Measurement of W-Helicity Fractions in $t\bar{t}$ decays and Search for Exotic Dihiggs Production in the $b\bar{b}WW^*$ Decay Channel Using the ATLAS Detector

DISSERTATION

Presented in Partial Fulfillment of the Requirements for the Degree Doctor of Philosophy in the Graduate School of The Ohio State University

By

Benjamin Tannenwald, B.A., B.S., M.S.

Graduate Program in Physics

The Ohio State University

2017

Dissertation Committee:

Harris Kagan, Advisor

Richard Kass

Stuart Raby

Andrew Heckler

Abstract

Two analyses using the ATLAS detector at the Large Hadron Collider are presented. The first analysis uses 20.2 fb^{-1} of data collected at a center of mass energy of $\sqrt{s} = 8$ TeV to produce a measurement of the helicity fractions of W bosons produced in the semileptonic decays of top quark pairs. The helicity fractions are measured using both the leptonically and hadronically decaying W bosons. The fractions measured using the leptonic W are the most precise values obtained to date, and the fractions obtained using the W decaying to quarks represent the first direct measurement using the hadronic W decays in top quark pairs. The fitted fractions of longitudinal, left-handed, and right-handed polarization states using the leptonic W are $F_0 = 0.709 \pm 0.019$, $F_{\text{L}} = 0.299 \pm 0.015$, and $F_{\text{R}} = 0.008 \pm 0.014$ respectively. These results are in agreement with the Standard Model prediction of $F_0 = 0.687 \pm 0.005$, $F_{\text{L}} = 0.311 \pm 0.005$, and $F_{\text{R}} = 0.0017 \pm 0.0001$. The second analysis uses 36.1 fb^{-1} of data collected at a center of mass energy of $\sqrt{s} = 13$ TeV and presents a search for Higgs boson pair production where one Higgs boson decays via $h \to b\bar{b}$ and the other Higgs boson via $h \to WW^* \to \ell\nu q\bar{q}$ (where ℓ is either an electron or a muon). This is the first search using the $b\bar{b}\ell\nu q\bar{q}$ final state to search for double Higgs production. Upper limits are placed on the cross-section of non-resonant and resonant Higgs pair production with resonant masses ranging from 500 to 3000 GeV. The most stringent observed (expected) limit is found for a resonant mass of 2500 GeV at 0.23 (0.45) pb. The largest deviation between the observed and expected limits is found at a resonance mass of 1800 GeV and has a local significance of 1.87 σ.

For Erika, Alice, Fred, and Marvin

Go to school
Get your doctorate
- Kanye West

Acknowledgments

Of all the pieces of my dissertation, this part might have been the most difficult part to write. Graduate school has been a long journey, and it's nearly impossible to think of, much less thank, all the people who have been a part of my life (and education) in Columbus and Geneva these last six years. First and foremost, thanks to Harris Kagan for having the patience to work with me through my first fumbling attempts at research and giving me the freedom to pursue a variety of different projects and interests during my time at OSU. Your help and advice have been essential, and I wouldn't be here today without your work and trust. Thanks are also due to Richard Kass for being an eternal voice of reason and K.K. Gan for the good stories and delicious meals in the French countryside. It would be a crime not to thank Joshua Moss, Renat Ishmukhametov, Suyog Shrestha, James Beacham, and even Chris Martin for their collective wisdom and uncountable numbers of conversations about research, physics, and life in general. CERN would have been an emptier place without your guidance and friendship.

A graduate student can't survive on research alone, and it's the people outside physics who have kept me sane and human during my PhD. Thanks to Kristina Looper who has somehow put up with me as a roommate on two separate continents for a total of almost two years. Your reserves of patience for my numerous character flaws are truly boundless. I'm not sure how the Catholic church chooses saints, but you've got my vote. Surviving the first two years of graduate school would have been unthinkable without Sean Flowers, and I'm incredibly grateful you eventually gave in and came to CERN for your own research. Matt Warren is another person without whom I can't imagine life in Columbus and who deserves endless thanks for all the good times and great conversations. Evan Prellberg also deserves a well-earned thank you for having been a true friend going on a decade now. Thanks for the California haven during candidacy and for forgiving me for making you drive up to Madison by mistake when I was actually in Milwaukee. If that's not friendship, I just don't know what is.

I'm unbelievably lucky to have spent a year and a half sharing two apartments with Jenna Iodice and Emily Wisnosky. It's a wonder how two conversations on the sidelines led to some of the best roommates and friendships I've had, but I'm not complaining. Charlie

Mueller is owed a huge debt of gratitude for putting up with me from Philosophes to Philo-not and is another friend that I don't deserve but I'm happy to have had in my life. The dude abides. Thanks are also due to Charlie Goodlake, Andrea Tognina, and Johannes Fexner for the times shared in the nicest place I'll ever live. Words will never do it justice, but thanks as well to the extended community of the Geneva Wizards. Vous étiez vraiment ma famille et mon monde durant les trois années que j'ai passé à Genève. Je ne peux pas vous remercier assez.

Lastly, I'd like to thank my family for everything; I wouldn't be the person I am today without you. Thanks to Katianne for putting up with me growing up and being the best sister I've ever had. Thanks Mom, Dad, Opa & Grandma, and Mema & Pop-pop for what I have to imagine was an often exasperating experience raising me. Nothing I write comes close to expressing the gratitude I have for the life and love you've given me. It's been a couple years now that I keep saying I should be finishing my PhD at the end of next semester. Thanks for being patient, and I promise that this time, I'm graduating for real.

Vita

May 2011 .... B.S., B.A. University of Kansas, Lawrence, Kansas, USA

September 2011 – May 2013 .... Graduate Teaching Assistant, Ohio State University, Columbus, Ohio, USA

August 2013 .... M.Sc. Ohio State University, Columbus, Ohio, USA

September 2013 – August 2017 .... Graduate Research Assistant, Ohio State University, Columbus, Ohio, USA

Publications

"Search for Higgs boson pair production in the $b\bar{b}WW^*$ final state at $\sqrt{s} = 13$ TeV the ATLAS detector", with M. Aaboud et. al. [ATLAS Collaboration], In preparation

"Measurement of the W Boson Helicity Fractions in $t\bar{t}$ Events at $\sqrt{s} = 8$ TeV in the Lepton + Jets Channel with ATLAS", with M. Aaboud et. al. [ATLAS Collaboration], Eur. Phys. J. C 77 (2017) 264

"Measurements of $Z\gamma$ electroweak production in association with a high-mass dijet system at $\sqrt{s} = 8$ TeV with the ATLAS detector", with M. Aaboud et. al. [ATLAS Collaboration], Submitted to Journal of High Energy Physics

"Search for Higgs boson decays to a photon and a Z boson in pp collisions at $\sqrt{s} = 7$ and 8 TeV with the ATLAS detector", with M. Aaboud et. al. [ATLAS Collaboration], Phys. Lett. B, 732, 8 (2014)

Fields of Study

Major Field: Physics

Studies in LHC physics, higgs decays, top quark physics, di-higgs searches, $t\bar{t}$ measurements, statistical interpretations of data, hardware and software development

Table of Contents

List of Figures

Figure **Page**

List of Tables

Chapter 1
Introduction

It's always best to start at the beginning.
- The Wizard of Oz

High energy physics is the study of the smallest and most fundamental building blocks of nature on the scale of attometers (10^{-15} m) and smaller. In order to study these incredibly tiny objects, physicists participate in scientific collaborations made up of thousands of scientists and engineers to collide particles like protons and atomic ions at speeds of over 99.9999% the speed of light. The enormous amounts of time, energy, and money dedicated to facilities like the Large Hadron Collider (LHC) are a testament to the significance of the questions high energy physics aims to answer, namely what are we made of, how did we get here, and why does it all work? There's a certain poetry in the fact that studying interactions on such small scales requires colliders tens of kilometers long, experiments the size of four story buildings, and the combined work of people scattered across the globe.

The Standard Model (SM) of particle physics is a model that describes nearly all we know about the observed fundamental particles and their electromagnetic, weak nuclear, and strong nuclear interactions. Missing from this picture is gravity, and the correct description of gravity at a quantum level is an open issue in theoretical physics. Chapter 2 provides a description of the various forces described by the Standard Model as well as more in-depth discussions of the Higgs mechanism and the top quark.

Experiments like ATLAS were built to test the predictions of the SM and search for new phenomena. Weighing more than the Eiffel Tower and measuring thirty by fifty meters, ATLAS is the largest detector at the LHC. Chapter 3 discusses the various sub-components of the detector and kind of tells you how they work. From measurements gathered by the hundreds of millions of channels in the detector, the various particles produced in collisions are identified and used to work backwards to understand the fundamental interactions taking place at the heart of the detector. Chapter 4 discusses how the particles used to 'do physics' are identified and reconstructed.

The analyses presented in this thesis are examples of the kinds of questions we can ask and the types of answers we can provide using the information produced at the LHC. Chapter 5 deals with precisely measuring the angular distributions and helicity fractions of particles produced in the decays of top quarks, enabling a better understanding of the mathematical structure governing such decays. Chapter 6 presents a search for the production of exotic new particles decaying into pairs of Higgs bosons, providing a way to discover or exclude new theories governing the fundamental interactions of particles.

1.1 Original Work

The enormity and scale of the experiments at the LHC precludes any single physicist or engineer from being able to claim individual responsibility for the complete whole of any physics result or analysis; everyone stands on the shoulders of giants. As such, much of the work presented in this thesis takes advantage of the collaboration of thousands of physicists over the course of several years. Several elements are however the unique and original contributions to the field by the author, namely:

- the kinematic fitting used to reconstruct the $t\bar{t}$ system in the W-helicity measurement especially with respect to the studies and results of the sensitivity of the kinematic fit to reconstruct and correctly identify the flavor of the daughters of the hadronic W decay. The helicity measurements produced from the hadronic W decay are the first direct helicity measurements using hadronic W decays in $t\bar{t}$ events,

- the template fitting used in the W-helicity measurement to extract the helicity fractions from the final distributions,

- the development, validation, and use of an ABCD method to estimate the multi-jet background in the dihiggs search,

- the statistical fit used in the dihiggs measurement to produce upper limits on non-resonant and exotic resonant dihiggs production.

Chapter 2
The Standard Model

> A possible explanation of the physicist's use of mathematics to formulate his laws of nature is that he is a somewhat irresponsible person.
>
> - Eugene Wigner

The Standard Model (SM) of particle physics is a relativistic quantum field theory that describes the fundamental particles of matter and their interactions via the electromagnetic, weak nuclear, and strong nuclear forces. The first steps toward the formalization of the SM were taken in the 1960s by the work of Glashow [1], Weinberg [2], and Salam [3] that described the unification of the electromagnetic and weak nuclear forces. The SM consists of particles with half integer spin called fermions and particles with integer spin called bosons. All known matter is constructed from the fermionic particles while the bosonic particles are responsible for mediating the interactions between particles. Fermions come in two types – leptons and quarks – which are further organized by mass into three generations[1].

The fermions possess various "charges" that determine the possible interactions between particles. If a fermion interacts with other particles via a given force, it is said to be "charged" under that force and the associated field. Interactions between two fermions charged under the same field proceed via the exchange of the force-carrying bosons. A simple example of this is the Coulomb repulsion between two electrons – electrons are both charged under the electromagnetic force ($q = -e$) and interact via the exchange of the force-carrying boson of the electromagnetic force, the photon. A Feynman diagram depicting this interaction is shown in Fig. 2.1. Figure 2.2 summarizes the particles of the Standard Model as well as some of their fundamental properties like mass, spin, and electric charge. While the charge of the electromagnetic force is electric charge and the mediating boson is the massless photon, the weak nuclear force is mediated by the exchange of heavy $W^{\pm}$ and Z bosons for particles possessing a weak charge, and the strong nuclear force is mediated by

[1] Each generation consists of one left-handed quark doublet, two right-handed quark singlets, a left-handed lepton doublet, and one right-handed charged lepton singlet. There is no current experimental evidence for right handed neutrinos. [4, 5]

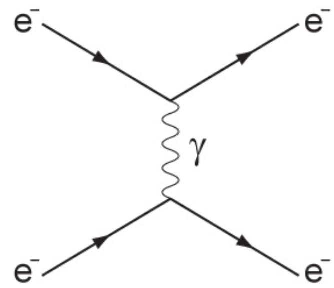

Figure 2.1: A Feynman diagram depicting the electromagnetic interaction between two electrons. The interaction is mediated by the exchange of a photon (a spin-1 gauge boson).

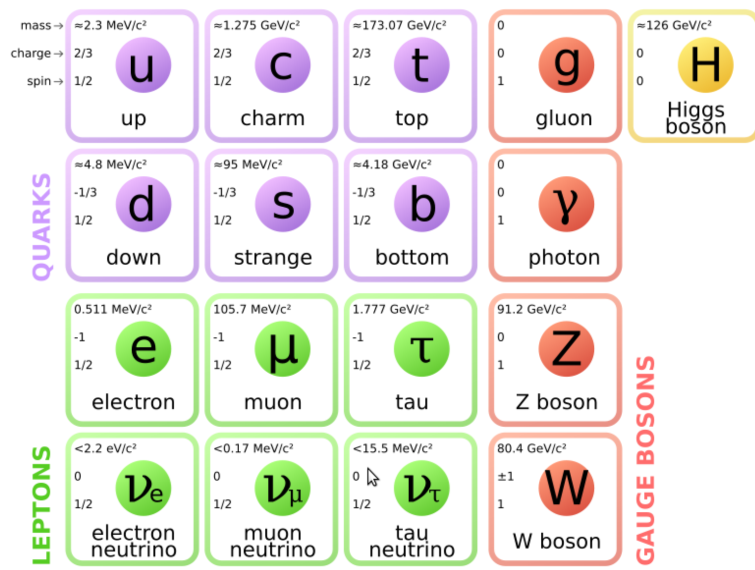

Figure 2.2: The constituents of the Standard Model and their masses, electric charges, and spin information.

the exchange of massless gluons between particles possessing color charge. Charged leptons (unsurprisingly) possess electric charge as well as weak charge while the neutral leptons (neutrinos) possess only a weak charge. Quarks are charged under the electromagnetic, weak, and strong nuclear forces and are the only fermions that interact via the strong force. Figure 2.3 shows a schematic representation of all the particles of the Standard Model and sketches out the allowed interactions between those particles through their connecting lines.

Gluons can be identified as the gauge fields, $G_i (i = 1 \cdots 8)$, of an $SU(3)$ gauge group. The strong force is non-chiral (i.e. treats right and left handed particles equally), and

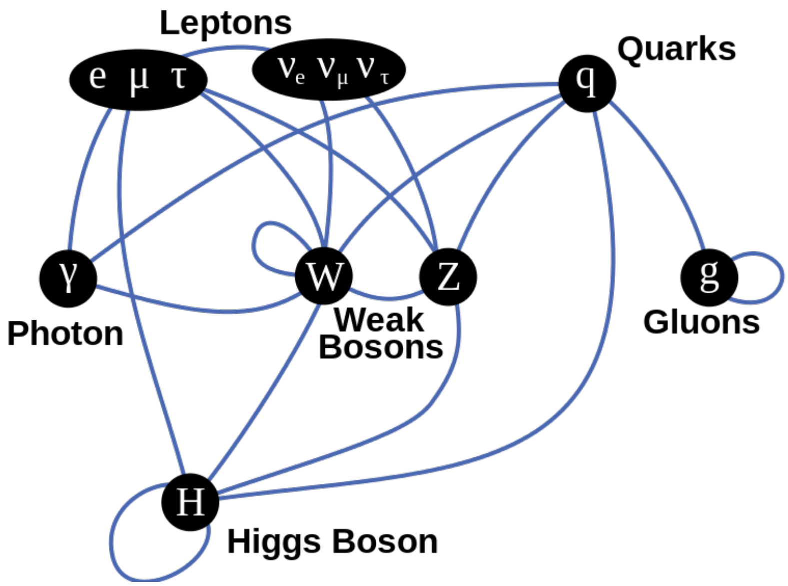

Figure 2.3: A schematic representation of the Standard Model. All constituent particles are represented by the black circles/ovals while their allowed interactions are signified by the connecting blue lines.

the $SU(3)$ operators act on the color indices of both left and right handed quarks. An important property of the strong force (also called quantum chromodynamics or QCD) is the confinement of color charge into color singlets. Colored objects (quarks and gluons) cannot exist in isolation, and they quickly hadronize (cascading decays of quarks via the strong force into mesons and baryons) into groups of particles called jets [6, 7].

The weak nuclear force and electromagnetism can be combined into an $SU(2) \otimes U(1)$ gauge group [2]. In contrast to the strong force, the weak force is chiral and acts on the flavor indices of only left handed fermions. The $U(1)$ subgroup is also chiral but acts on both left and right handed fermions [5]. The three gauge fields of $SU(2)$, $W_i (i = 1, 2, 3)$, along with the single gauge field of $U(1)$, B, combine after electroweak symmetry breaking to form the $W^{\pm}$, Z, and γ.

The full, unbroken group structure of the Standard Model is written

$$SU(3)_C \otimes SU(2)_L \otimes U(1)_Y \tag{2.1}$$

where the subscripts have physical rather than group significance. C denotes the strong color interaction group, Y represents the weak hypercharge, and L signifies the left-handed nature of the weak force. The full Lagrangian density of the Standard Model can be expressed as the sum

$$\mathcal{L} = \mathcal{L}_{gauge} + \mathcal{L}_{fermion} + \mathcal{L}_{\phi} + \mathcal{L}_{Yukawa} \tag{2.2}$$

where the individual parts refer to the gauge, fermion, Higgs, and Yukawa sectors of the SM. The Yukawa sector describes interactions between scalar and Dirac fields, e.g. flavor changing interactions between quarks via the weak force. The generation of mass for fermions via interaction with the Higgs field is also described by a Yukawa interaction.

2.1 Electroweak Theory

The unification of the weak and electromagnetic force into an $SU(2)_L \otimes U(1)_Y$ gauge group was first accomplished by Glashow [1]. The $SU(2)$ subgroup contains three gauge fields – one positively charged, one negatively charged, and one neutral. Since the weak interaction is observed to exhibit only a $V - A$ (vector - axial) coupling, only left handed operators are generated by the $SU(2)$ group, hence the L subscript. Right handed fermions are invariant singlets under $SU(2)_L$. Electromagnetism does not discriminate based on handedness, so the neutral field of $SU(2)$ cannot be the photon.

To incorporate the photon, the weak group is enlarged to $SU(2)_L \otimes U(1)_Y$ by adding the independent unitary group, $U(1)_Y$. The conserved quantity associated with this new group is called weak hypercharge and is denoted by the subscript Y. The hypercharge operator is defined as $\frac{Y}{2} = Q - I_3$ where Q is the electric charge, and I_3 is the third component of weak isospin.

To maintain local gauge invariance under group transformations, the ordinary derivative operator is replaced with the covariant derivative

$$\partial_\mu \rightarrow D_\mu = \partial_\mu - ig_1 \frac{Y}{2} B_\mu - ig_2 \left(\frac{\vec{\tau}}{2} \cdot \vec{W}_\mu \right) \tag{2.3}$$

where τ_i's are the Pauli matrices. The subscript index, μ, signifies the four-vector nature of the relevant objects and runs over the four spacetime dimensions. Inserting the covariant derivative into the SM Lagrangian couples the leptons and quarks to the electroweak gauge fields. The resulting interactions can be grouped into charged current and neutral current interactions with gauge fields [5, 7]

$$W^\pm_\mu = \frac{1}{\sqrt{2}}(W_{1\mu} \pm iW_{2\mu}),\ Z^0_\mu = \frac{-g_1 B_\mu + g_2 W_{3\mu}}{\sqrt{g_1^2 + g_2^2}} \tag{2.4}$$

The neutral field, Z^0_μ, cannot be the electromagnetic field, A_μ, since it mediates a coupling between left handed neutrinos, electrically uncharged fermions that do not interact electromagnetically. Since A_μ cannot couple to neutrinos, it must be orthogonal to the weak current that does. The gauge fields of $SU(2)_L$ and $U(1)_Y$ are orthogonal by construction, so the weakly orthogonal electromagnetic gauge field is defined

$$A_\mu = \frac{g_2 B_\mu + g_1 W_{3\mu}}{\sqrt{g_1^2 + g_2^2}} \tag{2.5}$$

The extended electroweak gauge group provides the structure to accommodate the electromagnetic and weak forces, but the extremely short range of the weak force ($\mathcal{O}(1\text{ fm})$) remains problematic. A gauge group exhibiting an exact symmetry, such as quantum electrodynamics (QED), contains massless gauge fields which mediate a force with infinite extent. The short range of the weak force implies massive mediating gauge fields; however, mass terms cannot be added directly to the SM Lagrangian while maintaining gauge invariance. In order to reproduce observed physical phenomena, current theory holds that the $SU(2)_L \otimes U(1)_Y$ symmetry of the Standard Model must be spontaneously broken.

2.2 Higgs Mechanism

The Englert-Brout-Higgs-Guralnik-Hagen-Kibble mechanism, proposed in the early 1960s by several independent groups [8–10] and often called simply the Higgs mechanism, is one way to generate the required symmetry breaking. This spontaneous symmetry breaking (SSB) can be accomplished by the introduction of a complex scalar doublet field

$$\phi = \begin{pmatrix} \phi^+ \\ \phi^0 \end{pmatrix} \tag{2.6}$$

where the superscripts denote electric charge. The Lagrangian for such a field is written as

$$\mathcal{L}_\phi = T - V = (\partial_\mu \phi)^\dagger (\partial^\mu \phi) - \mu^2 \phi^\dagger \phi - \lambda (\phi^\dagger \phi)^2 \tag{2.7}$$

where $V = \mu^2 \phi^\dagger \phi + \lambda(\phi^\dagger \phi)^2$ is the potential and $\mu^2 < 0$. The complex fields in Eq. 2.6 can be rewritten in terms of real fields $\phi^+ = (\phi_1 + i\phi_2)/\sqrt{2}$ and $\phi^0 = (\phi_3 + i\phi_4)/\sqrt{2}$, yielding

$$\mathcal{L} = \frac{1}{2}\sum_{i=1}^{4}(\partial^\mu \phi_i)(\partial_\mu \phi_i) - \frac{\mu^2}{2}\sum_{i=1}^{4}\phi_i\phi_i - \frac{\lambda}{4}\left(\sum_{i=1}^{4}\phi_i\phi_i\right)^2 \tag{2.8}$$

which is invariant under a global $SO(4)$ phase rotation in ϕ-space. If μ^2 is positive, the potential has a minimum at $\Phi^2 = (\phi_1 + \phi_2 + \phi_3 + \phi_4)^2 = 0$, and the $SO(4)$ symmetry remains unbroken. However, if $\mu^2 < 0$, the potential is minimized around a circle with radius $v = \sqrt{\frac{-\mu^2}{\lambda}}$. The vacua of the field can be arbitrarily rotated such that $\phi_1 = \phi_2 = \phi_4 = 0$, yielding vacuum expectation values (VEVs) of $\langle 0 \,|\, \phi^0 \,|\, 0 \rangle = \frac{v}{\sqrt{2}}$, $\langle 0 \,|\, \phi^+ \,|\, 0 \rangle = 0$.

After breaking and rotation, the Higgs doublet is written

$$\phi = \frac{1}{\sqrt{2}}\begin{pmatrix} 0 \\ v + h(x) \end{pmatrix} \tag{2.9}$$

This new field, $h(x)$ is identified as the physical Higgs boson. [8–10]

The weak gauge bosons gain mass through interactions arising from the covariant derivatives in the kinetic portion of Eq. 2.8. Inserting the covariant derivatives and keeping terms proportional to the square of the gauge fields yields

$$(D_\mu\phi)^\dagger(D^\mu\phi)_{mass} \sim (\frac{vg_2}{2})^2 W^{+\dagger\mu}W_\mu^{-\dagger} + \frac{1}{2}(\frac{v\sqrt{g_1^2+g_2^2}}{2})^2 Z^\mu Z_\mu \tag{2.10}$$

The masses of the gauge bosons are thus identified as

$$m_W = \frac{vg_2}{2},\ m_Z = \frac{v\sqrt{g_1^2+g_2^2}}{2},\ m_A = 0 \tag{2.11}$$

The electromagnetic field A_μ remains massless since no corresponding term is generated in the symmetry breaking. Electromagnetic charge conservation is also preserved. SSB breaks the extended electroweak group into the $U(1)$ gauge group of QED and the $SU(3)_C$ color group of QCD:

$$SU(3)_C \otimes SU(2)_L \otimes U(1)_Y \rightarrow SU(3)_C \otimes U(1)_{QED} \tag{2.12}$$

Mass terms for fundamental fermions can be generated by the Higgs mechanism via a Yukawa coupling between left and right handed fermions and the Higgs field. The SM Higgs is also required to be a spin-0 (scalar) boson even under charge-parity (CP) conjugation [11].

2.2.1 Single Higgs Production

Single Higgs boson production can occur via four different processes

- gluon-gluon fusion (ggF)
- vector boson fusion (VBF)
- vector boson associated production (VH)
- $t\bar{t}$ associated production (ttH)

The leading order Feynman diagrams for each process are shown in Figure 2.4.

Since hadronic accelerators do not collide individual quarks or gluons but rather hadrons such as protons, the rate of each production mechanism is set by the relative abundance of quarks, anti-quarks, and gluons in the colliding hadrons. Probability distributions called parton distribution functions (PDFs) are produced using measurements from fixed target and collider experiments [12–17] and model the probability for a particle of species s inside a hadron (e.g. a proton or anti-proton) to possess a given fraction, x, of the total momentum of the hadron. The more abundant a particle is at relatively low fractional energy, the more likely it is that for that particle to be involved in a collision with another hadron. Figure 2.5 shows the parton distribution functions obtained by the MSTW collaboration [12]. At a proton-proton collider like the LHC, the gluon fusion production mechanism is dominant

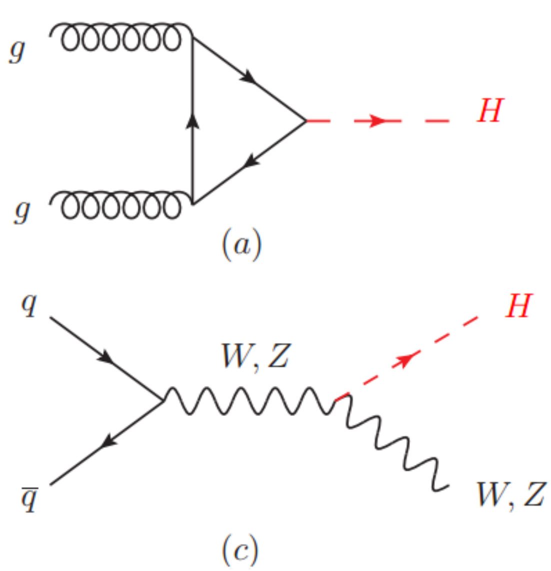

Figure 2.4: Feynman diagrams for single Higgs boson production via the a) gluon fusion, b) vector boson fusion, c) association with a vector boson, and d) association with a $t\bar{t}$ pair.

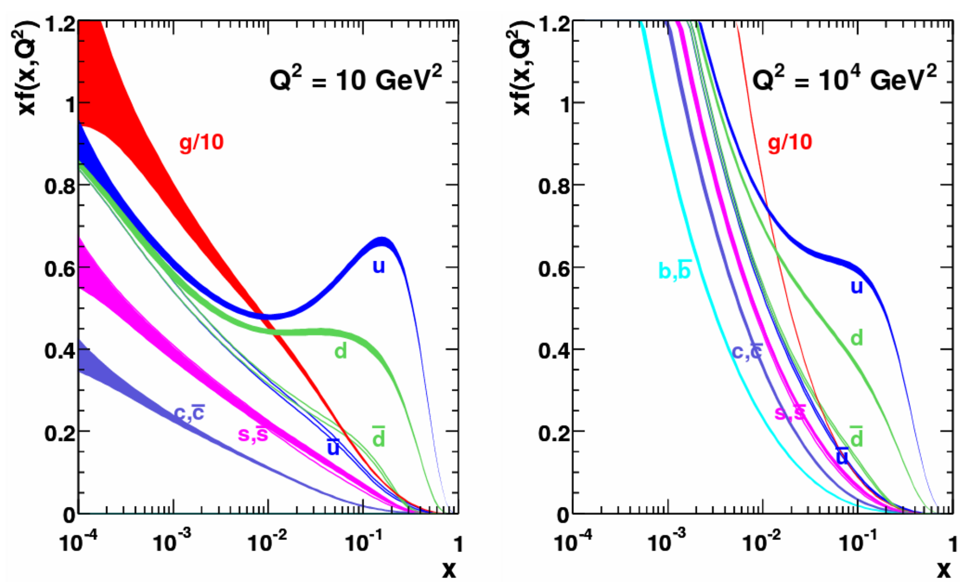

Figure 2.5: Parton distribution functions developed by the MSTW collaboration for the gluons and quarks (up/down/strange/charm/bottom) found in protons. The x-axis is represents the fractional momentum possessed by a particle inside the proton and the y-axis is the fractional momentum times population frequency as a function of fractional momentum and momentum transfer.

due to the relatively large population of gluons with enough combined energy to produce a Higgs boson. Figure 2.6 shows the rates of each production mechanism for a pp collider like the LHC.

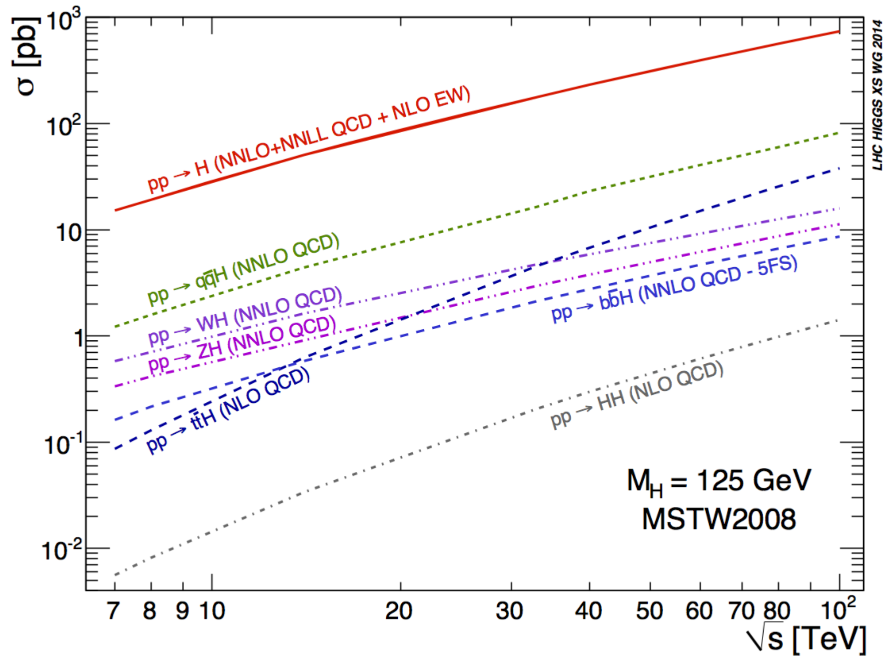

Figure 2.6: Standard Model Higgs production rates as a function of center of mass energy.

As gluons do not couple directly to the Higgs boson (gluons are perturbatively massless), the gluon fusion diagram proceeds via a quark loop interaction which couples directly to the Higgs field through its Yukawa coupling. Since the Higgs-fermion Yukawa couplings are directly proportional to the fermion mass, the contribution from the top quark loop dominates the gluon fusion mode. For a Higgs mass of 125 GeV, the cross-section for the gluon fusion production mechanism at the LHC is σ_{ggF} =19.27 pb^{-1} at $\sqrt{s}$ =8 TeV and 43.92 pb^{-1} at $\sqrt{s}$ =13 TeV [18]. While the gluon fusion mode has the largest cross-section at the LHC, the lack of additional identifying features (e.g. no associated jets or leptons produced in the interaction) makes for larger backgrounds relative to other production modes. Still, the larger cross-section of the gluon fusion mode means this is a dominant mode for analysis at the LHC.

In production via vector boson fusion, an incoming quark and anti-quark pair scatter off each other via the exchange of W or Z bosons, and the resulting vector bosons fuse to produce a Higgs boson. The outgoing quarks pick up a large recoil from the emission of the heavy W/Z bosons, and the final state for vector boson production is characterized by the presence of two high momentum quark jets in addition to the decay products of the Higgs itself. While the cross-section for Higgs production via the vector boson fusion mode is small at the LHC for a Higgs with a mass of 125 GeV (σ_{VBF} =1.58 pb^{-1} at $\sqrt{s}$ =8 TeV, 3.75 pb^{-1} at $\sqrt{s}$ =13 TeV [18]), the VBF mode has a higher signal to background ratio compared to the gluon fusion mode after requiring the presence of two high momentum jets in addition to the Higgs in the final state.

The associated production (VH) mode is characterized by the production of a Higgs boson in association with a W or Z vector boson. In this process, the heavy vector boson is produced via quark/anti-quark annihilation and radiates a Higgs boson before decaying to either leptons or quarks. In analogy with the bremsstrahlung process by which an electrically charged particle emits a photon, the associated production mechanism is often also referred to as higgsstrahlung. For a Higgs mass of 125 GeV, the cross-section for the associated production mechanism at the LHC is σ_{VH} =1.12 pb^{-1} at $\sqrt{s}$ =8 TeV and 2.25 pb^{-1} at $\sqrt{s}$ =13 TeV [18]. The presence of the high p_{T} decay products of the W/Z boson in the final state (especially for leptonic decays) is a powerful handle for reducing backgrounds despite the relatively low cross-section.

The last mode for single Higgs production at the LHC is the production of a Higgs boson in association with a pair of top quarks (also referred to as the $t\bar{t}H$ mode). The $t\bar{t}H$ mode can be proceed via the collision of two gluons that produce a top quark/anti-quark pair of which one quark radiates a Higgs boson (this diagram is shown in Fig. 2.4). The $t\bar{t}H$ mode can also be produced from the fusion of two gluons into a single gluon which then splits into a top quark/anti-quark pair of which one top radiates a Higgs. The presence of the $t\bar{t}$ pairs in addition to the Higgs boson gives the $t\bar{t}H$ production mode a rich final-state phenomenology, but the low cross sections ($\sigma_{t\bar{t}H}$ =0.13 pb^{-1} at $\sqrt{s}$ =8 TeV and 0.51 pb^{-1} at $\sqrt{s}$ =13 TeV [18] for a 125 GeV Higgs) make this a challenging process to search for at the LHC.

2.2.2 Single Higgs Decay

Once produced, the Higgs boson can decay into a particle/anti-particle pair of any particle coupling to the Higgs field via mass. Since the Higgs-fermion coupling is proportional to the fermion mass and the Higgs-boson coupling is proportional to the boson mass squared, the larger the mass of a particle coupled to the Higgs, the larger the branching fraction of Higgs decays. Figure 2.7 shows the Higgs branching fractions as a function of mass [19]. Decays to final states of massless particles, e.g. pairs of photons or gluons, proceeds via a quark or heavy vector boson loop analogous to the loop in gluon fusion production shown in in Fig. 2.4.

The branching fractions depend strongly on the mass of the Higgs, and for the observed

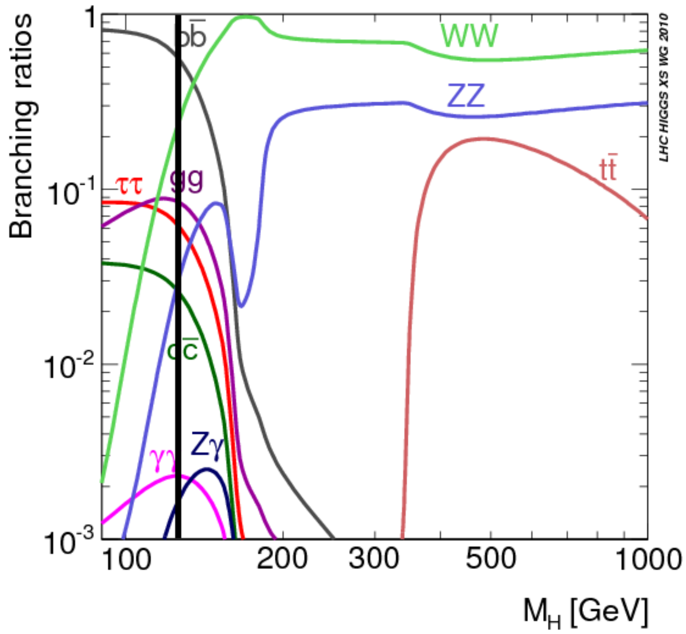

Figure 2.7: Standard Model branching fractions for a Standard Model Higgs across a range of Higgs masses. The black line vertical line at 125 GeV shows the branching fractions for the Higgs boson measured by the ATLAS and CMS collaborations.

Higgs mass of 125.09 ± 0.24 GeV [20], the $b\bar{b}$ and WW^* decay modes have the largest branching fractions, accounting for 79.3% of all Higgs decays [18]. While other modes such as $\gamma\gamma$ and ZZ^* have relatively smaller branching fractions (0.23% and 2.67% respectively), searches for these decay modes can yield more sensitive (larger ratio of signal to background events) results compared to decay modes with larger branching fraction due to their relatively smaller Standard Model backgrounds. The $h \to ZZ^*$ in the fully leptonic decay channel in particular has enormous sensitivity since the SM 4ℓ background is tiny. Combining measurements of Higgs properties in multiple decay channels improves the overall precision of our knowledge about the Higgs boson and the mechanism behind electroweak symmetry breaking.

2.2.3 Double Higgs Production

While single Higgs production can occur via a number of processes, Higgs bosons can also be produced in pairs through Higgs self-interactions or via double higgsstrahlung. Probing the Higgs self-interactions explores a completely new sector of physics and has great potential (pun not intended) for the field of precision Higgs measurements. The potential of the Lagrangian in Eq. 2.8 has a minimum at $\phi = \pm\sqrt{\frac{-\mu^2}{\lambda}}$. Taking ϕ to be a simple scalar field as an example, we can introduce the field variable

$$\eta = \phi \pm \sqrt{\frac{-\mu^2}{\lambda}} \tag{2.13}$$

the Lagrangian in Eq. 2.8 becomes

$$\mathcal{L}_\phi = \frac{1}{2}\left(\partial_\mu \eta\right)\left(\partial^\mu \eta\right) - \mu^2\eta^2 \pm \mu\lambda\eta^3 - \frac{1}{4}\lambda^2\eta^4 + \frac{1}{4}(\mu^2/\lambda)^2 \tag{2.14}$$

The first two terms are the familiar kinetic and mass terms, but now we have additional terms proportional to η^3 and η^4. These terms represent self-couplings of the Higgs field of the third and fourth order. Eqs 2.8 and 2.14 describe identical physics, but the second formulation presents the self-interactions in more evident way. Diagrams for the leading order ($\sim \eta^3$) Higgs self-interaction and double higgsstrahlung (via a quark loop and quark-Higgs Yukawa couplings) are shown in Fig. 2.8.

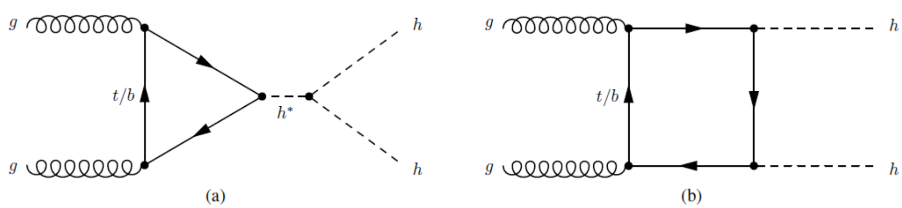

Figure 2.8: Leading order Feynman diagrams for dihiggs production due to a) the Higgs self-interaction and b) the Higgs-fermion Yukawa interaction.

The Standard Model contributes to dihiggs production only through non-resonant modes, but many models of new physics can yield additional contributions to dihiggs production when that new physics couples to the SM Higgs sector [21]. In the minimal supersymmetric extension of the Standard Model (the MSSM), there are five Higgs bosons (one neutral light CP even, one neutral heavy CP even, one neutral CP odd, and two charged Higgs bosons) of which the neutral light CP even Higgs, h, can be identified as the Standard Model Higgs boson. The heavy neutral CP even Higgs, H, can decay into hh pairs due to the mixing of the Higgs doublets in the model. Measuring the rate of dihiggs production in this context can then be used to constrain the range of possible masses and mixing angles in the theory. Figure 2.9 shows a leading order example of an H resonance decaying to two Higgs bosons.

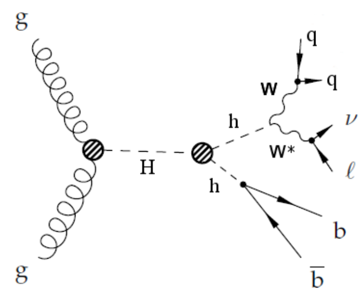

Figure 2.9: Schematic Feynman diagram showing gluon fusion initiated production of an exotic resonance, H, and its decay into two Higgs bosons.

2.3 Top Physics

The top quark, discovered in 1995 by the D0 and CDF collaborations at Fermilab [22,23], is the heaviest particle in the SM. Top quarks decay nearly universally via $t \to Wb$ and have a lifetime of $\sim 10^{-25}$ seconds. The top is so massive that its lifetime is much smaller than the time it would take to hadronize ($\sim 10^{-23}$ s), so precision measurements of top quark decays allow for measurements of the 'bare' electroweak properties of the top quark. Studying distributions sensitive to the production mechanisms of top quarks allows for constraints on PDF, and studying the high energy tails of top quark distributions acts as a probe of the existence of any new physics coupling to the Standard Model via mass. In short, precision top quark measurements can help say a lot about how high energy physics works at the edge of our understanding.

2.3.1 Top Quark Production

Top quarks can be produced in a variety of ways, and at a hadron collider like the LHC, the production of top quarks is dominated by strong pair production of top/anti-top quark pairs. The leading order Feynman diagrams for strong $t\bar{t}$ production are shown in Figure 2.10. Gluon-fusion initiated production dominates at the LHC while quark/anti-quark annihilation is suppressed due to the low abundance of anti-quarks relative to gluons in the quark sea of the proton (see Fig. 2.5. At a center of mass energy of $\sqrt{s} = 8(13)$ TeV and a top quark mass of 172.5 GeV, the $t\bar{t}$ production cross-section at the LHC is predicted [24] to be

$$\sigma_{t\bar{t}}\ (8\ \text{TeV}) = 252.89\ \text{pb}^{-1} \qquad \sigma_{t\bar{t}}\ (13\ \text{TeV}) = 831.76\ \text{pb}^{-1}$$

While Section 5 deals entirely with top quark pair production, single top quarks can be produced via the weak interaction. Figure 2.11 shows the leading order Feynman diagrams

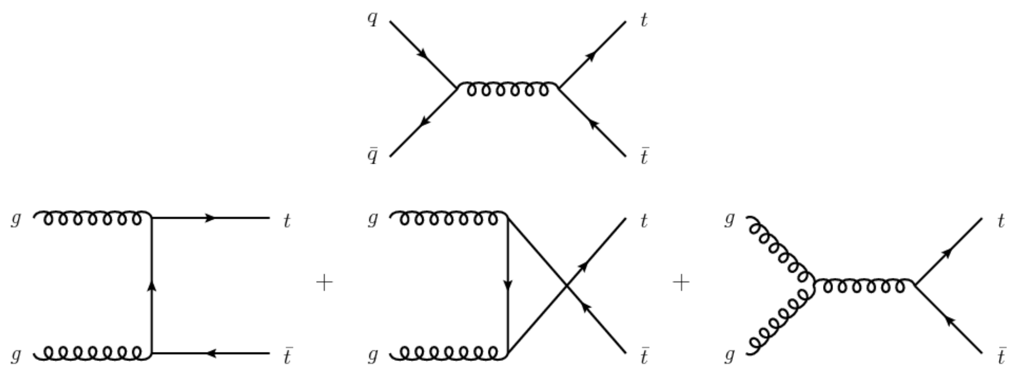

Figure 2.10: Leading order Feynman diagrams for strong top pair production at the LHC.

that contribute to single top production. At the LHC, the total cross-section for single top production at $\sqrt{s} = 8$ and 13 TeV with a top quark mass of 172.5 GeV is calculated [25] to be

$$\sigma_t \text{ (8 TeV)} = 112.30 \text{ pb}^{-1} \qquad \sigma_t \text{ (13 TeV)} = 299.01 \text{ pb}^{-1}$$

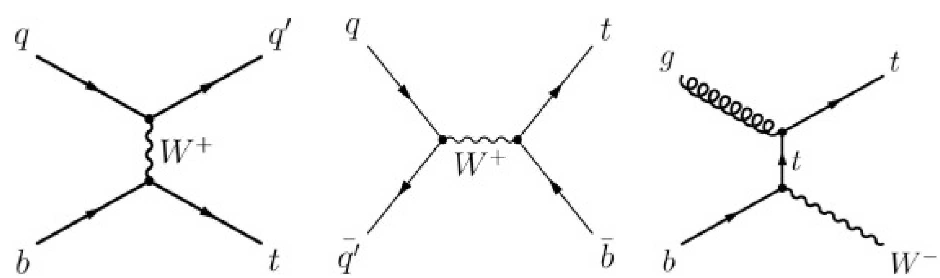

Figure 2.11: Leading order Feynman diagrams for electroweak single top production at the LHC.

Both $t\bar{t}$ and single top production have been studied at the LHC by the ATLAS and CMS collaborations, and the results have been in good agreement with prediction. Figure 2.12 summarizes the results from both experiments [26].

2.3.2 Top Quark Decay

Measurements of top quark pairs are usually classified by the decay products of their daughter W bosons

- fully hadronic decays where both W's decay into qq' pairs

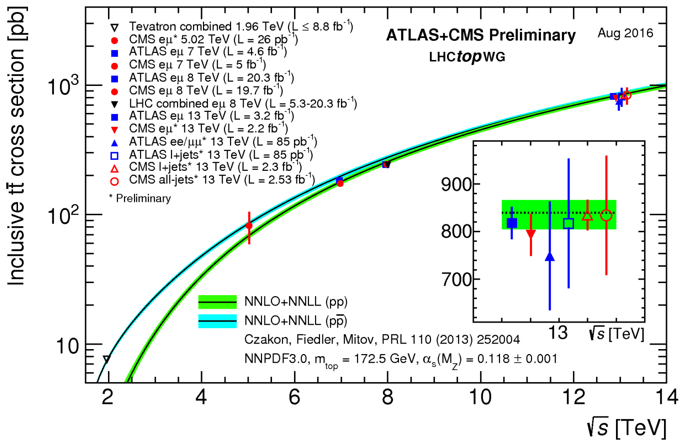

Figure 2.12: Measured inclusive top quark pair cross-sections as measured at $\sqrt{s} = 2$ TeV at the Tevatron and at $\sqrt{s} = 7, 8$, and 13 TeV at the LHC. Several analyses with different final states and different integrated luminosities are shown, and the agreement between theoretical predictions and measured cross-sections is clear across the entire range of probed energies.

- fully leptonic decays when both W's decay into lepton/neutrino pairs
- and semileptonic decays when one W decays leptonically and the other hadronically.

Classification by W decays is possible since the top quark decays almost exclusively via $t \to Wb$. A breakdown of the various decay channels is shown in Figure 2.13.

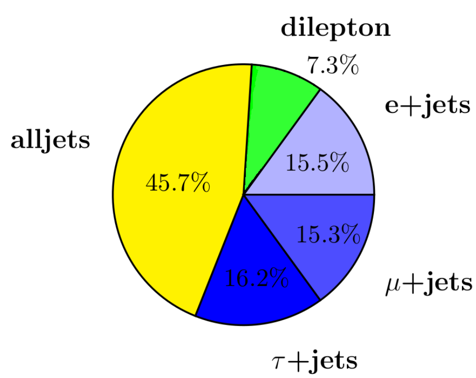

Figure 2.13: Top quark pair production decay channels. The green dilepton portion represents the fully leptonic decays of the $t\bar{t}$ pair, the yellow alljets portion corresponds to the fully hadronic decays, and the remaining blue portions represent the semileptonic decay channels.

It is clear from Figure 2.13 that (neglecting the τ+jets contribution) the fully hadronic channel has the highest branching fraction followed by the semileptonic and lastly the fully leptonic channel. Studying each decay channel has its own strengths and weaknesses. The fully hadronic channel has the largest branching fraction but comes with a large and difficult to model QCD background and a combinatorical ambiguity. The fully leptonic channel has the smallest branching fraction but the highest signal to background ratio and the presence of two neutrinos makes it difficult to fully reconstruct the $t\bar{t}$ system.

Sitting between the full leptonic and fully hadronic decays, the semileptonic channel possesses a reasonable branching ratio and signal to background ratio, and the presence of a single neutrino means that it is possible to fully reconstruct the $t\bar{t}$ pair. Results from all three channels provide independent information used to measure top quark decay and constrain exotic physics in the Wtb vertex.

Chapter 3
The LHC and the ATLAS Detector

> Why build the LHC? Because those damn Americans will never follow through with that project in Texas.
>
> - Something I Assume Someone Has Said

In order to test the predictions of the Standard Model and other exotic theories, experiments must be designed and built that enable precision measurements of highly energetic and often rare processes. The Large Hadron Collider at CERN was built for precisely this reason, and four main detectors (ATLAS, CMS, ALICE, and LHCb) record and analyze the data produced in proton-proton (pp), proton-lead ($p-Pb$), and lead-lead ($Pb-Pb$) collisions to draw conclusions about the underlying mechanisms governing our subatomic world. As this thesis is based on work done using the ATLAS detector, it is the only experiment discussed in depth.

Measuring the rate at which an interesting process occurs (i.e. a cross-section) is related to the total number of collisions delivered to a detector and the number of interesting interactions observed. Put algebraically

$$\frac{dN_{\text{events}}}{dt} = \mathcal{L} \times \sigma_{\text{process}} \tag{3.1}$$

where $\frac{dN_{\text{events}}}{dt}$ is the rate of events observed, $\mathcal{L}$ is the number of particles per unit area per unit time that can collide in the detector (i.e. instantaneous luminosity), and σ_{process} is the cross-section of the process in question. The luminosity delivered to an experiment like ATLAS is set by the geometry and operating conditions of the LHC. The total number of events recorded by a detector is a function of measurement capabilities of its component sub-systems, the rate at which collision information can be extracted from the detector and stored for later analysis, and the total number of collisions delivered by the LHC.

To understand both these elements, this section provides an overview of the LHC and concludes with in-depth descriptions of the various sub-components of ATLAS detector.

3.1 The LHC

The LHC is a superconducting particle accelerator and collider operated at the Centre Européen pour le Recherche Nucleaire (CERN) and situated on the border between France and Switzerland [27]. The main ring has a circumference of 27 km making it the largest built man-made accelerator. Before particles (both protons and lead ions) collide in the main LHC ring, they first pass through a multi-stage accelerator chain with the energy and intensity of the particle beams increasing at each step. Since the research in this thesis was performed using proton-proton collisions, only the proton acceleration chain is discussed. The protons used in collisions start as simple hydrogen gas. The hydrogen is ionized,

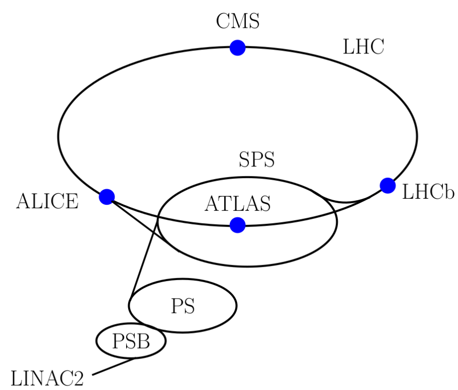

Figure 3.1: The LHC accelerator chain.

and a linear accelerator (linac) is used to accelerates bunches of the resulting protons to 50 MeV/c. These protons are then successively accelerated to 1.4 GeV/c by the Proton Synchrotron Booster (PSB) and to 25 GeV/c by the Proton Synchrotron (PS). From here, the proton bunches are injected into the Super Proton Synchrotron (SPS) and accelerated to 350 GeV/c.

After acceleration in the SPS, the proton bunches are injected into the LHC. The final injected proton beam is not a continuous proton stream as the word beam might imply but a *train* of proton bunches precisely spaced and calibrated to deliver specific luminosities to the different detectors, allow for efficient detector operation, and provide abort gaps to safely dump the beams if and when instabilities arise in the main LHC ring. The beam size is also set in the injection from the SPS to the LHC rings. The entire accelerator chain, from the LINAC to the LHC is diagrammed in Figure 3.1.

Once in the LHC rings, the beams undergo their final acceleration before colliding. Using 1232 8.3 T superconducting dipole magnets cooled to 1.9 K, the LHC is capable of accelerating protons to a maximum design momentum of 14 TeV/c.

The luminosity delivered discussed in Eq. 3.1, $\mathcal{L}$, can be written as a function of several of the parameters discussed above

$$\mathcal{L} = \frac{N_b^2 n_b f_{\text{rev}}}{4\pi\sigma_x\sigma_y} \tag{3.2}$$

where N_b is the number of protons per bunch, n_b is the number of bunches per beam, f_{rev} is the revolution frequency of the beams, and $\sigma_x\sigma_y$ are the transverse widths of the proton beams with respect to the beam direction. Most of these parameters are set in the injection from the SPS to the LHC and the final acceleration in the LHC rings.

The actual luminosity delivered to the ATLAS detector throughout the data-taking periods in 2012, 2015, and 2016 varied depending on the different center of mass energies ($\sqrt{s} = 8$ TeV in 2012 and $\sqrt{s} = 13$ TeV in 2015 + 2016) and beam filling and compression schemes. The total integrated luminosities delivered by the LHC in the periods used in this thesis are shown in Figure 3.2.

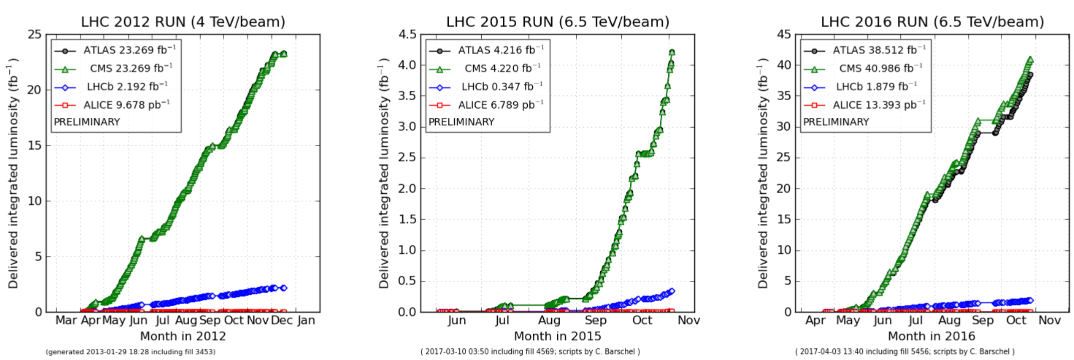

Figure 3.2: Total integrated luminosities delivered by the LHC to the four main detectors in data-taking periods in 2012, 2015, and 2016. The total luminosity is shown as a function of the date of data-taking across the three years.

3.2 ATLAS

The ATLAS detector is one of the four main detectors at the LHC. Standing for **A T**oroidal **L**HC **A**pparatu**S**, the detector's distinguishing feature is its series of air-core toroidal magnets which aid in the identification of muons produced in collisions. A schematic diagram of the ATLAS detector is shown in Figure 3.3 [28]. ATLAS is composed of multiple subsystems, each responsible for different measurements used to reconstruct the fundamental interactions occurring with each collision. ATLAS is a general-purpose detector meaning that each subsystem is designed to be sensitive over a large range of particle energies in order to have sensitivity to a wide variety of phenomena; if you don't know where to look for new physics, you have to be able to look everywhere.

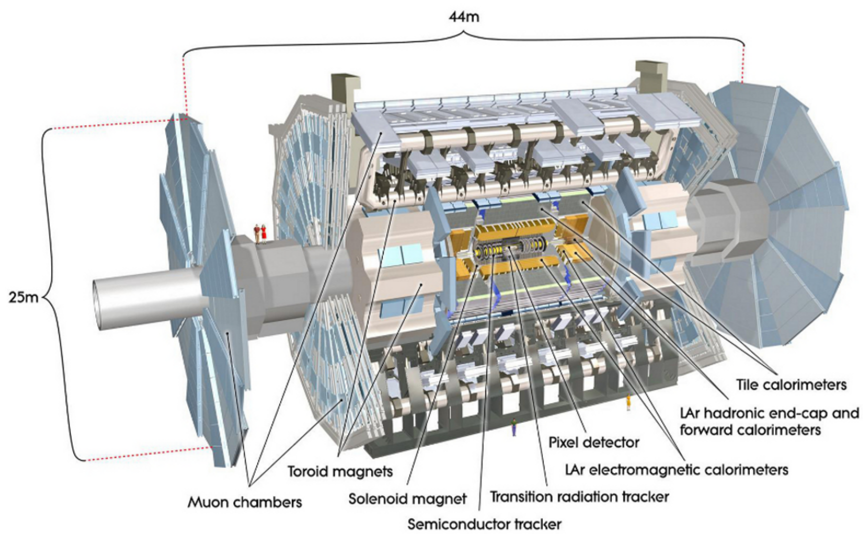

Figure 3.3: A schematic figure of the ATLAS detector.

Starting from the collision point and moving radially outward, the inner detector is responsible for charged track reconstruction and is the first subsystem to record the passage of charged particles produced at the interaction point. After the inner detector, a calorimetry system absorbs the electrons, photons, and neutral and charged hadrons produced in collisions. Charged particles surviving absorption in the calorimeters are then recorded by a multi-part muon spectrometer. The detector is designed to have almost complete hermetic coverage, i.e. to cover nearly the entire solid angle surrounding the interaction point such that as few particles escape detection as possible.

ATLAS is forward-backward symmetric with respect to the nominal interaction point and uses a Cartesian coordinate grid centered around this point. The positive z-axis is pointed along the beam line while the positive x-axis points inward toward the center of the LHC ring and the y-axis points upwards. The azimuthal angle, ϕ, is defined in the transverse x-y plane, and the polar angle, θ, is defined as the angle between the transverse plane and the z-axis. Pseudorapidity is defined as $\eta = -\ln(\tan(\theta/2))$.

3.2.1 Magnet Systems

ATLAS uses a hybrid magnet system composed of a central, superconducting solenoid surrounding the inner detector and three exterior (one central and two endcap) toroids. The central solenoid is made of a single coiled layer of superconducting Titanium/Niobium cooled to 4.5K and produces an axial magnetic field of 2.0 T. Each of the three toroids is composed of eight coils radially symmetric around the beam axis and cooled and operated at a temperature of 4.6K. The barrel toroid produces a magnetic field of 0.5 T, while the two endcap toroids each produce magnetic fields of 1.0 T. Figure 3.4 shows the spatial arrangement of the central solenoid and the barrel and endcap toroids.

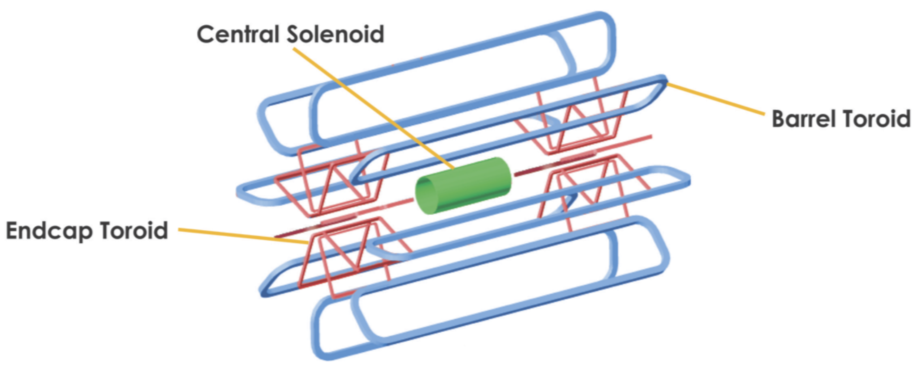

Figure 3.4: The toroids and solenoid of the ATLAS magnet system.

The magnet system bends the trajectories of charged particles passing through the ATLAS detector and allows for precise determinations of those particles' momenta. The central solenoid aids in the measurement of electrons, protons, and other charged hadrons, while the toroids produce magnetic fields used to precisely measure muon momenta. The non-trivial magnetic field of ATLAS requires dedicated measurements of the magnetic field in order to produce precise tracking measurements of the charged particles produced in collisions [29].

3.2.2 Inner Detector

An inner detector (ID) with high resolution tracking subsystems is required to reconstruct the large number of charged particles produced in collisions. The ATLAS inner detector provides coverage inside $|\eta| \leq 2.5$ and is made of pixel and micro-strip silicon trackers (SCT) surrounding the beam pipe followed by a gas-straw transition radiation tracker (TRT) [30, 31]. The basic principle behind the inner detector is to measure the passage of charged particles while minimally affecting their trajectories and energies. The pixel and strip subsystems track the passage of particles bent by the solenoidal magnetic field while the TRT collects radiation profiles of passing particles useful in identifying the kinds of particles (electron, pion, etc) being produced. Figure 3.5 shows a cut-away view of all subsystems of the inner detector.

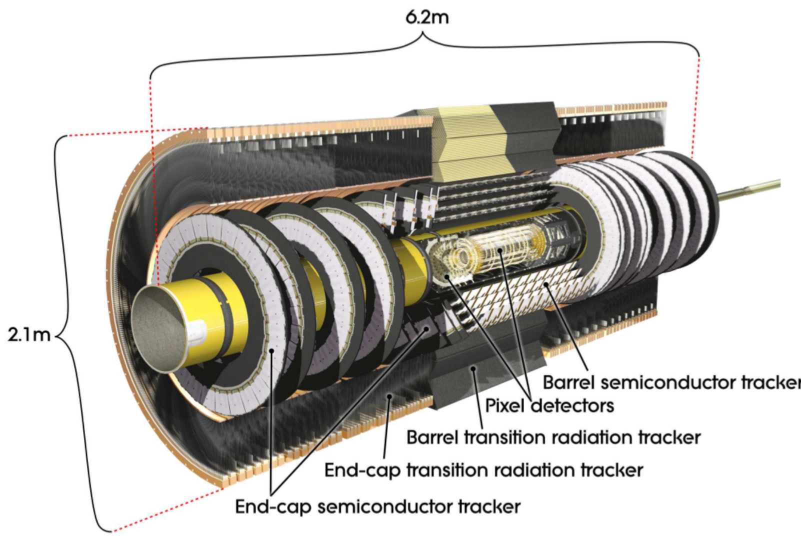

Figure 3.5: A cut-away view of the ATLAS inner detector.

As the innermost element of the inner detector, the silicon pixel and strip systems must be able to deal with the enormous flux of charged particles produced at the interaction point. Both the pixels and strips are arranged in three layers with barrel region modules oriented parallel to the beam axis and two endcap regions with modules oriented perpendicular to the beam axis. Each pixel sensor has a minimal $R-\phi \times z$ pixel size of 50×400 μm^2 and intrinsic resolutions of 10 μm in $R-\phi$ and 115 μm in z for both the barrel and the endcaps. The secondary silicon strip layers have intrinsic resolutions of 17 μm in $R-\phi$ and 580μm in z for both the barrel and the endcaps. Combined, the three layers of the SCT have nearly 90 million output channels to be processed for each collision.

A fourth layer, positioned inside the previous described three and named the insertable beam layer (IBL), was installed during the first LHC shutdown and was in operation for data-taking in 2015 and 2016 [32]. The IBL sensing volume contains ∼12 million 50×250 μm^2 pixels at an average radius of 3.3 cm from the interaction point. The addition of a fourth, inner layer to the inner detector helps to improve tracking performance in the high occupancy environment and large pileup expected from the intense luminosities experienced in run II of the LHC. Figure 3.6 shows the difference between the measured and true longitudinal and transverse impact parameters of the primary vertex in simulated $t\bar{t}$ decays with and without the addition of the IBL [32]. The additional tracking information also improves the performance of algorithms used to identify jets arising from b jets produced in collisions.

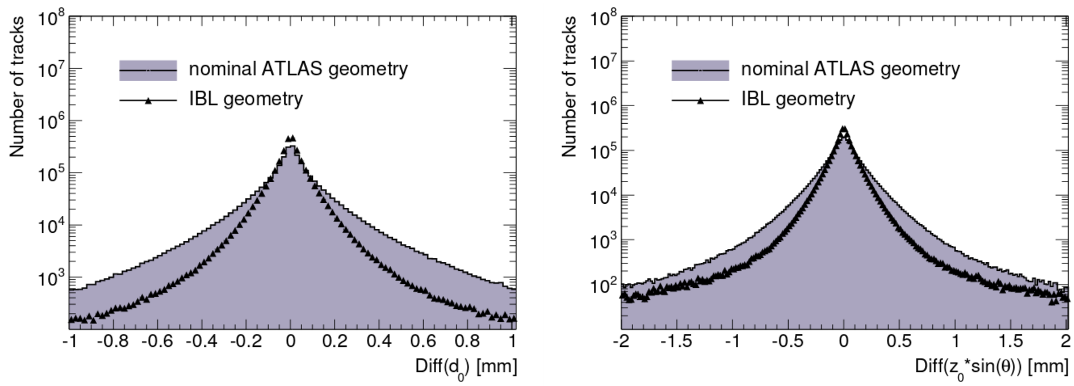

Figure 3.6: Difference between reconstructed and true transverse (left) and longitudinal (right) impact parameters for tracks produced by simulated $t\bar{t}$ decays. Distributions are shown for the nominal inner detector and with the inclusion of the IBL.

The last element of the inner detector, the TRT covers a region of $|\eta| < 2.0$ and is composed of thousands of gas-filled straw drift tubes which provide extra information in identifying pions and electrons. Each straw (cathode) has an outer diameter of 4 mm and a 31 μm diameter central tungsten wire acting as the anode. The straws are filled with a gaseous mixture of Xe, CO_2, and O_2 which is ionized by passing charged particles. The resolution of the TRT in the $R - \phi$ direction is $\sim$130 μm.

By analyzing the radiation patterns left by passing particles, the TRT aids in differentiating electrons from pions over an energy range between 1 and 200 GeV. The performance of the TRT for pion identification and rejection was studied using collision data at $\sqrt{s} = 7$ TeV [33]. The simulated and measured probabilities of pion mis-identification over the momentum range 4 to 20 GeV are shown in Figure 3.7. While there is an increase in pion mis-identification around $|\eta| \sim 0.8$ due to the transition between the endcap and barrel components of the TRT, the average pion rejection factor across the detector and full momentum range is $\sim$20 and up to 100 for the best performing regions.

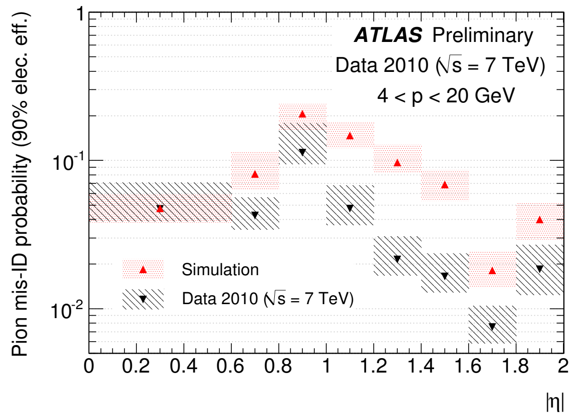

Figure 3.7: Pion mis-identification probability for a high threshold hits criteria that gives 90% electron efficiency in bins of eta. The detector performance exceeds the simulation-based expectations, in particular in the end-cap region ($|\eta|> 0.8$).

3.2.3 Calorimeters

The ATLAS electromagnetic (ECAL) and hadronic (HCAL) calorimetry systems cover the range $|\eta|\leq 4.9$ and provide precise measurements of the energies of electrons, photons, and hadrons passing through the inner detector. Both the electromagnetic and hadronic calorimeters employ alternating layers of absorbing material designed to initiate showers from passing particles and layers of active material responsible for measuring the energies of passing particles and the showers they produce.

Figure 3.8 shows the layout of the various hadronic and electromagnetic calorimeters used in ATLAS. The entire calorimetry system is designed to absorb as much hadronic and electromagnetic radiation from collisions as possible and to limit non-muonic sources of radiation from reaching the muon spectrometer. The electromagnetic calorimeters are placed in front of the hadronic calorimeters since the radiation length for particles passing through the calorimeter materials is smaller than the nuclear interaction length.

The electromagnetic calorimeter is composed of one barrel ($|\eta|< 1.475$) and two endcap components ($1.375 < |\eta|< 3.2$). Each ECAL component is made up of alternating layers of LAr sampling medium with accordion shaped electrodes and lead absorber plates. The accordion shape of the sampling medium provides fully symmetric azimuthal coverage without gaps. The thickness of the lead plates is optimized as a function of η and energy resolution.

The hadronic calorimeter is composed of a central, tile component and two LAr-based endcap components. The tile calorimeter is constructed of interspersed layers of steel and plastic scintillating tiles measuring the energy deposition of charged and neutral hadrons. Wavelength shifting fibers transport scintillation light to photo-multiplier tubes that convert

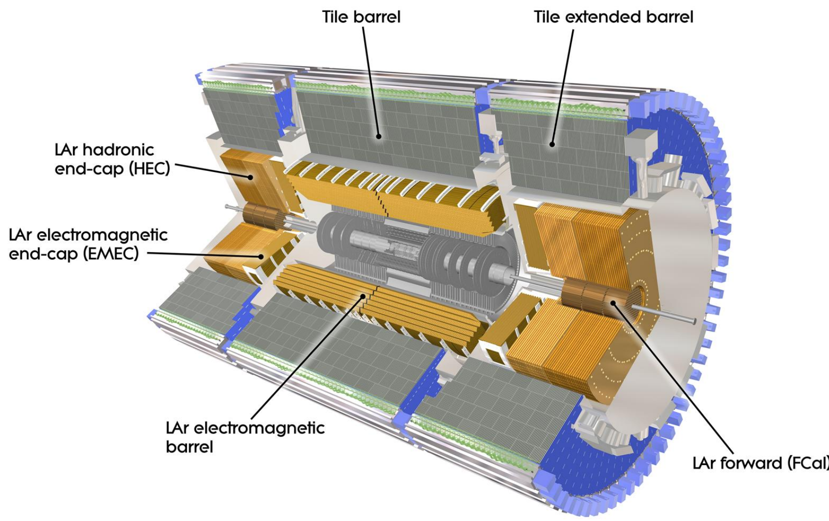

Figure 3.8: Diagram of the ATLAS calorimetry system.

the light to an electronic signal. The central tile calorimeter extends over $|\eta| < 1.7$ while the extensions cover $0.8 < |\eta| < 1.475$. At its outer edge, the tile calorimeter is approximately ten interaction lengths thick, providing enough material for good energy resolution of high p_{T} jets and leaving little hadronic energy left to bombard the muon spectrometer.

The LAr endcaps of the hadronic calorimeter are located directly behind the LAr ECAL endcaps and cover the range $1.5 < |\eta| < 3.2$, overlapping the tile calorimeter and the forward calorimeters. Copper is used in the endcaps as the absorbing material in place of lead. The two forward ($3.3 < |\eta| < 4.9$) liquid Argon calorimeters (FCAL) placed around the endcaps aid in both electromagnetic and hadronic measurements.

3.2.4 Muon Spectrometer

The muon spectrometer provides precision measurements for charged particles passing through the calorimetry systems and is the last system encountered by escaping particles produced at the interaction point. Information from monitored drift tubes and cathode strip chambers is combined to identify and measure the energy of passing charged particles, while resistive plate and thin gap chambers provide information for muon-based triggering as well as additional spatial measurements. Muon track reconstruction is possible thanks to the barrel and endcap toroid systems discussed in Section 3.2.1. Figure 3.9 displays the various subsystems of the muon spectrometer and their arrangement with respect to the toroid system.

Monitored drift tubes (MDTs) are responsible for measuring and tracking passing muons

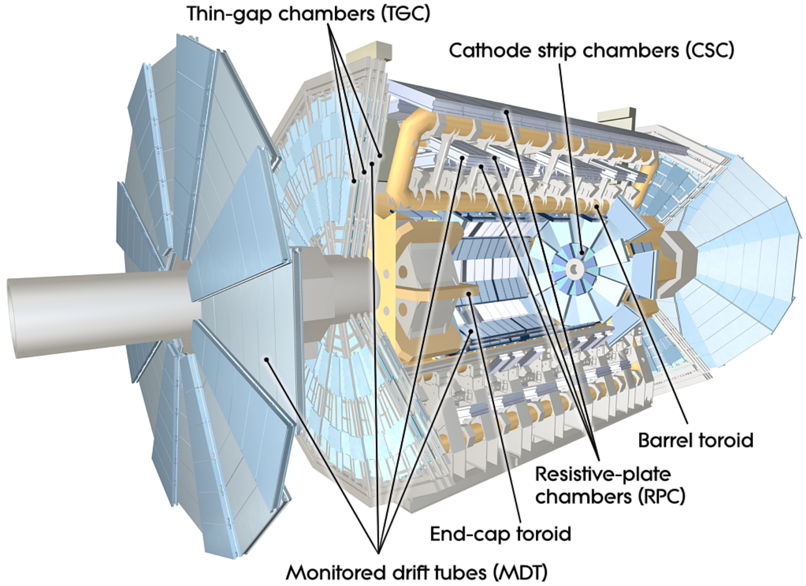

Figure 3.9: Diagram showing the various subsystems of the muon spectrometer and the toroids responsible producing the magnetic field that aids in track reconstruction.

throughout the majority of the η range covered by the muon system. Each tube is composed of a 30 mm diameter cylindrical aluminum tube with a central 50 μm diameter wire kept at a potential difference of 3270 V with respect to the outer cylinder. An Ar-CO_2 gas mixture fills the gap between the two and is ionized as a charged particle passes through the tube. The induced charge is collected by the central wire and provides timing and spatial resolution information used in track reconstruction. Each tube has an individual spatial resolution of $\sim$80μm [34].

At larger pseudorapidities($2.0 < |\eta| < 2.7$), a series of cathode strip chambers (CSCs) are used for muon track reconstruction. Each chamber is a multi-wire proportional chamber with high voltage wires suspended in a Ar-CO_2-CF_4 gas mixture and enclosed by two grounded conducting planes. The CSC system has over 67000 readout channels, and this high-granularity design gives the CSCs the sensitivity necessary to deal with the large flux of charged particles at high pseudorapidities. Tracks measured by the CSCs have a spatial resolution of $\sim$50μm [34].

Resistive plate chambers (RPCs) and thin gap chambers (TGCs) make up the last components of the muon system and are responsible for event triggering and muon tracking in the direction orthogonal to the drift tubes and strip chambers. Each chamber is composed of a parallel plate detector separated by 2mm and filled with a gaseous mixture of 94.7% $C_2H_2F_4$, 5% Iso-C_4H_{10}, and 0.3% SF_6. The RPCs are responsible for providing trigger information in the barrel region of the detector and have timing resolution of $\mathcal{O}(1\text{ ns})$.

The TGCs are multi-wire proportional chambers filled with a mixture of CO_2 and n-C_5H_{12} and provide triggering information in the forward region of the muon spectrometer. The wires in each TGC are separated by 1.8 mm, and the cathode to anode separation is 1.4 mm. The timing resolution of the TGCs is comparable to that of the RPCs. In addition to timing information, the both the TGCs and the RPCs also aid in the azimuthal angle, ϕ, of passing muon tracks. The spatial resolution for both systems is ~1 cm.

Since nearly all other particles excluding neutrinos (e.g. electrons, hadrons, photons) are absorbed in the calorimeter systems, the charged particles reaching the muon spectrometers are nearly always muons. Particles coming from secondary interactions in the detector are rejected by requiring tracks from the muon spectrometer to match tracks from the inner detector during muon reconstruction. The probability for incorrectly reconstructing a particle, e.g. a pion, as a muon was studied using collision data recorded at $\sqrt{s} = 7$ [35]. Figure 3.10 shows the probability to reconstruct a pion as a muon as a function of η and p_{T} for muon candidates reconstructed using a particular muon reconstruction algorithm ('Chain 2'). 'Combined' muons refer to muon candidates with tracks and a trajectory

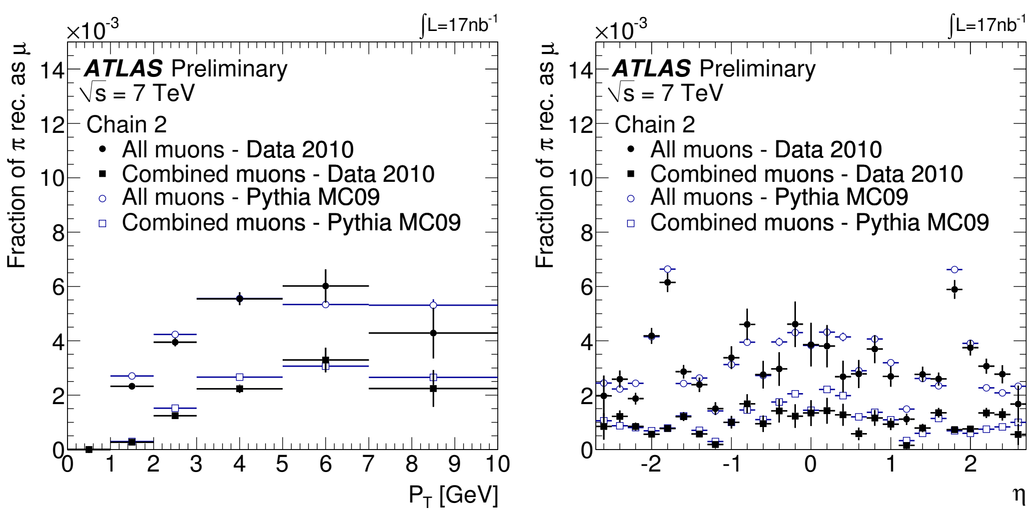

Figure 3.10: The measured fraction of pions reconstructed as muons in as a function of p_{T} and η. Results are shown for combined muons only and for combined and segment-tagged muons. The data are represented by filled markers, while Monte-Carlo simulation by open markers.

measured in the muon spectrometer is matched to tracks in the inner detector while the 'all' category includes muon candidates with only straight-line tracks measured in the muon spectrometer and matched to tracks measured in the inner detector. For both types of muon candidates, the overall pion mis-identification rate is below the 1% percent level.

3.2.5 Missing Energy Reconstruction

There is no good direct way to detect the high energy neutrinos produced in collisions at the LHC due to their weakly interacting nature. Possible new particles (e.g. dark matter, supersymmetric particles, etc.) could also be produced and escape ATLAS without detection if they have zero or highly suppressed electromagnetic and hadronic interactions. Instead of measuring the energy, momentum, or tracks of these particles directly, the 'missing' transverse energy (MET) in an event is calculated by balancing the total transverse energy deposited by an event and measured by the other components (calorimeters, muon systems) of ATLAS. Only the transverse component is calculable since the initial transverse momentum of the incoming partons is nearly zero while the longitudinal imbalance is *a priori* unknown.

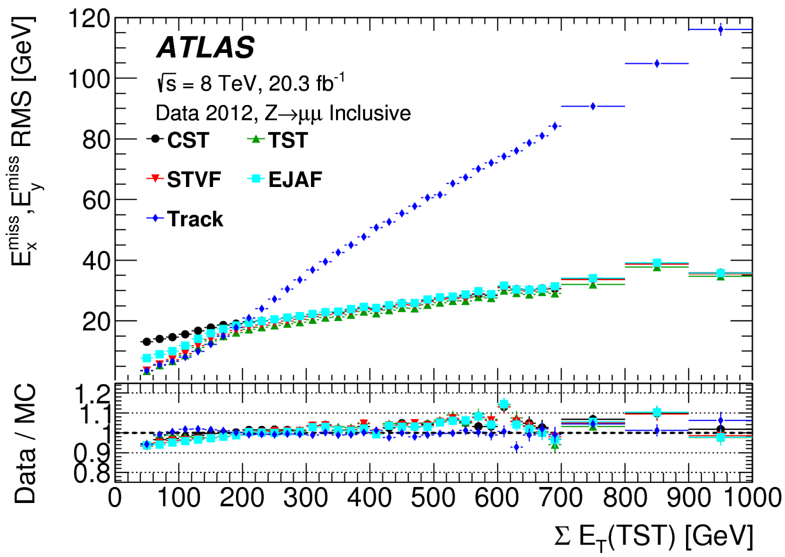

Figure 3.11: Resolution of missing energy in the x and y directions as a function of the total transverse energy measured in the calorimeter and muon systems in $Z \to \mu\mu$ events measured at $\sqrt{s} = 8$ TeV. Results are compared for several different algorithms used to calculate the missing transverse energy.

Since the missing energy in an event is not directly measured, is it important to minimize the effects in the MET calculation of incomplete detector coverage, finite detector resolution, and the presence of dead and noisy regions in the detector. ATLAS is designed as a hermetic detector, and the large η extension of the calorimeter and muon systems provide near-complete transverse coverage of the interaction point. Various algorithms to take detector resolution effects into account and suppress spurious sources of MET have been developed to improve the resolution of the missing energy calculation. Using collision data recorded at $\sqrt{s} = 8$ TeV and selecting $Z \rightarrow \mu\mu$ events, the MET resolution in the individual x and y directions was measured to be on the order of a few tens of GeV or less (for most $E_{\mathrm{T}}^{\mathrm{miss}}$ algorithms) in events with up to ~1 TeV of energy deposited in the ATLAS detector [36]. Figure 3.11 shows the resolution of the various algorithms for calculating the missing transverse energy as a function of the measured transverse energy.

3.2.6 Triggering and Data Acquisition

The high collision rate (40 million collisions per second) at the LHC produces many more events than can reasonably be recorded, and solving this problem requires fast detector readout electronics to quickly obtain collision data and efficient triggering infrastructure to decide which of the read out events are worthwhile to keep. The data acquisition system in ATLAS first receives data from the readout electronics connected to each sub-detector and buffers the information long enough to be processed by the event trigger. ATLAS used a three-level trigger during data-taking from 2010 through 2012. Improvements in the trigger algorithms and hardware enabled the use of a two-level trigger when data-taking resumed in 2015. Both frameworks are discussed below.

The first trigger level, known as the L1 trigger, is a hardware-based trigger using a small subset of the total calorimeter and muon spectrometer information to decide in under 2.5 μs whether or not to keep an event. Multiple inputs are used when in deciding whether to save an event, e.g. the presence of high p_{T} objects, large missing energy, large total transverse energy, etc. From an initial collision rate of 400 MHz, L1 processing reduces the event rate to ~75 kHz. In 2010-2012 data-taking, a secondary L2 trigger re-processes events passing the L1 stage using more complete detector information from the muon spectrometer and inner detector systems.

For events passing the L1 and L2 trigger processing (L1 only for data-taking after 2015), the software-based high level trigger (HLT) uses the full amount of data collected by the detector (including track and vertex reconstruction) to decide which events are written to disc. The HLT computer farm processes events in ~4 seconds and produces an output rate of ~200 Hz. During the first long LHC shutdown, the throughput capabilities of the HLT were significantly improved, allowing for the removal of the L2 stage in event processing. At the end of the triggering chain, each event is recorded to disc and has a per event size of ~1.3 MB. At 200 Hz, the ATLAS experiment records ~3000 TB of collision data per year.

Chapter 4
Object Definitions

They're like really complicated legos.

4.1 Electrons

4.1.1 8 TeV

Electron candidates [37] are reconstructed from energy deposits (clusters) in the electromagnetic calorimeter that are associated to reconstructed charged tracks in the inner detector. Candidates are required to have $p_{\mathrm{T}} > 25$ GeV and $|\eta_{\mathrm{cluster}}| < 2.47$ (where $|\eta_{\mathrm{cluster}}|$ is the pseudorapidity of the calorimeter cluster associated with the electron candidate). Candidates in the calorimetry transition region $1.37 < |\eta_{\mathrm{cluster}}| < 1.52$ are excluded. To reduce the background from non-prompt electrons, i.e. from decays of hadrons (including heavy flavor) produced in jets, electron candidates are also required to be isolated. An η-dependent, 90% efficient isolation cut is made on the sum of transverse energy deposited in a radius of $\Delta R = 0.2$ around the calorimeter cells associated with the electron[2]. The sum of energy deposited around the cells associated with the electron cluster is corrected for leakage from the electron cluster itself. A further 90% efficient isolation cut is made on the track transverse momentum (p_{T}) sum around the electron in a cone of radius $\Delta R = 0.3$ (p_T^{cone30}).

All candidate electrons are required to pass the tight++ ID requirement. Figure 4.1 shows the total reconstruction times identification efficiency as a function of η and transverse energy of electron candidates using in $Z \to e^+e^-$ events measured at $\sqrt{s} = 8$ TeV [38]. The data points labeled 'Tight' correspond to the electrons used in the W-helicity analysis presented in Chapter 5. In addition, the longitudinal impact parameter of the electron track with respect to the selected event primary vertex, z_0, is required to be less than 2 mm.

[2] ΔR is a measurement of the angular distance between two reconstructed objects and is defined as $\Delta R = \sqrt{(\Delta\eta)^2 + (\Delta\phi)^2}$.

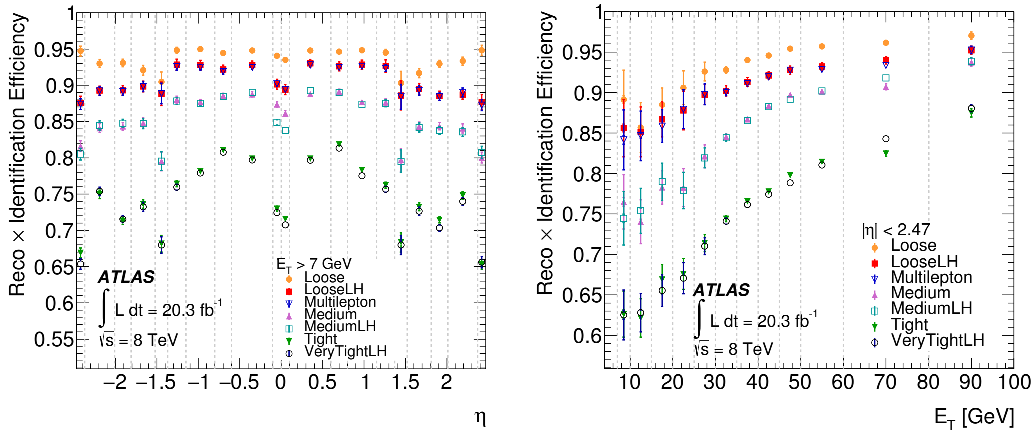

Figure 4.1: The combined reconstruction and identification efficiency for various cut-based and likelihood electron selections as a function of η (left) and E_T (right) using $Z \to e^+e^-$ decays measured at $\sqrt{s} = 8$ TeV. The data points labeled 'Tight' correspond to the electrons used in the W-helicity analysis presented in Chapter 5.

4.1.2 13 TeV

Electron identification is performed using a likelihood-based method which uses longitudinal and transverse shower profiles, track quality information, track and cluster matching, and the presence of high-threshold TRT hits to discriminate between electrons and other physics objects. The likelihood-based method allows the inclusion of discriminating variables that would be otherwise difficult to use without incurring significant efficiency loss.

An additional track-based isolation variable helps quantify the energy of the particles produced around the electron candidate to aid in the identification of prompt electrons from other, non-isolated electron candidates such as electrons originating from converted photons produced in hadron decays, electrons from heavy flavor hadron decays, and light hadrons mis-identified as electrons. The variable, $p_\mathrm{T}^{\mathrm{varcone0.2}}$, is defined as the sum of transverse momenta of all tracks, satisfying quality requirements, within a cone of $\Delta R = \min(0.2, 10\ \mathrm{GeV}/E_T)$ around the candidate electron track. A more detailed discussion on the electron likelihood identification and isolation variables and their performance with Run 2 data can be found in Ref. [39]. The electron energy scale is calibrated such that it is uniform throughout the detector, and the residual differences between data and simulation are corrected. The calibration strategy is based on the same strategy developed in Run-1 [40] and updates to the calibration strategy for Run-2 is documented in Ref. [41].

In order to be considered as a signal electron for the dihiggs analysis presented in Chapter 6, electron candidates must have $p_\mathrm{T} > 27$ GeV and be associated with a calorimeter cluster in the range of $|\eta| < 2.47$ with the crack region $(1.37 < |\eta| < 1.52)$ between the barrel and endcap calorimeters excluded. The candidate is required to pass a tight likelihood identification and must pass an isolation requirement of $p_{\mathrm{T}}^{\mathrm{varcone0.2}}$ / $p_{\mathrm{T}} < 0.06$. Figure 4.2 shows the total reconstruction times identification efficiency as a function of η and transverse energy of electron candidates using in di-electron events measured at $\sqrt{s}$ = 13 TeV [39]. The data points labeled 'Tight' correspond to the electrons used in the dihiggs analysis. Additional cuts are placed on electron candidates requiring the significance of the transverse impact parameter ($|d_0^{\mathrm{sig}}|$) to be less than two standard deviations and the $\sin\theta$-weighted longitudinal impact parameter of the electron tack to be less than 0.5 mm from the primary vertex.

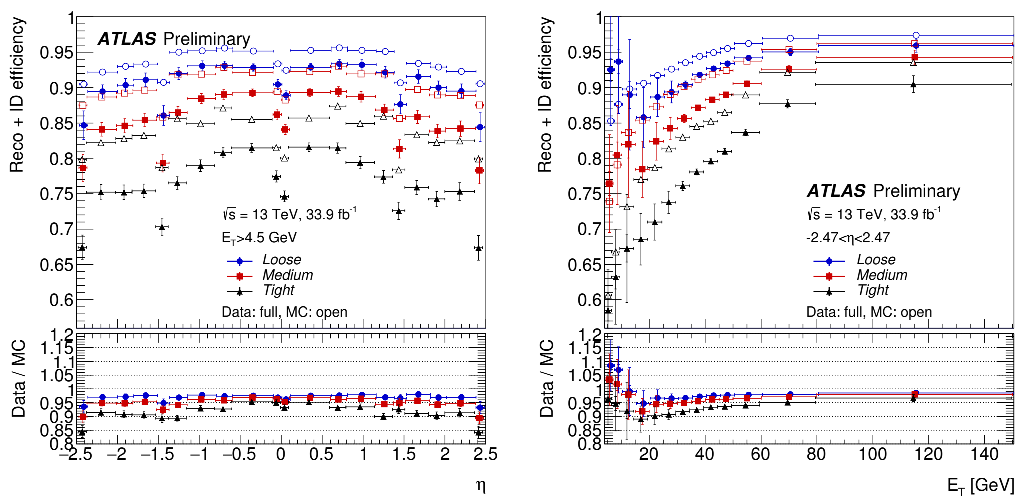

Figure 4.2: The combined reconstruction and identification efficiency for three likelihood-based electron selections as a function of η (left) and E_{T} (right) using di-electron events measured at $\sqrt{s}$ = 13 TeV. The data efficiencies are obtained by applying data/MC efficiency ratios that were measured in $J/\psi \to e^+e^-$ and $Z \to e^+e^-$ events to MC simulation. The data points labeled 'Tight' correspond to the electrons used in the dihiggs analysis presented in Chapter 6.

4.2 Muons

4.2.1 8 TeV

Muon candidates are reconstructed from track segments in the various layers of the muon spectrometer and matched with tracks found in the inner detector. The final candidates are refitted using the complete track information from both detector systems and required to satisfy $p_{\mathrm{T}} > 25$ GeV and $|\eta| < 2.5$. They are referred to as "combined" muons. Figure 4.3

shows the reconstruction efficiency for these types of muons (labeled 'CB+ST') with p_T up to 300 GeV and measured in $Z \to \mu^+\mu^-$ events recorded at $\sqrt{s} = 8$ TeV [42]. The reconstruction algorithm is over 99% efficient for the majority of the phase space probed. Muon candidates are required to satisfy a p_T-dependent track-based isolation requirement

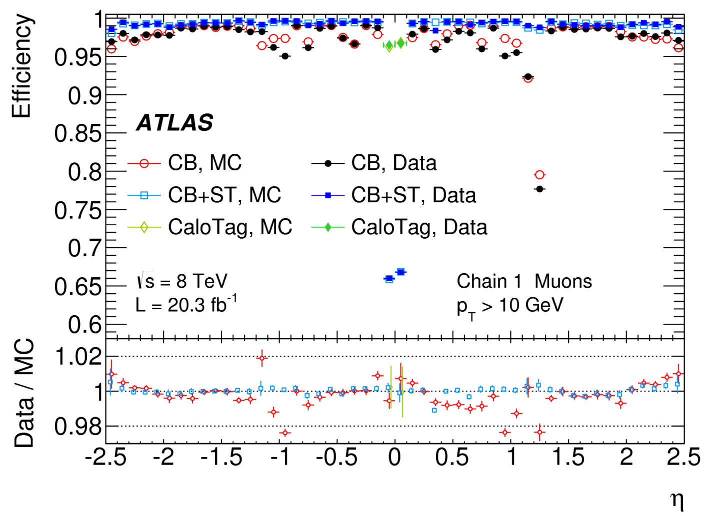

Figure 4.3: The muon reconstruction efficiency as a function of η measured in $Z \to \mu^+\mu^-$ events for muons with p_T >10 GeV and measured using collisions recorded with $\sqrt{s} = 8$ TeV. The panel at the bottom shows the ratio between the measured and predicted efficiencies. The data points labeled 'CB+ST' correspond to the muons used in the W-helicity analysis presented in Chapter 5.

that has good performance under high pileup conditions or in boosted configurations where the muon is close to a jet: the scalar sum of the track p_T in a cone of variable radius $\Delta R < 10$ GeV$/p_T^\mu$ around the muon (excluding the muon track itself) must be less than 5% of the muon p_T. Additionally, muons are required to be separated by $\Delta R > 0.4$ from any selected jet (see Section 4.3.1). Muons are required to have a hit pattern in the inner detector consistent with a well-reconstructed track. Analogous to the electrons, the muon track longitudinal impact parameter with respect to the primary vertex, z_0, is required to be less than 2 mm.

4.2.2 13 TeV

Muon candidates are identified using the algorithm described in Ref. [43]. Muons are selected within $|\eta| < 2.5$ using track quality criteria based on the number of hits in the inner detector and the muon spectrometer. Medium quality criteria are used for muon identification which require the presence of tracks matched between the inner detector and muon spectrometer. An additional track-based isolation variable, $p_{\mathrm{T}}^{\mathrm{varcone0.3}}$, is used to select isolated muons and is defined as the sum of transverse momenta of all tracks (satisfying quality requirements) within a cone of $\Delta R = \min(0.3, 10\ \mathrm{GeV}/p_{\mathrm{T}})$ around the candidate muon. The performance of the muon identification and isolation variables are documented in Ref. [43]. Corrections to the muon momentum scale and resolution are applied to MC simulation to correct for differences between the simulated Monte Carlo and measured data. The correction factors were derived from data/MC simulation comparisons with $Z \to \mu^+\mu^-$ and $J/\Psi \to \mu^+\mu^-$ events.

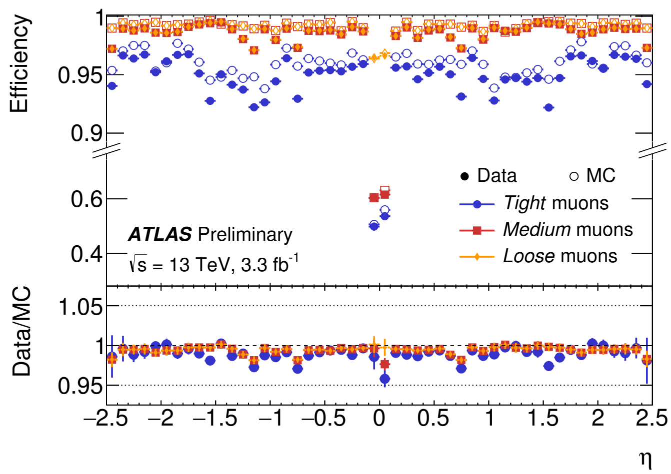

Figure 4.4: The muon reconstruction efficiency as a function of η measured in $Z \to \mu^+\mu^-$ events for muons with p_{T} >10 GeV and measured using collisions recorded with $\sqrt{s} = 8$ TeV. The panel at the bottom shows the ratio between the measured and predicted efficiencies. Efficiencies are shown for three different reconstruction algorithms. The data points labeled 'Medium' correspond to the muons used in the dihiggs analysis presented in Chapter 6.

In order to be considered as a signal muon for the dihiggs analysis presented in Chapter 6, muon candidates must have $p_{\mathrm{T}} > 27$ GeV and should be in the range of $|\eta| < 2.4$. The candidate is required to pass a medium likelihood identification and must pass an isolation requirement of $p_{\mathrm{T}}^{\mathrm{varcone0.3}}$ / $p_{\mathrm{T}} < 0.06$. Figure 4.2 shows the efficiency for three reconstruction algorithms as a function of η for muons measured in $Z \to \mu^+\mu^-$ events recorded at $\sqrt{s} = 13$ TeV. The data points labeled 'Medium' correspond to the muons used in the dihiggs analysis. The reconstruction algorithm is over 99% efficient for the majority of the phase space probed. Additional cuts are placed on muon candidates requiring the significance of the transverse impact parameter ($|d_0^{\mathrm{sig}}|$) to be less than two standard deviations and the $\sin\theta$-weighted longitudinal impact parameter of the muon tack to be less than 0.5 mm from the primary vertex.

4.3 Jets

4.3.1 8 TeV

Jets are reconstructed with the anti-k_t algorithm [44–46] with a radius parameter $R = 0.4$ from calibrated topological clusters [47] built from energy deposits in the calorimeters. Prior to jet finding, a local cluster calibration scheme [48, 49] is applied to correct the topological cluster energies for the effects of non-compensation, dead material and out-of-cluster leakage. The corrections are obtained from simulations of charged and neutral particles. After energy calibration [50] jets are required to have $p_{\mathrm{T}} > 25$ GeV and $|\eta| < 2.5$.

To avoid selecting jets from secondary pp interactions, a selection on the so-called "jet vertex fraction" (JVF) variable above 0.5 is applied to jets with $p_{\mathrm{T}} < 50$ GeV and $|\eta| < 2.4$. This requirement ensures that at least 50% of the sum of the p_{T} of tracks with $p_{\mathrm{T}} > 1$ GeV associated with a jet comes from tracks compatible with originating from the primary vertex. During jet reconstruction, no distinction is made between identified electrons and jet energy deposits. For jets within $\Delta R < 0.2$ of selected electrons, the single closest jet is discarded to avoid double-counting of electrons as jets. After this removal procedure, electrons within $\Delta R < 0.4$ of all remaining jets are removed.

Jets are identified as originating from the hadronization of a b quark (b tagged) via an algorithm [51] using multivariate techniques to combine information from the impact parameters of displaced tracks as well as topological properties of secondary and tertiary decay vertices reconstructed within the jet. The working point used in the 8 TeV W-helicity analysis discussed in Chapter 5 corresponds to a 70% efficiency to tag a b quark jet, with a light jet rejection factor of $\sim$130 and a charm jet rejection factor of 5, as determined for b tagged jets with $p_{\mathrm{T}} > 20$ GeVand $|\eta| < 2.5$ in simulated $t\bar{t}$ events. The simulated b tagging efficiency is corrected to that measured in data using calibrations produced for the 6 bin $t\bar{t}$ PDF calibration (combined_pdf_dijet_7) [52]. This calibration uses a combinatorical likelihood to measure b tagging efficiency in a data sample of dileptonic $t\bar{t}$ events and helps reducing b tagging uncertainties by considering correlations between the measured jets. The total uncertainty on the measured jet p_{T} due to the detector response, jet reconstruction algorithms, and backgrounds due to multiple $p - p$ interactions is found to range from between 1 to 4 % of the total jet p_{T} across the full η of the calorimeters for jets with p_{T} up to 1.7 TeV [53].

4.3.2 13 TeV

Jets are reconstructed from three-dimensional topological calorimeter clusters [54] using the anti-k_t jet algorithm [44] with a radius parameter of 0.4. Jet energies are corrected [55] for detector inhomogeneities, the non-compensating nature of the calorimeter, and the impact of multiple overlapping pp interactions. Correction factors are derived using test beam, cosmic ray, pp collision data, and a detailed Geant4 detector simulation. Jet cleaning is applied to remove events with jets built from noisy calorimeter cells or non-collision backgrounds, requiring that jets are not of "bad" quality [56]. To avoid selecting jets originating from pile-up interactions a "jet vertex tagger" (JVT) criterion is applied for jets with $p_T < 60$ GeV and $|\eta| < 2.5$ requiring a JVT > 0.59 cut.

Signal jets are defined as jets which passes the jet cleaning and JVT criteria and are further required to have $p_{\mathrm{T}} > 20$ GeV and $|\eta| < 2.5$. The ATLAS jet flavor tagging algorithm, the `MV2c10` algorithm [57], is used to select signal events and suppress multi-jet, W+jets, Z+jets and di-boson background. The jets identified as initiated by a b-quark are called b-jets in this note. Out of the possible working points corresponding to different b-tagging efficiencies, the 85% Fixed-Cut working point (WP) is selected as to keep the signal efficiency high. The 85% efficiency for selecting b-jets corresponds with a charm jet rejection factor 3.1 and a light jet rejection factor of 33.5. Signal jets are labeled b-jets if they pass the `MV2c10` 85% WP cut and labeled as light-jets if they fail the cut. The difference in the efficiency of b-tagging between data and simulation is taken into account by applying b-tagging scale factors. The uncertainties associated with b-tagging are considered separately for b-, c- and light-flavor-induced jets. Table 4.1 summarizes the jet selection. The total uncertainty on the measured jet p_{T} due to the detector response, jet reconstruction algorithms, and backgrounds due to multiple $p-p$ interactions is found to range from between 2 to 5 % of the total jet p_{T} across the full η of the calorimeters for jets with p_{T} up to 2 TeV [55].

Table 4.1: Selection for jets with distance parameter $R = 0.4$.

	Signal Jets
Algorithm	anti$-k_t$
p_T	20 GeV
$\|\eta\|$	< 2.5
Quality	not "bad" jet
Pile-up jet removal	JVT > 0.59 when $\|\eta\| < 2.5$ *and* $p_T < 60$ GeV
b-tagging	`MV2c10`, 85% fixed-cut WP, labeled as b-jets pass cut, light-jets if fail cut

4.4 Missing Energy

4.4.1 8 TeV

The missing transverse momentum ($E_{\mathrm{T}}^{\mathrm{miss}}$ or MET) is used to estimate the transverse momentum of an assumed neutrino originating from the decay of W bosons in the $t\bar{t}$ final state. $E_{\mathrm{T}}^{\mathrm{miss}}$ is itself reconstructed by first matching each calorimeter energy cluster with either a reconstructed lepton or jet. Failing this, the cluster is left unassociated. The remaining unassociated clusters are then calibrated for energy losses in un-instrumented regions and for different responses of the calorimeters to electromagnetic and hadronic shower components. This calibration scheme is similar to that described in Ref. [58]. $E_{\mathrm{T}}^{\mathrm{miss}}$ is calculated from a vector sum of the calibrated cluster momenta, together with a term associated with muon momenta. The $E_{\mathrm{T}}^{\mathrm{miss}}$ resolution shown in Figure 3.11, measured in $Z \to \mu^+\mu^-$ events at 8 TeV, ranges from 10-30 GeV for up to $\sim$1 TeV of energy deposited in the calorimeter systems. The black points in Figure 3.11 show the measured resolution as a function of the deposited transverse energy.

4.4.2 13 TeV

The $E_{\mathrm{T}}^{\mathrm{miss}}$ used in the analysis presented in Chapter 6 is computed using the objects passing the 13 TeV electron, muon, and jet object selections described above. Electrons and muons with $p_{\mathrm{T}} >$7 GeV are used in the MET calculation. Leptons with looser identification criteria are also included in the $E_{\mathrm{T}}^{\mathrm{miss}}$ calculation. Photons and hadronically decaying taus are also included in the $E_{\mathrm{T}}^{\mathrm{miss}}$ calculation even though they are not used explicitly in the event reconstruction. A track-based (TST) algorithm [59] is used for the final $E_{\mathrm{T}}^{\mathrm{miss}}$ calculation. Figure 4.5 shows the resolution of the track-based algorithm as a function of the measured transverse energy in measured a sample of $Z \to \mu^+\mu^-$ events corresponding to an integrated luminosity of 6 pb^{-1}. With the data collected, the $E_{\mathrm{T}}^{\mathrm{miss}}$ resolution varies between 10 and 25 GeV as a function of the measured transverse energy.

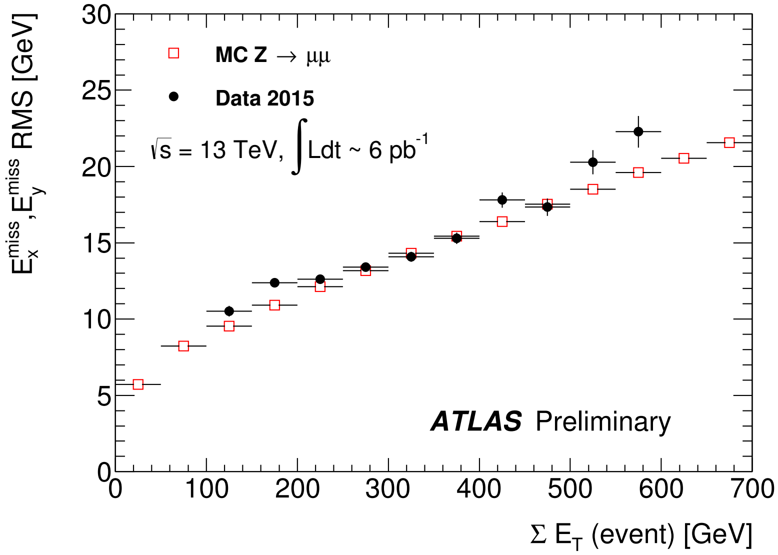

Figure 4.5: Resolution of the track-based missing energy calculation in the x and y directions as a function of the total transverse energy measured in the calorimeter and muon systems in $Z \to \mu^+\mu^-$ events measured at $\sqrt{s} = 13$ TeV.

Chapter 5
Measuring W-Helicity in $t\bar{t}$

> Just because things get a little dingy at the subatomic level doesn't mean all bets are off.
>
> - Murray Gell-Man

5.1 Introduction

Discovered in 1995 at the Tevatron [22, 23], the top quark is the heaviest particle in the Standard Model of particle physics. In proton-proton collisions at the LHC [27], top quarks are produced in pairs through the strong interaction and individually through electroweak processes. With a mass of 173.34 $\pm$ 0.76 GeV [60] (close to the electroweak symmetry breaking scale [61][3]), measurements of the top quark properties can provide important tests of the Standard Model. Due to its extremely short lifetime ($\sim 10^{-25}$ seconds), the top quark decays before hadronization, passing its spin information to the decay products. The top quark decays almost exclusively into a W boson and a b quark, and thus studying the Wtb vertex is of importance in the search for new interactions.

The W boson can be produced with left-handed, longitudinal, or right-handed helicity. The SM predictions for the W boson helicity fractions at next-to-next-to-leading-order (NNLO) in the strong coupling constant, including the finite b quark mass and electroweak effects, are $F_0 = 0.687 \pm 0.005$, $F_\mathrm{L} = 0.311 \pm 0.005$, and $F_\mathrm{R} = 0.0017 \pm 0.0001$ [62] for a bottom quark mass $m_b = 4.8$ GeV and a top quark mass $m_t = 172.8 \pm 1.3$ GeV. These fractions can be extracted from measurements of the angular distribution of the decay products of the top quark. The helicity angle θ^* is defined [63] as the angle between the momentum direction of the charged lepton (down-type quark) from the decay of the leptonic (hadronic) W boson and the reversed momentum direction of the b quark from the decay of the top quark, both boosted into the W boson rest frame. The distribution of the cosine

[3] The electroweak symmetry breaking scale is of order $\sim$100 GeV.

of the helicity angle has a dependence on the helicity fractions given by

$$\frac{1}{N}\frac{dN}{d\cos\theta^*} = \frac{3}{8}(1-\cos\theta^*)^2 F_{\mathrm{L}} + \frac{3}{4}\sin^2\theta^* F_0 + \frac{3}{8}(1+\cos\theta^*)^2 F_{\mathrm{R}}, \tag{5.1}$$

The helicity fractions, F_{i}, can then be extracted via a fit of the reconstructed $t\bar{t}$ candidate events measured in data.

A kinematic likelihood fit is used to determine the best association of b jets, light jets, and lepton candidates to the top quark and anti-quark decay hypotheses, considering the momentum imbalance as the existence of a neutrino originating from the leptonically decaying W boson. Both ATLAS [64] and CMS [65] produced 7 TeV measurements using leptonically decaying W's in semileptonic $t\bar{t}$ decays. CMS also produced a measurement at 8 TeV [66] using the leptonically decaying W bosons produced in semileptonic $t\bar{t}$ events. For this analysis, the helicity fractions were measured using both the leptonically and hadronically decaying W's from the $t\bar{t}$ decay in both the electron and muon channels. While previous analyses from D0 [67] and CMS [65] have performed indirect helicity measurements using the hadronic W decay in semileptonic $t\bar{t}$ events, this analysis is the first to perform this measurement directly by identifying the identities (up type or down type) of the daughter jets from the hadronic W decay.

After event selection and reconstruction, the helicity fractions were measured using a template fit method. Signal and background templates were generated using Monte Carlo (MC) simulation except for contributions from mis-identified leptons (QCD processes) which were generated via a data-driven method. Pure helicity templates for the signal sample were obtained from using a Monte Carlo re-weighting procedure described in Section 5.5. The final fit to data was performed using a binned likelihood fit.

5.2 Event Selection

This analysis is based on data collected by the ATLAS experiment in pp collisions at $\sqrt{s}$ = 8 TeV between April and October 2012. The corresponding integrated luminosity is 20.2 fb^{-1}. Only events collected using a single electron or single muon trigger under stable beam conditions and for which all detector subsystems were fully operational were considered.

The p_{T} thresholds are 24 or 60 GeV for electrons (logical OR of EF_e24vhi_medium1 and EF_e60_medium1 trigger chains) and 24 or 36 GeV for muons (logical OR of EF_mu24i_tight and EF_mu36_tight trigger chains). The triggers with the lower p_{T} threshold include isolation requirements on the candidate lepton, resulting in inefficiencies at high p_{T} that are recovered by the triggers with higher p_{T} threshold. The triggers use similar but looser selection criteria than the final reconstruction requirements.

Events passing the trigger are required to have at least one reconstructed vertex with at least five associated tracks, consistent with the beam collision region in the $x - y$ plane. If more than one vertex is found, the primary vertex is taken to be the vertex with the largest scalar sum of transverse momenta from its associated tracks. Events are discarded if any jet with $p_{\mathrm{T}} > 20$ GeV is independently identified as out-of-time activity from a previous pp collision or as calorimeter noise [68].

In order to pick up semileptonic $t\bar{t}$ decays, events are required to have exactly one reconstructed electron or muon with $p_{\mathrm{T}} > 25$ GeV and at least four jets satisfying the quality and kinematic criteria discussed in Section 4.3.1. The remaining events are separated into two independent b tag regions: one with exactly one b tag and one with two or more b tags. For both electron and muon channels, the selected lepton is required to match ($\Delta R < 0.15$) the lepton reconstructed by the high-level trigger.

Since the background from multi-jet production is very small in the high jet and b tag multiplicity regions which are the focus of this analysis, no requirements on the $E_{\mathrm{T}}^{\mathrm{miss}}$ or transverse mass of the W boson are applied for the inclusive region with 2 or more b tags. In the 1 exclusive b tag region, the $E_{\mathrm{T}}^{\mathrm{miss}}$ is required to be greater than 20 GeV and the sum of $E_{\mathrm{T}}^{\mathrm{miss}}$ and transverse mass of the leptonic W boson is required to be greater than 60 GeV in order to suppress multi-jet (QCD) backgrounds coming from the presence of misidentified leptons.

Selected events are categorized into 1 exclusive and 2 b tag inclusive regions. Event yields for both lepton channels and b tag regions are shown in Table 5.1. Cutting on the log likelihood (discussed in Sec. 5.4.5) significantly reduces background contributions and improves the data/prediction agreement. Studies on optimizing the sensitivity of the W helicity measurement using a cut on the likelihood are presented in Sec. 5.4.5. Plots showing data/prediction comparisons after event selection and log likelihood cut for both lepton channels and b tag regions are shown in Figures 5.1-5.4. Control plots for the pre-fit $cos\theta^{*}$ distributions are shown in Figure 5.5 for both the 2 inclusive and 1 exclusive b tag regions.

The largest shape difference between the leptonic and hadronic angles in Figure 5.5 is due to the fact that for events with $\cos\theta^{*} \sim -1$, the charged lepton (down-type quark) is emitted parallel to the b-jet, and more leptonic events fail the lepton p_{T} and lepton-b-jet isolation requirements imposed by the event selection. This affects the leptonic side more than the hadronic side since there is no corresponding jet-b-jet isolation requirement. Another noticeable difference between the 1 exclusive and 2 inclusive shapes around $\cos\theta^{*} \sim +1$ is where the neutrino (up-type quark) and b-jet are parallel in the mother W boson rest frame, so the MET cut in the 1 exclusive region causes some events to fail the selection criteria. Lastly, the hadronic $\cos\theta^{*}$ distribution in the 1 exclusive region suffers from an additional light jet/b-jet quark mismatch which results in the double peak structure.

e+jets	No Likelihood Cut		Log(Likelihood) > -48	
Sample	1 b tag	≥ 2 b tags	1 b tag	≥ 2 b tags
$t\bar{t}$	69822 ± 4490	74467 ± 4788	36495 ± 2347	36028 ± 2317
Single top	5553 ± 944	3682 ± 626	1996 ± 339	974 ± 166
W + light	2498 ± 125	104 ± 7	600 ± 30	24 ± 1
W + c	4490 ± 1123	274 ± 64	1212 ± 303	54 ± 13
W + bb/cc	12040 ± 843	2866 ± 134	2726 ± 191	538 ± 38
Z + jets	3847 ± 1847	1281 ± 615	1200 ± 576	329 ± 158
Diboson	808 ± 388	176 ± 84	215 ± 103	33 ± 16
QCD	6862 ± 2059	2054 ± 616	2272 ± 682	447 ± 134
Total expected	105920 ± 5553	84904 ± 4871	46716 ± 2561	38426 ± 2332
Data	102591	89414	45246	40045
Dev. %	3.2	-5.0	3.2	-4.0

μ+jets	No Likelihood Cut		Log(Likelihood) > -48	
Sample	1 b tag	≥ 2 b tags	1 b tag	≥ 2 b tags
$t\bar{t}$	87405 ± 5620	92321 ± 5936	43597 ± 2803	42634 ± 2741
Single top	6717 ± 1142	4464 ± 759	2328 ± 396	1102 ± 187
W + light	3296 ± 165	177 ± 11	761 ± 38	45 ± 2
W + c	5556 ± 1389	329 ± 77	1439 ± 360	51 ± 13
W + bb/cc	16386 ± 1147	4098 ± 191	3520 ± 246	780 ± 55
Z + jets	2445 ± 1174	744 ± 357	606 ± 291	158 ± 76
Diboson	924 ± 444	185 ± 89	214 ± 103	37 ± 18
QCD	5280 ± 1584	1457 ± 437	1746 ± 524	323 ± 97
Total expected	128009 ± 6344	103775 ± 6019	54211 ± 2928	45130 ± 2751
Data	126333	108131	53747	46048
Dev. %	1.3	-4.0	0.9	-2.0

Table 5.1: Event yields in the electron (top) and muon channel (bottom) for 1 exclusive and 2 inclusive b tag regions after event selection. Errors on the Monte Carlo yields come from the uncertainties in the normalization of each sample. The last two columns refers to the yields after applying the likelihood cut. Details are given in 5.4.5

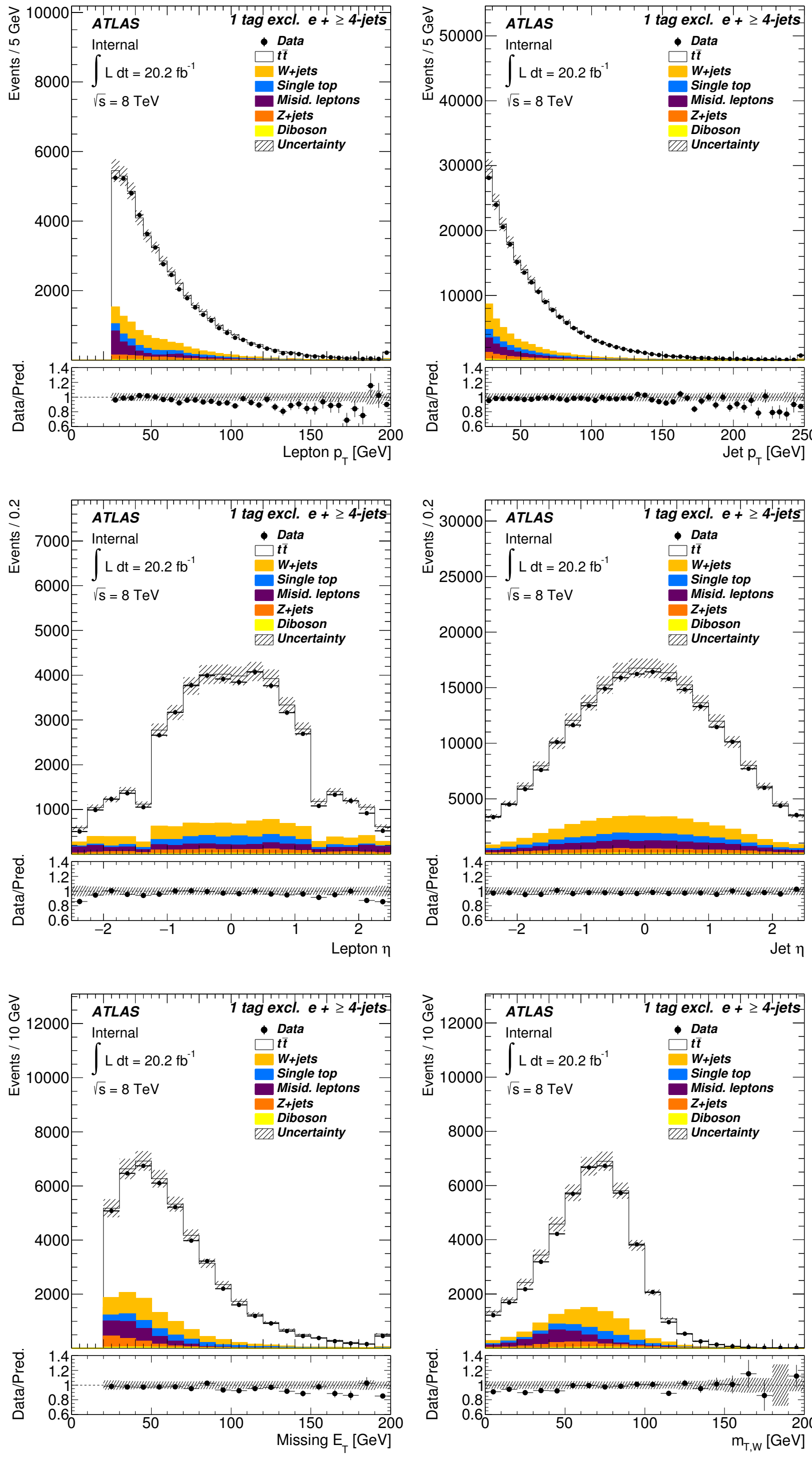

Figure 5.1: Plots showing data/MC agreement after event selection for reconstructed objects (lepton, jets, neutrino) in the 1 exclusive b tag, electron region. The shaded bands represent the Monte Carlo statistical uncertainties.

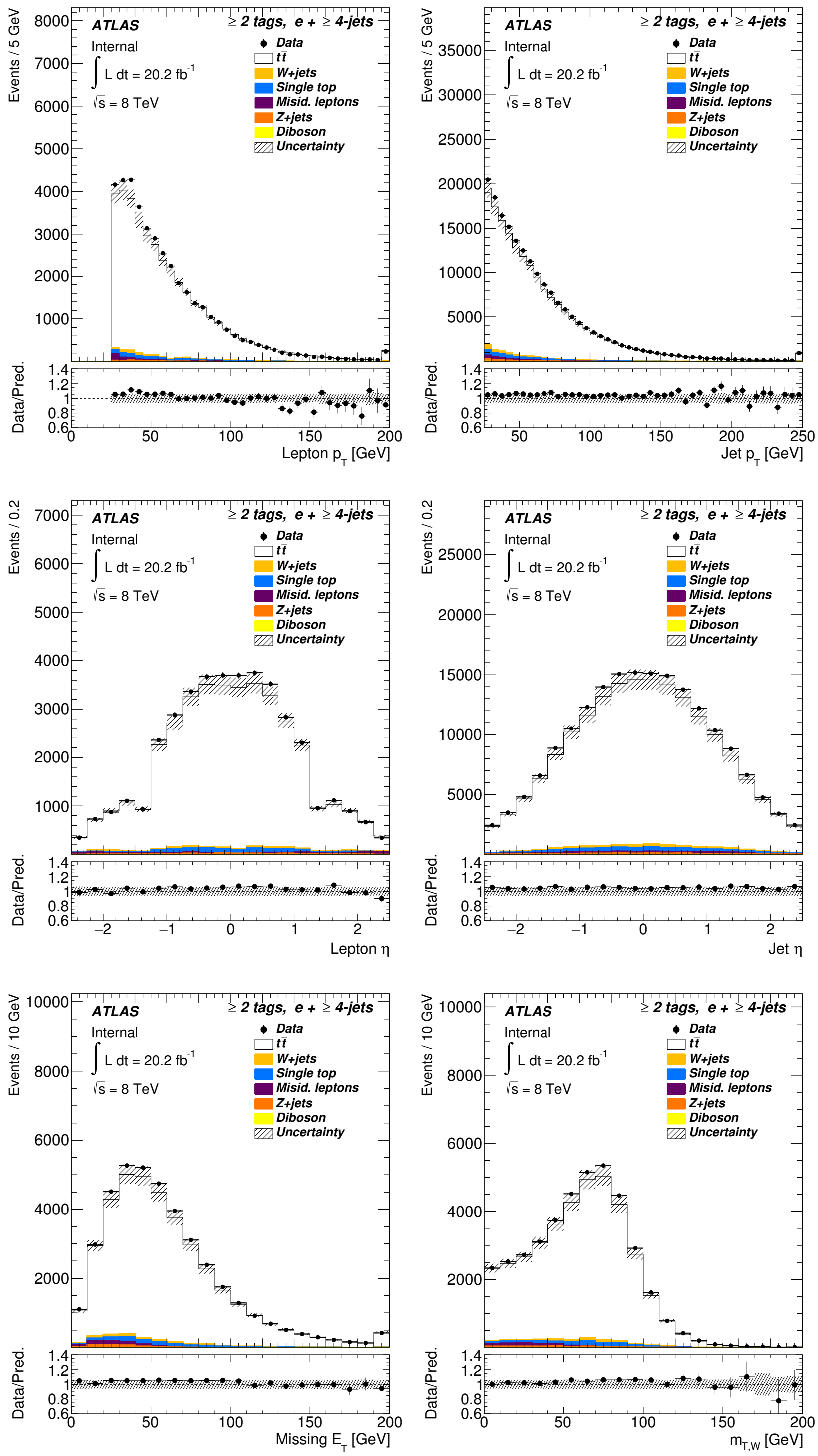

Figure 5.2: Plots showing data/MC agreement after event selection for reconstructed objects (lepton, jets, neutrino) in the 2 inclusive b tag, electron region. The shaded bands represent the Monte Carlo statistical uncertainties.

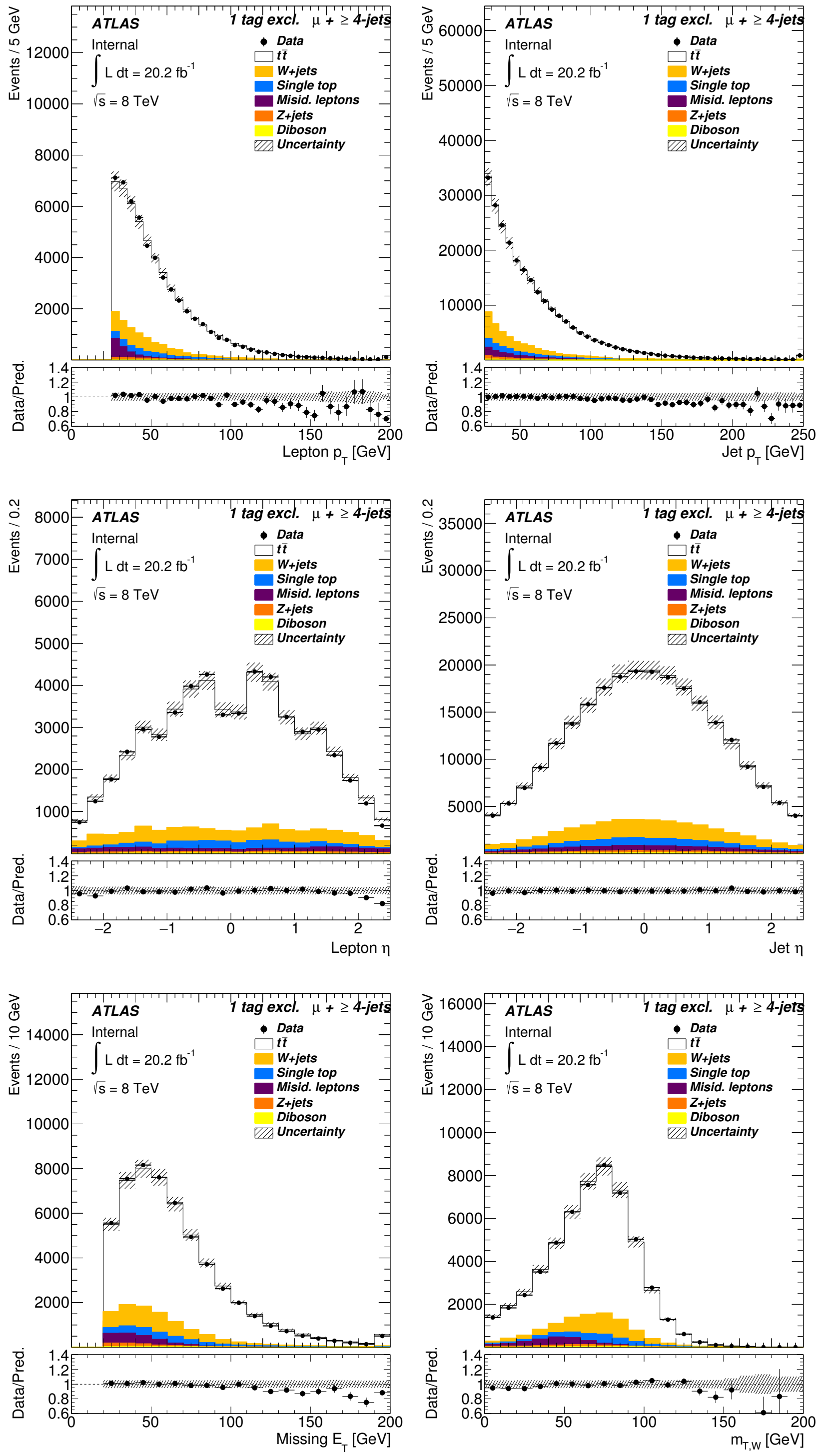

Figure 5.3: Plots showing data/MC agreement after event selection for reconstructed objects (lepton, jets, neutrino) in the 1 exclusive b tag, muon region. The shaded bands represent the Monte Carlo statistical uncertainties.

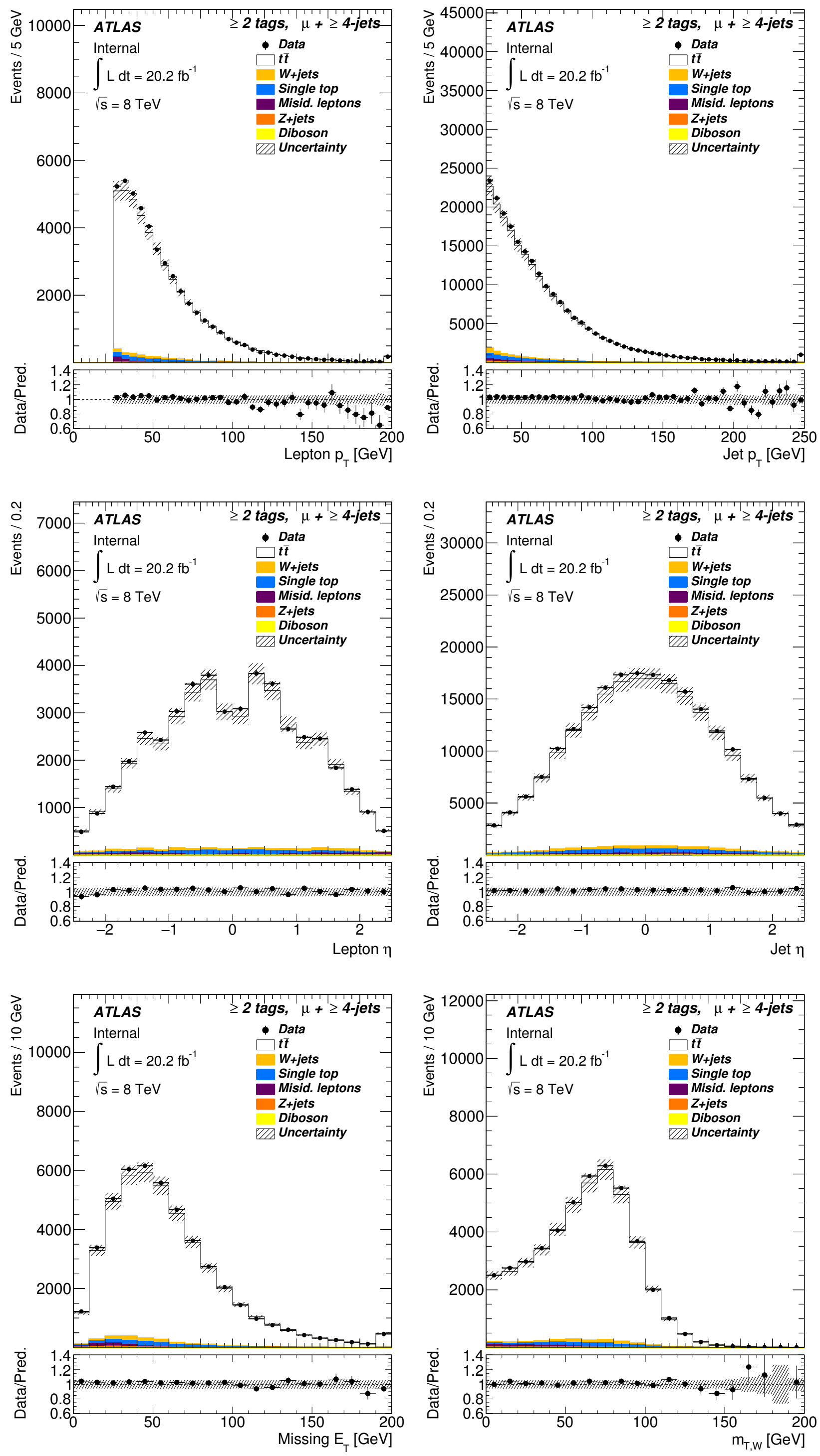

Figure 5.4: Plots showing data/MC agreement after event selection for reconstructed objects (lepton, jets, neutrino) in the 2 inclusive b tag, muon region. The shaded bands represent the Monte Carlo statistical uncertainties.

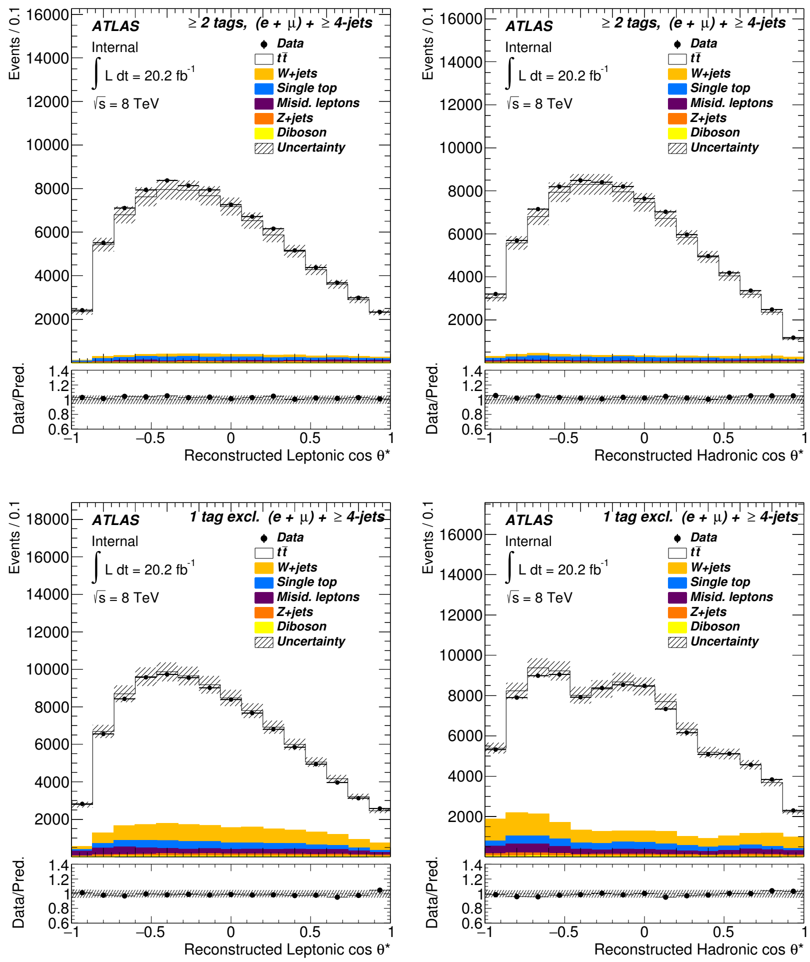

Figure 5.5: Plots showing data/MC agreement after event selection and after the likelihood cut for leptonic and hadronic $\cos\theta^*$ in the 2 inclusive b tag (top) and 1 exclusive b tag (bottom) region. All plots show merged electron+muon data and Monte Carlo. The shaded bands represent the Monte Carlo statistical uncertainties.

5.3 Background and Signal Modeling

After event selection, the largest remaining background comes from the production of a W boson in association with jets (W+jets) with multi-jet QCD production contributing to a lesser extent. Small contributions arise from single top quark, Z+jets and diboson (WW, WZ, ZZ) production. The absolute yield of all considered backgrounds rises in the 1 exclusive b tag region while the contributions from single top and W+jets backgrounds also increase relatively with respect to the other backgrounds.

Multi-jet events contribute to the selected sample via the mis-identification of a jet or a photon as an electron or the presence of a non-prompt lepton, e.g. from a semileptonic b- or c-hadron decay, and the corresponding yield is estimated using a data-driven matrix method [69].

Small background contributions coming from single top quark, Z+jets and diboson production are estimated from simulation and normalized to their theoretical cross sections.

Samples of W/Z+jets events at 8 TeV are generated using the Alpgen v2.14 [70] leading-order (LO) generator and the CTEQ6L1 PDF set [71]. Parton shower and fragmentation are modeled with Pythia 6.425 [72] for W+jets and Z+jets production. To avoid double-counting of partonic configurations generated by both the matrix-element calculation and the parton-shower evolution, a parton-jet matching scheme ("MLM matching") [73] is employed. Since final states with hadronic Z decays of WZ are missing in Alpgen+Herwig production, Sherpa samples generated with massive b and c quarks (i.e. b and c quark masses are set to their PDG values in the matrix element calculation as opposed to being set massless) are used for these decay modes.

The W +jets samples are generated with up to five additional partons, separately for W+light jets, $Wb\bar{b}$+jets, $Wc\bar{c}$+jets, and Wc+jets. The overlap between $Wq\bar{q}$ ($q = b, c$) events generated from the matrix element calculation and those generated from parton-shower evolution in the W+light jet samples is removed by using the angular separation between the extra heavy quarks: if $\Delta R(q, \bar{q}) > 0.4$, the matrix-element prediction is used, otherwise the parton-shower prediction is used. The W+jets background is normalized using data-driven calibration factors which take into account the charge of the lepton and heavy flavor components of the associated jets. The method and factors were derived in the 8 TeV ATLAS $t\bar{t}$ charge asymmetry analysis [74].

The Z+jets background is generated using the Alpgen v2.14 [70] leading-order (LO) generator with up to five additional partons separated by different parton flavors and is normalized to the inclusive NNLO theoretical cross section [75].

The $WW/WZ/ZZ$+jets samples are generated using Sherpa with up to three additional partons in the hard process and are normalized to their NLO theoretical cross sections [76]. Heavy flavor quarks (b and c) are treated as massive in the matrix element calculation and generation of all diboson samples.

The $t\bar{t}$ sample is generated using POWHEG NLO generator [77–79] with the CT10 PDF set assuming a top quark mass of 172.5 GeV and setting the h_{damp} factor (the parameter responsible for high p_{T} radiation damping in the POWHEG-BOX generator) equal to the top quark mass. POWHEG is interfaced to PYTHIA 6.425 [72] with the CTEQ61L set of parton distribution functions and Perugia2011C underlying event tune. The sample is normalized to the theoretical calculation performed at next-to-next-to leading order (NNLO) in QCD including resummation of next-to-next-to-leading logarithmic (NNLL) soft gluon terms with top++2.0 [24,80–84]. At 8 TeV, the $t\bar{t}$ cross-section is calculated to be 253^{+15}_{-16} pb.

Effects due to PDF variations, choice of α_S, and the input top quark mass are taken as systematic uncertainties. The PDF and α_S uncertainties are calculated using the PDF4LHC prescription [17] with the MSTW2008 68% CL NNLO [12, 13], CT10 NNLO [14, 15] and NNPDF2.3 5f FFN [16] PDF sets added in quadrature to the scale uncertainty. Unlike multi-leg generators, POWHEG is expected to describe jet multiplicity properly only for $t\bar{t}$ accompanied by up to two jets. Nevertheless when interfaced with PYTHIA, POWHEG provides good description of jet multiplicity in data up to much higher jet multiplicities and reproduces the associated heavy flavor fraction in $t\bar{t}$ production despite the fact that heavy flavor component originates only from the parton shower [85].

Samples of single top quark backgrounds corresponding to the s-channel, t-channel and Wt production mechanisms are generated with POWHEG [77–79] using the CT10 PDF set [86]. In the case of the Wt-channel, the nominal sample uses a diagram removal approach to handle the interference arising at NLO. All samples are interfaced to PYTHIA 6.425 [72] with the CTEQ61L set of parton distribution functions and Perugia2011C underlying event tune. Overlaps between the $t\bar{t}$ and Wt final states are removed [87]. The single top quark samples are normalized to the approximate NNLO theoretical cross sections [88, 89] using the MSTW2008 NNLO PDF set.

All event generators using HERWIG are also interfaced to JIMMY v4.31 [90] to simulate the underlying event. All simulated samples utilize PHOTOS 2.15 [91] to simulate photon radiation and TAUOLA 1.20 [92] to simulate τ decays. All simulated samples (including the $t\bar{t}$ signal) include multiple pp interactions and are processed through a simulation [93] of the detector geometry and response using GEANT4 [94]. All simulated samples are processed through the same reconstruction software as the data. Simulated events are corrected so that the object identification efficiencies, energy scales and energy resolutions match those determined in data control samples.

Table 5.2 provides a summary of basic parameters of the MC samples used in the analysis.

Sample	Generator	PDF	Shower	Normalization
$t\bar{t}$ + jets	Powheg	CT10	Pythia 6.425	NNLO+NNLL [95–97]
W + jets	Alpgen	CTEQ6L1	Pythia 6.426	8 TeV charge asymmetry CAs [74]
Z + jets	Alpgen	CTEQ6L1	Pythia 6.426	NLO [98]
Single top (s-channel, Wt)	Powheg	CT10	Pythia 6.426	aNNLO [99–101]
Single top (t-channel)	Powheg	CT10	Pythia 6.427	aNNLO [99–101]
Diboson	Sherpa	CT10	Sherpa	NLO [102]

Table 5.2: A summary of basic generator parameters used to simulate various processes

5.4 Event Reconstruction

A kinematic fitting technique is used to reconstruct candidate events passing basic selection requirements and identify optimal jet assignments. The following section details the methodology of the kinematic fit as well as extensions that use information beyond object kinematics in order to produce the final jet assignments. A number of different configurations are studied in order to determine the optimal setup to extract the helicity fractions.

5.4.1 Kinematic Fitting

The events are reconstructed using a kinematic likelihood code package (KLFitter) [103] which makes use of the Bayesian Analysis Toolkit (BAT) [104]. KLFitter takes an input model (e.g., $t\bar{t}$ decay) and mass constraints (m_t, m_W) on composite objects built from the input leptons, $E_{\mathrm{T}}^{\mathrm{miss}}$, and jets to map the input particles to leading order partons/leptons from the $t\bar{t}$ decay. Transfer functions are used to float the measured energies of the jets and lepton within detector resolutions. Separate transfer functions are defined for jets/leptons/$E_{\mathrm{T}}^{\mathrm{miss}}$ in different η ranges, but the measured angles themselves are assumed to be correctly reconstructed. The final two and three-body masses are evaluated with Breit-Wigner PDFs using $m_t = 172.5$ GeV and $m_W = 80.2$ GeV. The Breit-Wigner widths are set to $\Gamma_t = 1.33$ GeV and $\Gamma_W = 2.1$ GeV for the top quark and W boson respectively. The final expression for likelihood, $\mathscr{L}$, is then expressed as

$$\mathscr{L} = BW(m_{q_1q_2q_3}|m_t\Gamma_t) \cdot BW(m_{q_1q_2}|m_W\Gamma_W) \cdot BW(m_{q_4\ell\nu}|m_t\Gamma_t) \cdot BW(m_{\ell\nu}|m_W\Gamma_W)$$
$$\prod_{i=1}^{4} W_{jet}(E_i^{meas}|E_i) \cdot W_\ell(E_\ell^{meas}|E_\ell) \cdot W_{miss}(E_x^{miss}|p_x^\nu) \cdot W_{miss}(E_y^{miss}|p_y^\nu). \quad (5.2)$$

where q_i ($i = 1, 2, 3, 4$) are the labels for the four jets used in the calculation, $W_i(E_x^{meas}|E_i)$ are the transfer functions, E_x^{meas} is the measured energy of object x, E_i is the 'true' energy of the reconstructed parton i, and the $BW(m_{ij(k)}|m_Y\Gamma_Y)$ are the Breit-Wigner functions used to evaluate the masses of composite reconstructed particles with respect to the mass and width of particle Y.

Section 5.4.2 provides an in-depth discussion about the construction and use of the transfer functions. Permuting the jets in an event through all positions in the model hypothesis yields different values for each permutation according to Eq. 5.2. To increase the ability of KLFitter to correctly identify the assignments for each jet, additional information (e.g. b tagging, differences between types of light jets) can be used to improve the likelihood that a given permutation is correct. This information can be used to extend the likelihood definition of Eq. 5.2 into an event probability. This extension is fully discussed in Sec. 5.4.3.

After the likelihood (and/or event probability) of each permutation is calculated, the results are ordered, and the best permutation (defined as the permutation with the highest event probability) is selected for measuring the angles necessary to extract the helicity fractions. Reconstructed distributions from the leading permutation after a log likelihood cut of > -48 (abbreviated as 'LH > -48' in the following) are shown in Figs 5.6-5.9. The optimization and choice of the log likelihood cut is discussed in Section 5.4.5. Good agreement between data and prediction is observed in all signal regions.

5.4.2 Transfer Functions

The transfer functions (TF) used in the kinematic fitter are derived for electrons, muons, light jets, b jets, and $E_{\mathrm{T}}^{\mathrm{miss}}$ using the 8 TeV $t\bar{t}$ MC sample described in Section 5.3. The difference between reconstructed energy and truth-level energy is fit using a double Gaussian functional form to determine the detector response for jets and electrons. A double Gaussian functional form was chosen in order to allow for the modeling of asymmetric tails in the detector response. The functional form of the transfer functions is given by

$$W(\Delta E) = \frac{1}{\sqrt{2\pi}(p_2 + p_3 p_5)} \left[e^{\frac{-(\Delta E - p_1)^2}{2p_2^2}} + p_3 \cdot e^{\frac{-(\Delta E - p_4)^2}{2p_5^2}} \right] \tag{5.3}$$

where $\Delta E = \frac{E_{truth} - E_{reco}}{E_{truth}}$, and the parameters p_i depend on the energy of the parton/lepton are parameterized depending on the parton/lepton type. As the best guess at leading order, a linear dependence is assumed. If another dependence is known by a physical motivation, the paramterization is adapted correspondingly. For example, in the case of jets and electrons, p_2 represents the calorimeter resolution and is hence parameterized as $\sim 1/\sqrt{E}$. If the linear assumption fails, it can also be replaced by heuristically determined parameterizations. In the case of electrons and jets, the parameterizations are

$$p_1 = a_1 + b_1 \cdot E_{truth} \tag{5.4}$$

$$p_2 = a_2/\sqrt{E_{truth}} + b_2 \tag{5.5}$$

$$p_3 = a_3 + b_3 \cdot E_{truth} \tag{5.6}$$

$$p_4 = a_4 + b_4 \cdot E_{truth} \tag{5.7}$$

$$p_5 = a_5 + b_5 \cdot E_{truth} \tag{5.8}$$

The a_i's and b_i's are obtained from a global fit to each particle species and η region. For muons, E_{truth} is replaced with p_T^{truth}, and all p_i are parameterized linearly, i.e. Equation 5.5 becomes $p_2 = a_2 + b_2 \cdot E_{truth}$.

Only reconstructed objects that are bi-uniquely (one and only one matching for both objects) matched to partons from the hard decay are used to derive the transfer functions. An object is considered matched if the ΔR between the reconstructed and truth object is less than 0.3. The matching efficiencies for jets are (unsurprisingly) dependent on the jets fed into the kinematic fitter, and these efficiencies are discussed further in Sec. 5.4.4.

As the detector response changes in different regions of the detector and for particles with different energy ranges, a number of transfer functions are defined for each particle species and binned in terms of η and p_{T}.

5.4.3 Hadronic Flavor Separation

Directly extracting helicity fractions using the hadronic W decay requires a correct reconstruction and identification of the flavor of the daughter jets. Since the W and top masses for the hadronically decaying top are invariant under a permutation of the W-daughter jets, a quantity including information beyond the kinematics is necessary to correctly assign the identities of all four jets in the hard $t\bar{t}$ decay. This new quantity is called the event probability, and for a given permutation, i, is given by

$$p_i = \frac{\mathcal{L}_i \prod_j \Delta p_{i,j}}{\sum_i \mathcal{L}_i \prod_j \Delta p_{i,j}} \tag{5.9}$$

where the $\Delta p_{i,j}$'s are extensions or weights for each jet, j, in permutation i which are convoluted with the likelihood in order to take advantage of information beyond the invariant masses of the candidate W and top objects, e.g. the b tagging (MV1) weight of the jets. A simple extension using b tagging information would be to apply a binary weight of 1(0) depending on whether a jet permuted into the position of a b jet has an MV1 weight larger(smaller) than a predefined threshold, e.g.

$$\Delta p_{i,j} = \begin{array}{l} 0 \text{ if jet position is for } b \text{ jet and input jet is not } b \text{ tagged} \\ 1 \text{ if position is for } b \text{ jet and input jet is } b \text{ tagged} \end{array} \tag{5.10}$$

To extract the helicity fractions in the hadronic channel, an extension must be defined that takes advantage of information that can distinguish between the up and down type jets of the W decay. The p_{T} of the light jets can be used to separate up-type from down-type jets since the $V-A$ structure of the Wtb vertex predicts an imbalance in their energies [105,106]. This difference is the most pronounced in the top rest-frame, but differences between the measured jet p_{T}'s are also observable in the lab-frame and are simpler to use. The jet p_{T} shapes for different flavor types are shown in Figure 5.10, but the separation power from this effect alone is quite small.

The MV1 weights of the two light jets are also be used to discriminate between up and down type jets. Compared to jets coming from u, d, and s quarks, jets coming from c quarks have, on average, considerably higher MV1 weights. This discrimination is observable in Figure 5.10. W bosons decaying via $W \to c\bar{s}$ (about 50 % of all hadronically decaying W bosons) allow the MV1 information to help identify light jet flavors in a large number of reconstructed events.

Using both of these variables, an extension for separating up and down type jets ('u/d separation') can be calculated using templates of the reconstructed jet p_{T} and MV1 distributions. This approach follows the path taken by the 7 TeV ATLAS measurement of spin correlation in semileptonic $t\bar{t}$ events [107]. The templates were created for up-type $(q = u, c)$, down-type $(q = d, s)$, and b jets $(q = b)$ using the 8 TeV $t\bar{t}$ Monte Carlo signal sample. The reconstructed jets must be bi-uniquely matched $(\Delta R \leq 0.3)$ to one of the quarks produced in the $t\bar{t}$ decay in order to counted in the templates. Using these templates, the product of the probability extensions for all jets in one fit is formally given as

$$\Delta p_{i,\text{u/d sep}} = \mathrm{P}^{\text{ b-type}}(p_{\mathrm{T}}^{\text{blep}}) \cdot \mathrm{P}^{\text{ b-type}}(MV1^{\text{ blep}}) \cdot \mathrm{P}^{\text{ b-type}}(p_{\mathrm{T}}^{\text{bhad}}) \cdot \mathrm{P}^{\text{ b-type}}(MV1^{\text{ bhad}}) \cdot \tag{5.11}$$

$$\mathrm{P}^{\text{ u-type}}(p_{\mathrm{T}}^{\text{u-jet}}) \cdot \mathrm{P}^{\text{ u-type}}(MV1^{\text{ u-jet}}) \cdot \mathrm{P}^{\text{ d-type}}(p_{\mathrm{T}}^{\text{d-jet}}) \cdot \mathrm{P}^{\text{ d-type}}(MV1^{\text{ d-jet}}) \tag{5.12}$$

where $P()$'s represent the probability of a particular jet to have its measured values of p_{T} and MV1 given the jet assignment (b from leptonic top (blep), b from hadronic top (bhad), u-jet, d-jet) in the current permutation. The individual jet weights are calculated using the templates in Figure 5.10 normalized to unity. Using these weights, the event probability is calculated for each permutation. The permutation with the highest event probability is then chosen as the final permutation for the extraction of the helicity angles for both W's from the $t\bar{t}$ decay. Dedicated linearity tests were performed to check whether the use of templates based on the p_{T} of the jets introduces a bias for left-handed events. The hadronic

Configuration	ℓ+jets
4-jet simple	0.260
5-jet simple	0.292
5-jet advanced	0.323

Table 5.3: Matching efficiencies for different KLFitter input jet configurations. An event is considered matched if all four truth jets from the hard $t\bar{t}$ decay are bi-uniquely matched (within a $\Delta R \leq 0.3$) to four reconstructed jets of the leading KLFitter permutation.

linearity tests were found to perform well under closure, and no bias was observed.

5.4.4 KLFitter Optimization Study

The efficiency of the kinematic fitting to correctly identify jet assignments relies on the jets available for permutation. Since each position is unique in the u/d separation configuration (even though swapping the positions of the light jets from W decay is invariant under the W mass constraint), supplying KLFitter with n jets requires the likelihood calculation for $n!$ permutations. The optimal jet input configuration should maximize the matching efficiency of the reconstruction while balancing the CPU time required for each event. The matching efficiency is defined as

$$\epsilon_{\text{match}} = N^{\text{match}}_{\text{events}} / N^{\text{total}}_{\text{events}} \tag{5.13}$$

where $N^{\text{match}}_{\text{events}}$ can be defined in many ways (e.g. correctly matching all four jets, correctly matching only the three jets necessary for the hadronic angle, correctly matching only the b jets, etc.). In the following discussion, an event is considered matched for the leptonic angle when both b jets be correctly matched while all four jets are required to be correctly matched in in the hadronic case. Using these definitions, the final matching efficiencies are computed for both channels to find the optimal jet input configuration.

Many previous ATLAS $t\bar{t}$ analyses use the four leading jets in p_{T} as input to reconstruct the $t\bar{t}$ system. The simplest extension is increasing the number of input jets to five. In this case, the fitter will iterate through $5! = 120$ permutations. Another option is to change the ordering by which jets are chosen to be included in the fit. In the 8 TeV ATLAS measurement of $t\bar{t}$ charge asymmetry [74], the two jets (taken from all jets passing object selection in the event) with the highest MV1 weights are selected, and then the remaining jets are re-ordered in p_{T} and the three highest taken as input.

For this analysis, three different input configurations were studied: four leading jets in p_{T} (4-jet simple), five leading jets in p_{T} (5-jet simple), two leading jets in MV1 + three highest p_{T} jets remaining (5-jet advanced). The results are presented in Table 5.3.

Since the 5-jet advanced configuration was found to have the highest efficiency and the computing time required was reasonable, it was chosen as the final configuration for the extraction of the helicity fractions in both the leptonic and hadronic channels.

5.4.5 Optimizing hadronic sensitivity

Helicity fractions extracted from the hadronic W decay are less sensitive than the corresponding fractions extracted from the leptonic W decay since the daughter down-type jet is, in general, harder to correctly identify than a charged lepton (electron or muon). If the u/d separation procedure detailed in Section 5.4.3 were 100% efficient, the pure helicity templates for the hadronic decay (Figure 5.13) would be expected to follow the theoretical curves for pure helicity states as in the case of the leptonic templates (Figure 5.12). Incorrectly assigned jets (and swapping between the two hadronic W daughters) lead to left-handed and right-handed templates that closely resemble one another other.

Selecting a subset of reconstructed events which contain a relatively higher fraction of correctly matched events should provide a larger separation between hadronic signal templates and lead to a more sensitive result. To this end, four categories of $t\bar{t}$ reconstruction are defined, and the resulting categories plotted to identify regions with higher proportions of correctly matched events:

- **Right**: All 4 jets uniquely truth-matchable, fed into KLFitter, and correctly assigned in the leading permutation
- **Wrong**: All 4 jets uniquely truth-matchable, fed into KLFitter, but not correctly assigned in the leading permutation
- **Non-reco**: Due to acceptance loss or non-unique matching, not all four jets from the hard $t\bar{t}$ decay can be matched to reconstructed objects
- **Bkg**: Dileptonic or tauonic $t\bar{t}$ decays where no true hadronic angle exists

In Figure 5.11, the $t\bar{t}$ distributions for the event probability and log likelihood are broken into the above categories and shown for the leading KLFitter permutation in the electron channel. Both plots are normalized to the total $t\bar{t}$ yield from the 2012 dataset.

While there is no region with clear concentration of correctly matched $t\bar{t}$ in the event probability distribution, correct matched events are concentrated in the log likelihood distribution above values of -55.

To optimize the statistical sensitivity of the hadronic templates, several fits in the two inclusive b tag region were performed scanning across a number of cuts on the log likelihood of the best permutation. The template fitting method used to study the effect of the likelihood cuts on the statistical sensitivity is discussed in Section 5.5. The background normalizations in the fit were kept fixed in order to isolate the effect of the likelihood cut on the $t\bar{t}$ signal. Results of the sensitivity on the extracted fractions and the signal efficiencies as a function of the likelihood cut are shown in Table 5.4.

Channel		LH > -49	LH > -48	LH > -47	LH > -46
	σ_{F_0}	0.0168±0.0002	0.0167±0.0002	0.0174±0.0002	0.0193±0.0002
e+**jets**	σ_{F_L}	0.0299±0.0003	0.0301±0.0003	0.0299±0.0003	0.0350±0.0003
	σ_{F_R}	0.0293±0.0003	0.0285±0.0003	0.0288±0.0003	0.0324±0.0003
	σ_{F_0}	0.0159±0.0002	0.0161±0.0002	0.0170±0.0002	0.0193±0.0002
μ+**jets**	σ_{F_L}	0.0285±0.0003	0.0281±0.0003	0.0297±0.0003	0.0353±0.0004
	σ_{F_R}	0.0273±0.0003	0.0268±0.0003	0.0288±0.0003	0.0337±0.0004
LH Cut Efficiency		0.418	0.375	0.308	0.212

Table 5.4: Top: scan of log likelihood cuts designed to find value that yields optimal statistical sensitivity of hadronic helicity fraction extraction. A log likelihood cut of > -48 was found to have the best sensitivity. Bottom: $t\bar{t}$ efficiency for each likelihood cut in the scan.

A log likelihood cut of > -48 is found to optimize the statistical sensitivity in the hadronic channel. An identical study on the leptonic angle showed no significant gain (or loss) in sensitivity for any cut on likelihood, so the hadronically optimal cut of log likelihood > -48 was applied to all events for both angles to simplify combinations between the leptonic and hadronic channels. Plots for both lepton channels and b tag regions showing data/prediction comparisons after event reconstruction and the log likelihood cut are shown in Figures 5.1-5.4. The log likelihood plots are shown before the likelihood cut is applied.

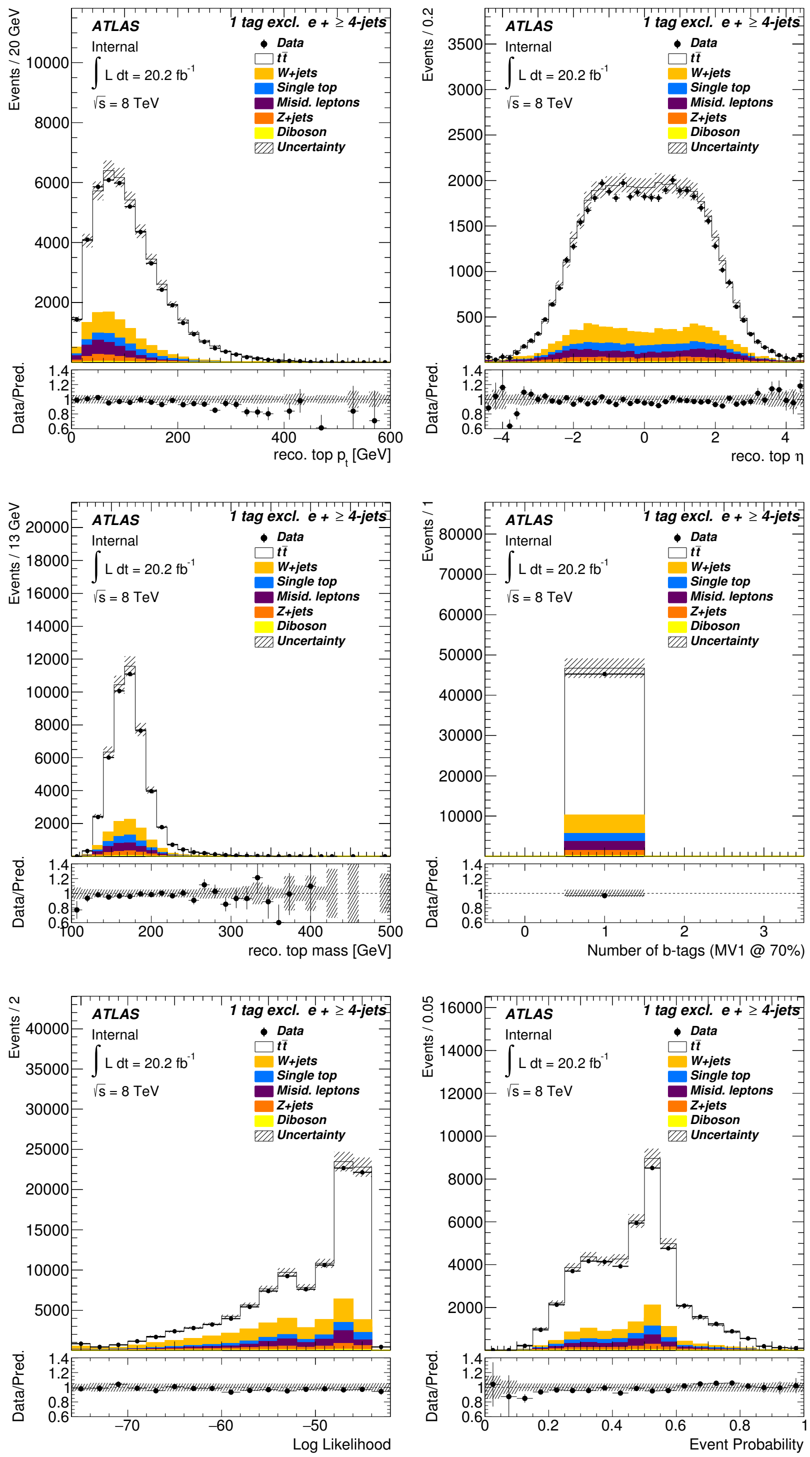

Figure 5.6: Control distributions in the 1 exclusive b tag, electron channel for selected top kinematics, the log likelihood, and the event probability distributions of the leading permutation (ranked by event probability). All plots except for the log likelihood are shown after the cut LH > -48. The shaded bands represent the Monte Carlo statistical uncertainties.

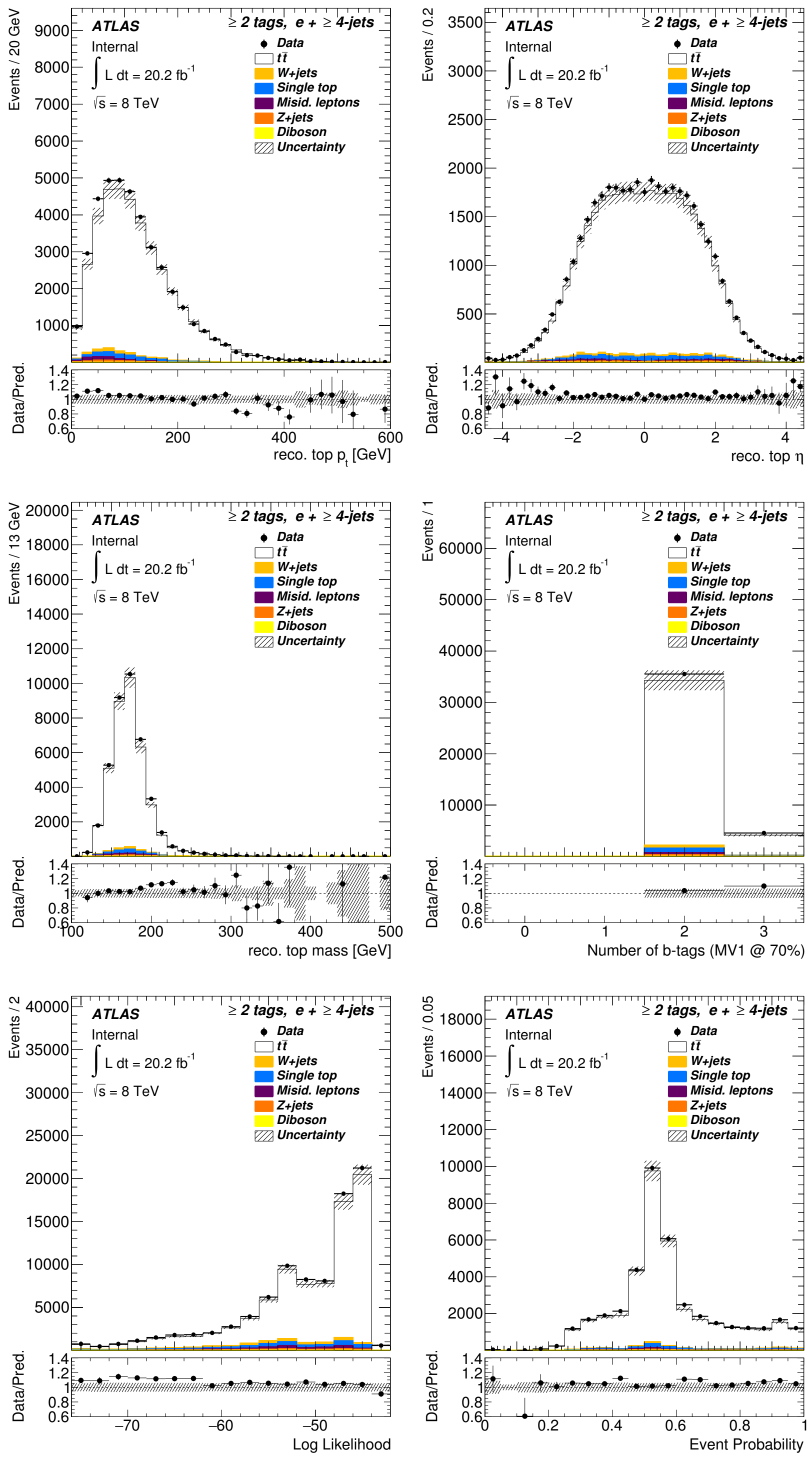

Figure 5.7: Control distributions in the 2 inclusive b tag, electron channel for selected top kinematics, the log likelihood, and the event probability distributions of the leading permutation (ranked by event probability). All plots except for the log likelihood are shown after the cut LH > -48. The shaded bands represent the Monte Carlo statistical uncertainties.

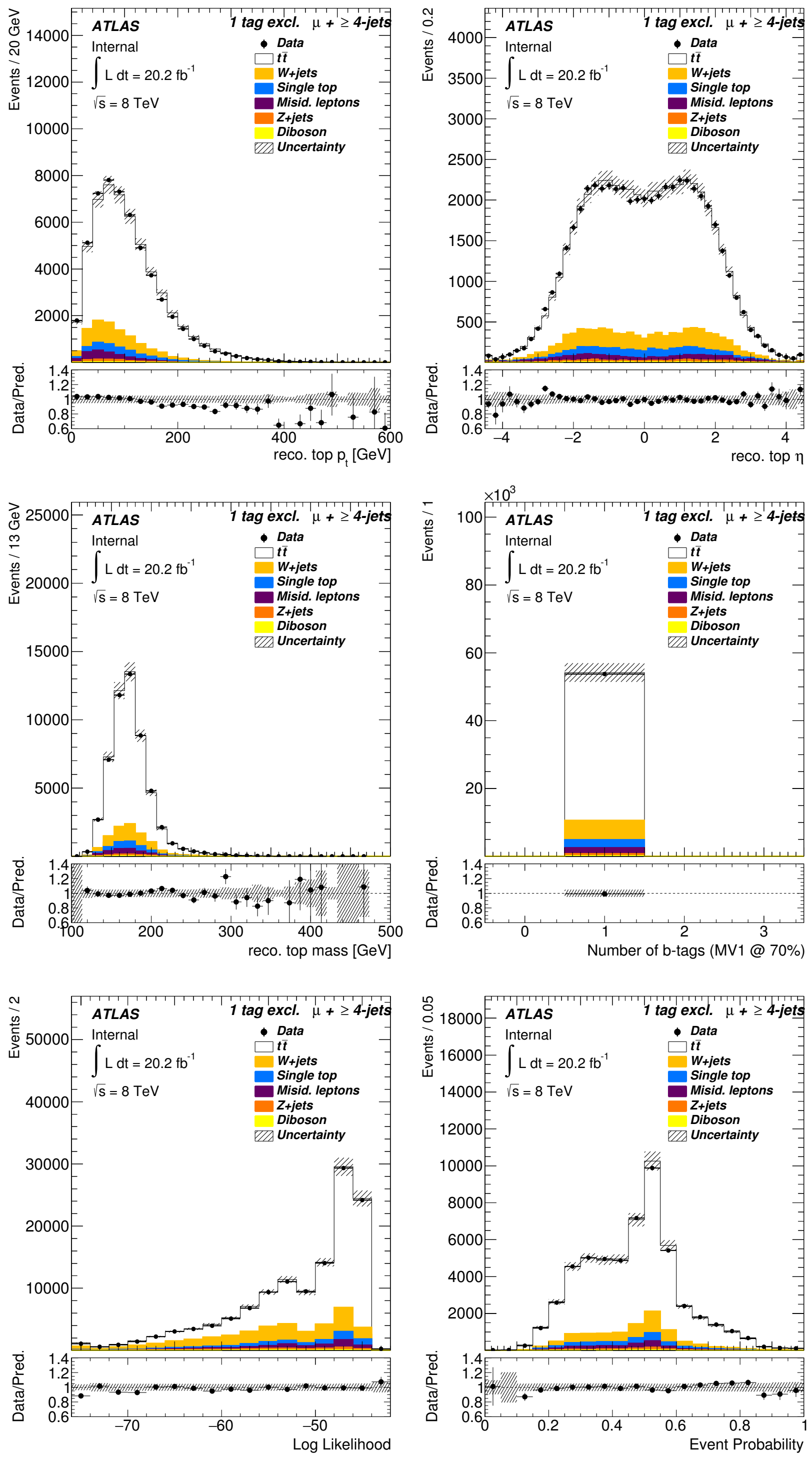

Figure 5.8: Control distributions in the 1 exclusive b tag, muon channel for selected top kinematics, the log likelihood, and the event probability distributions of the leading permutation (ranked by event probability). All plots except for the log likelihood are shown after the cut LH > -48. The shaded bands represent the Monte Carlo statistical uncertainties.

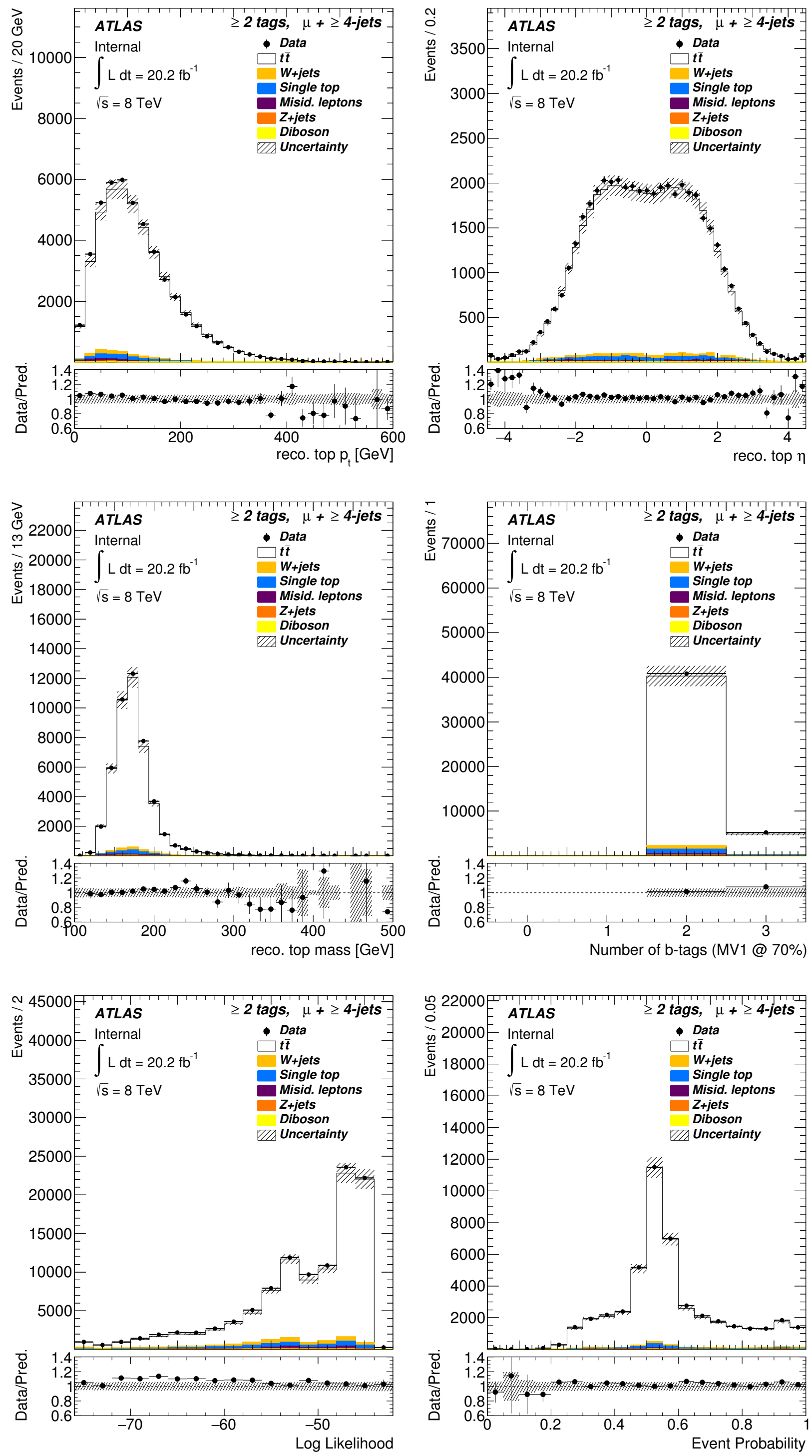

Figure 5.9: Control distributions in the 2 inclusive b tag, muon channel for selected top kinematics, the log likelihood, and the event probability distributions of the leading permutation (ranked by event probability). All plots except for the log likelihood are shown after the cut LH > -48. The shaded bands represent the Monte Carlo statistical uncertainties.

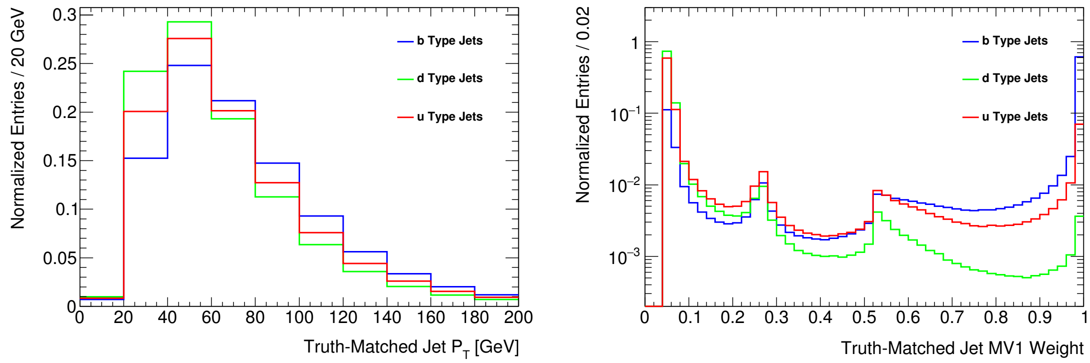

Figure 5.10: Templates of reconstructed p_{T} and MV1 weight for truth-matched u-type, d-type, and b jets. These templates are used as inputs to the u/d separation configuration of KLFitter.

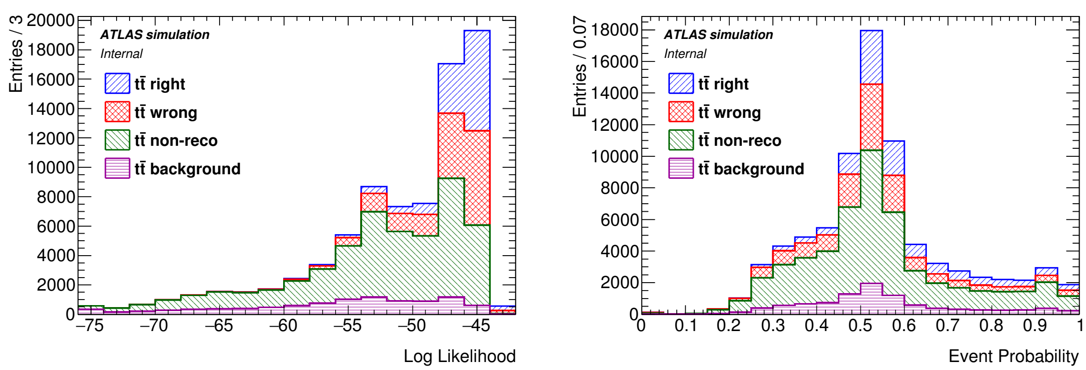

Figure 5.11: Categorized $t\bar{t}$ distributions for log likelihood and event probability of leading KLFitter permutation. Total yield is normalized to $t\bar{t}$ yield from 20.3 fb^{-1}.

5.5 Template Fitting

In this analysis, the W boson helicity fractions are measured by fitting the $t\bar{t}$ and background distributions to the data using a binned likelihood template fit. A brief discussion of the re-weighting method for producing pure helicity templates is provided followed by a discussion of the mechanics of the likelihood fit. The section concludes with a discussion of the correlations between the leptonic and hadronic measurements, the evaluation of statistical and systematic uncertainty, and closure tests on the fitting method.

5.5.1 Template Re-weighting

Since there is no next-to-leading order (NLO) simulation $t\bar{t}$ sample capable of generating pure W boson helicity states, the three required pure helicity templates are produced by re-weighting the Powheg $t\bar{t}$ sample at truth level. The pre-selection truth $\cos\theta^*$ observed in the Monte Carlo is fit to obtain the input helicity fractions, F_i^{Powheg}. Two sets of weights (one for the hadronic W and one for the leptonic W) are generated per event using the truth $\cos\theta^*$ values from $t\bar{t}$ events after event reconstruction. Weights are calculated separately for the leptonically and hadronically decaying W's as they have independent truth values of $\cos\theta^*$. The weights, $W_i(\cos\theta^*)$ are produced using Eq. 5.14.

$$W_i(\cos\theta^*) = \frac{w_i(\cos\theta^*)}{w_0(\cos\theta^*) + w_L(\cos\theta^*) + w_R(\cos\theta^*)} \tag{5.14}$$

where $i = 0$, L, R and the components $w_i(\cos\theta^*)$ are taken from Eq. 5.1 and the have functional form

$$w_0(\cos\theta^*) = \frac{3}{4}(1 - cos^2\theta^*)F_0^{\text{Powheg}} \tag{5.15}$$

$$w_L(\cos\theta^*) = \frac{3}{8}(1 - cos\theta^*)^2 F_L^{\text{Powheg}} \tag{5.16}$$

$$w_R(\cos\theta^*) = \frac{3}{8}(1 + cos\theta^*)^2 F_R^{\text{Powheg}} \tag{5.17}$$

Figures 5.12 and 5.13 display the re-weighted signal templates for e+jets and μ+jets channels in both b tag regions. The background templates for the leptonic and hadronic channels in both b tag regions are shown in Figures 5.14 and 5.15 and show the shapes for W +light jets, W +c jets, W +bb/cc jets, misidentified leptons, and the template for the remaining background contributions, namely single-top, Z+jets and diboson processes. The large fluctuations and spikes in W +light and W +c jets background templates in the two inclusive b tag region are due to leak of MC statistics. No significant difference in the fit results was observed when using smoothed background templates in place of unsmoothed templates.

5.5.2 Likelihood Fit

A binned likelihood fit is performed using the signal and background templates mentioned above. The fit procedure is based on the ROOT MINUIT package [108], [109]. The normalizations of the backgrounds and the normalizations of each pure $t\bar{t}$ helicity template are free parameters in the fit. The number of expected events in the fit corresponds to the sum of all template normalizations calculated and is calculated as:

$$n_{\text{exp, templ.}} = n_{\text{0, templ.}} + n_{\text{L, templ.}} + n_{\text{R, templ.}} + n_{\text{W+light}} + n_{\text{W+}c} + n_{\text{W+}bb/cc} + n_{\text{QCD}} + n_{\text{Rem.Bkg.}}, \tag{5.18}$$

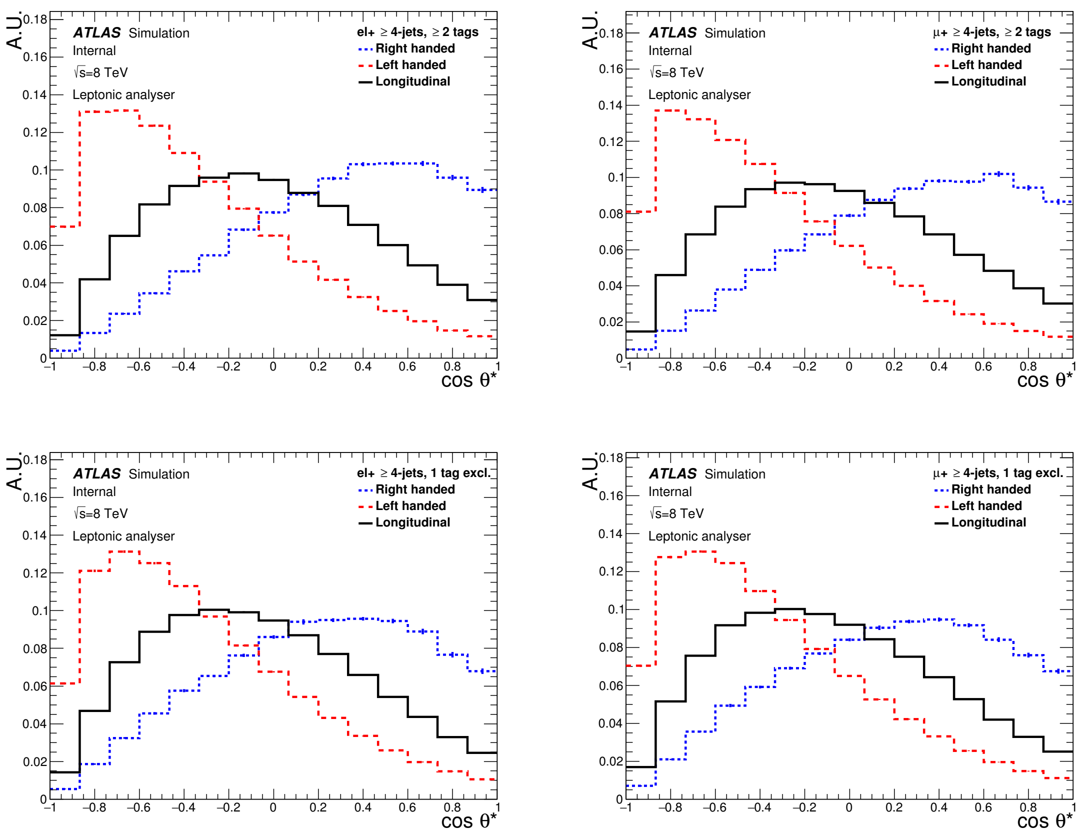

Figure 5.12: Reconstructed signal templates for e+jets channel (left) and μ+jets channel (right) in the two inclusive b tag region (top) and one exclusive b tag region (bottom) for the leptonic angle.

to be compared in each bin to the data distribution from the likelihood fit:

$$\mathscr{L} = \prod_{i=1}^{N_{\text{bins}}} \text{Poisson}(n_{\text{data},i}, n_{\text{exp},i}) \prod_{j=1}^{N_{\text{bkg}}} \frac{1}{\sqrt{2\pi}\sigma_{\text{bkg.j}}} e^{\frac{-(n_{\text{bkg.j}} - \hat{n}_{\text{bkg.j}})^2}{2\sigma^2_{\text{bkg.j}}}}, \qquad (5.19)$$

where the background normalization uncertainties are constrained by Gaussian priors, and the $\sigma_{\text{bkg.j}}$ are the background normalization uncertainties for a given background. All free parameters in Eq. 5.18, except for n_{QCD}, are common across all lepton/b tagged regions (e.g. the same $n_{\text{W+light}}$ parameter is common across all signal regions). The fake lepton normalization, n_{QCD}, is floated independently for electrons and muons and in different b tag regions. For the W +jets components, the normalization uncertainties are taken from the data-driven calibration factors [74]: 5% for W +light jets, 25% for W +c jets and 7%

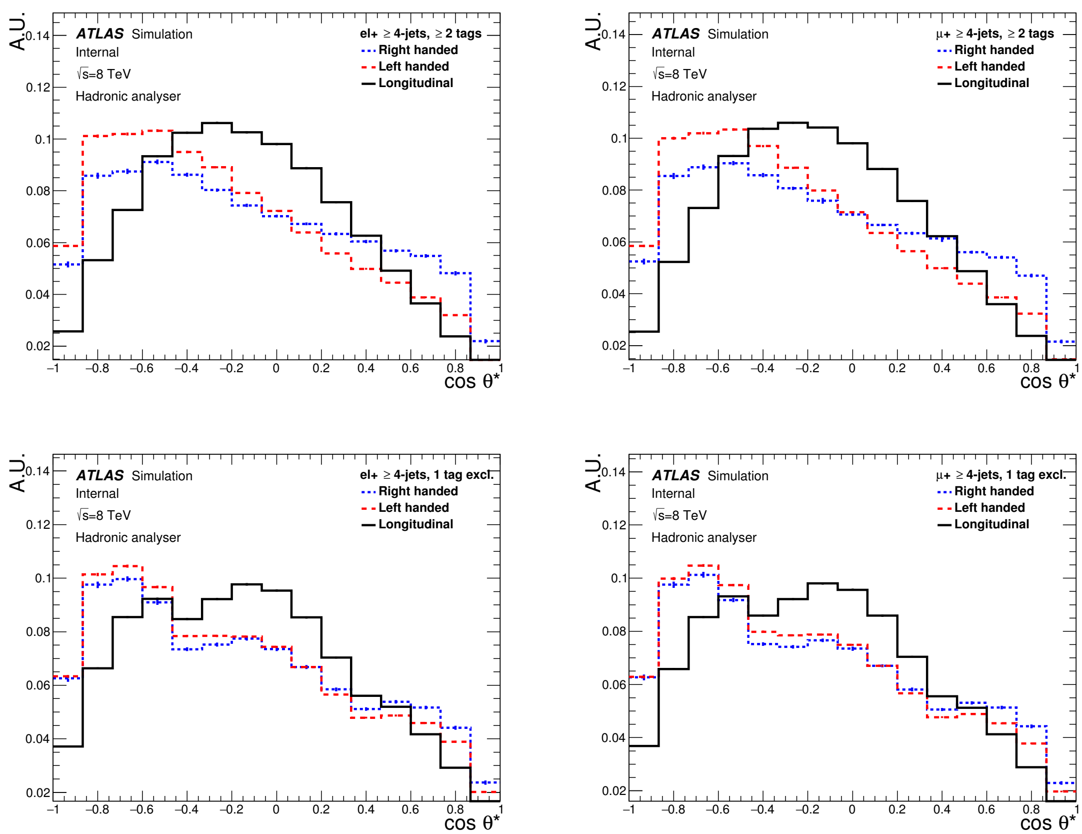

Figure 5.13: Reconstructed signal templates for e+jets channel (left) and μ+jets channel (right) in the two inclusive b tag region (top) and one exclusive b tag region (bottom) for the hadronic angle.

for W +cc/bb jets. A relative uncertainty of 30% is estimated for the matrix method QCD calculation [110] and is used for the fake lepton contribution. An uncertainty of 16% (17%) is considered for the remaining background sources in the two inclusive b tag region (one exclusive + two inclusive b tag region) by adding the uncertainties on the theoretical cross sections of the single top quark, diboson and Z+jets components in quadrature with extra uncertainties accounting for additional jet reconstruction. For single top production, an uncertainty of 17% is assumed, which takes into account the variation from the initial and final state radiation in t-channel samples and accounts for the single top +jets requirement in the 4 jets signal region. An overall normalization uncertainty of 48% is applied to Z+jets and diboson contributions which takes into account 5% uncertainty on the theoretical (N)NLO cross section and uncertainties to account for the extrapolation to high jet multiplicity (24% per jet). A summary of all the free parameters in the fit and their uncertainties is

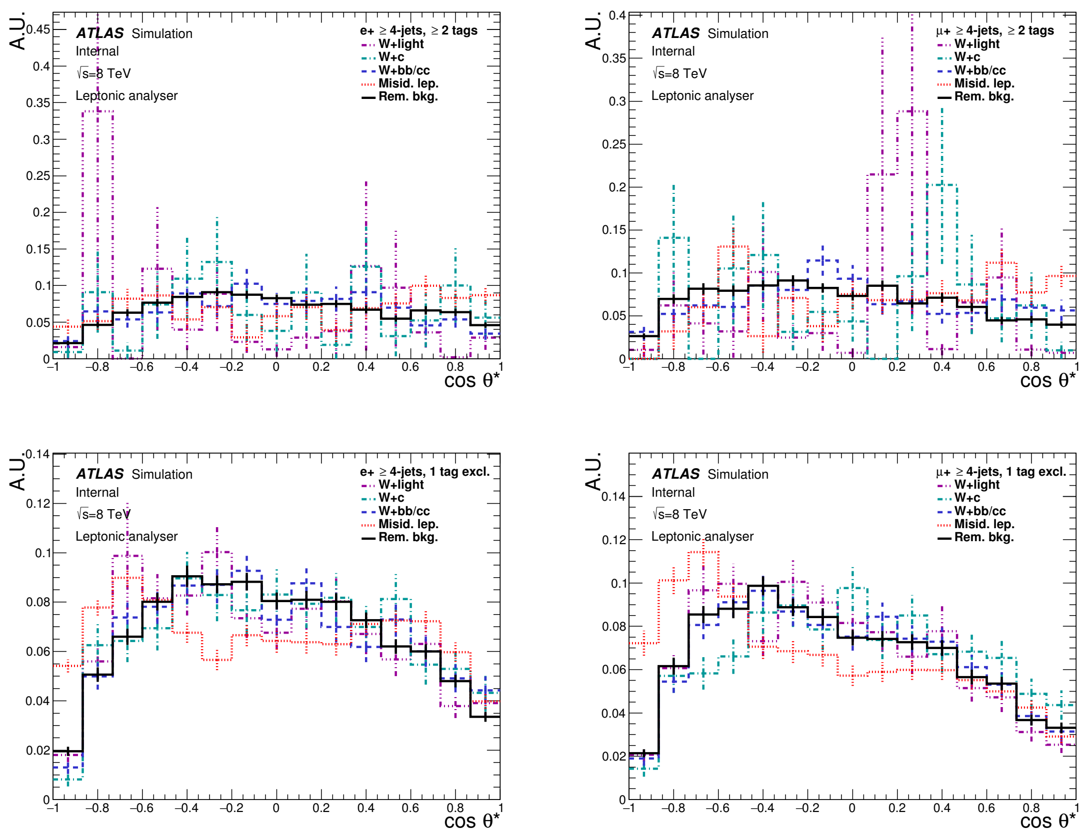

Figure 5.14: Background templates for e+jets channel (left) and μ+jets channel (right) in the two inclusive b tag region (top) and one exclusive b tag region (bottom) for the leptonic angle.

given in Table 5.5. For most backgrounds, the normalizations are taken from simulation. Exceptionally, the normalization for misidentified leptons and W+jets events is taken from a data-driven method (see Section 5.3 for details). These background normalizations and uncertainties are shown in Table 5.1.

The normalization for each helicity template is allowed to float unconstrained in the fit. Because the analysis is not equally sensitive to all helicity states, extraction of the production-level helicity fractions requires knowledge of the reconstruction efficiency per helicity state. These efficiencies, $\epsilon_i^{\mathrm{sel}}$, are calculated using the nominal $t\bar{t}$ sample and are shown in Table 5.8. Given that the total $t\bar{t}$ cross-section cancels in the calculation of the helicity fractions, the quantities N_i are defined to translate the post-fit normalizations, $n_{\mathrm{i,\ templ.}}$, into experimentally-independent quantities using these efficiencies. The relation-

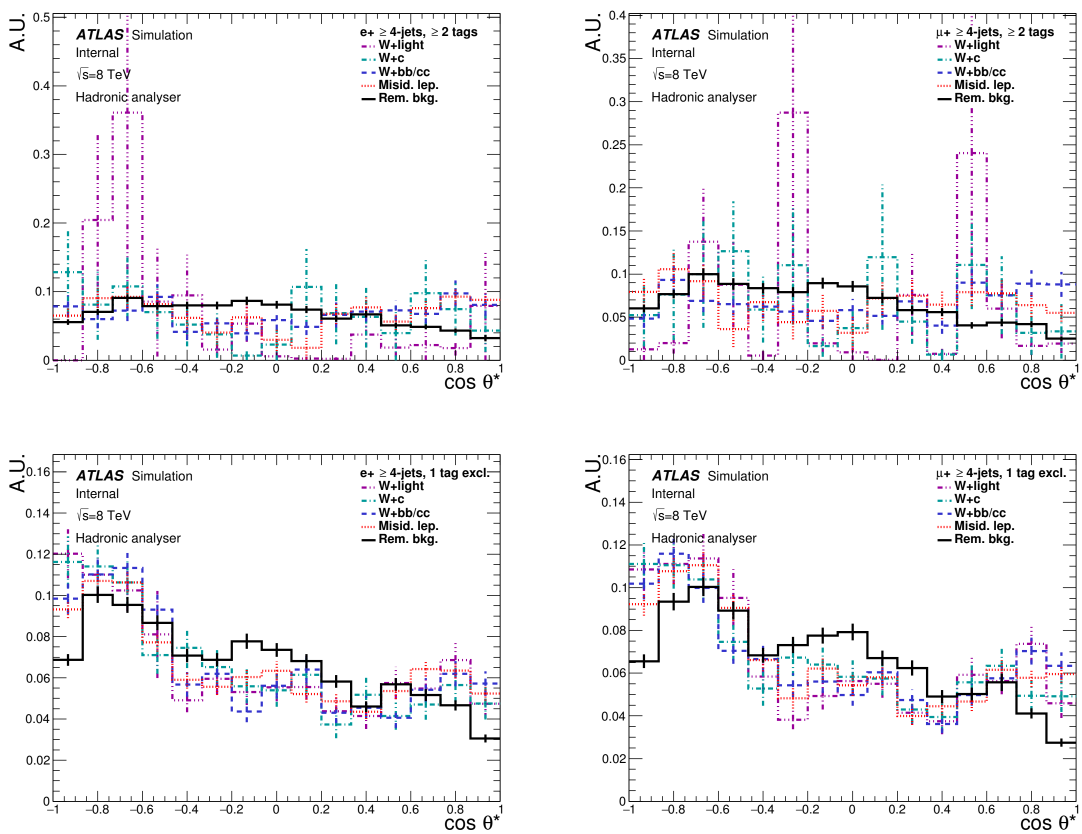

Figure 5.15: Background templates for e+jets channel (left) and μ+jets channel (right) in the two inclusive b tag region (top) and one exclusive b tag region (bottom) for the hadronic angle.

Fit Parameter	Relative Width of Gaussian Prior
n_0	-
n_L	-
n_R	-
$n_{W\ +\text{light}}$	0.05
$n_{W\ +\text{c}}$	0.25
$n_{W\ +\text{bb/cc}}$	0.07
n_{QCD}	0.30
$n_{\text{Rem. Bkg.}}$	0.16(0.17) in $\geqslant 2$ b tags ($1\ b + \geqslant 2\ b$ tags)

Table 5.5: List of all free parameters in the bin-by-bin likelihood fit as well as the relative widths (width/normalization) of the Gaussian priors assumed in the fit with floating backgrounds.

ship is given by

$$n_{\text{i, templ.}} = \epsilon_i^{\text{sel}} \cdot N_i \quad \text{for i= 0, L, R,} \tag{5.20}$$

where, again, the $n_{\text{i, templ.}}$ are the parameters in the likelihood fit. Using N_i allows the final helicity fractions to be expressed the simple ratio

$$F_{\text{i}} = \frac{N_i}{N_0 + N_L + N_R} \quad \text{for i= 0, L, R.} \tag{5.21}$$

5.5.3 Combining Fit Regions

The combination of one exclusive and two inclusive b tag regions as well as the combination of e+jets and μ+jets channels is studied. The channels are combined via a common likelihood fit; the signal templates for each of the respective helicity states are combined in an extended distribution with two/four/eight times the number of bins in the two/four/eight channel combination, while each background contribution is fit as described in the previous section. The selection efficiencies for the combined templates are adjusted accordingly. The summary of the pre-fit and post-fit yields in the combined electron + muon channel in two inclusive b tag region for leptonic analyzer and in one exclusive + two inclusive b region for the hadronic analyzer are shown in Tables 5.6 and 5.7 respectively.

5.5.4 Correlations Between Leptonic and Hadronic Measurements

Since there are two simultaneous measurements being performed per event (the angles from leptonically and hadronically decaying W bosons), the correlation between the two angles needs to be quantified. Even though they are, in principle, uncorrelated as the decays themselves are independent, a non-zero correlation could be introduced through the reconstruction. In the case of non-negligible correlation, it would be incorrect to evaluate

Parameter	Norm. unc.	Pre-fit	Post-fit	Δ%
$t\bar{t}$	-		2.87e+06 ± 44700	
W+light	5%	68	68 ± 3	0.02
W+c	25%	105	105 ± 26	0.3
W+bb/cc	7%	1318	1317 ± 92	-0.08
QCD 2incl. (el)	30%	447	575 ± 117	28.6
QCD 2incl. (mu)	30%	330	285 ± 93	-13.6
Rem. bkg.	16%	2633	2629 ± 414	-0.2

Table 5.6: Pre-fit and post-fit yields comparison in the combined electron + muon channel in two inclusive b tag region for the leptonic analyzer.

Parameter	Norm. unc.	Pre-fit	Post-fit	Δ%
$t\bar{t}$	-		2.90e+06 ± 94400	
W+light	5%	1430	1424 ± 71	-0.4
W+c	25%	2756	2070 ± 577	-24.9
W+bb/cc	7%	7565	7298 ± 495	-3.5
QCD 1excl. (el)	30%	2272	1431 ± 348	-37
QCD 1excl. (mu)	30%	447	620 ± 111	38.7
QCD 2incl. (el)	30%	1746	1379 ± 340	-21
QCD 2incl. (mu)	30%	323	283 ± 92	-12.3
Rem. bkg.	17%	9191	6019 ± 1290	-34.5

Table 5.7: Pre-fit and post-fit yields comparison in the combined electron + muon channel in one exclusive + two inclusive b tag region for the hadronic analyzer.

the uncertainties in the different channels independently, and the correlation would need to be correctly accounted for. In the case of negligible correlation, the two channels can be treated and evaluated fully independently.

To estimate the correlation, two-dimensional plots (one angle per axis) are produced and the correlation factor (=-1 for perfect anti-correlation, = +1 for perfect correlation, = 0 for 100% uncorrelated) calculated. The plots are shown in Figure 5.16. The correlation factor is evaluated for all events with at least two b tags passing the nominal selection as well as for the subset events with log(LH)> -48 (discussed in Section 5.4.5 for optimizing hadronic sensitivity).

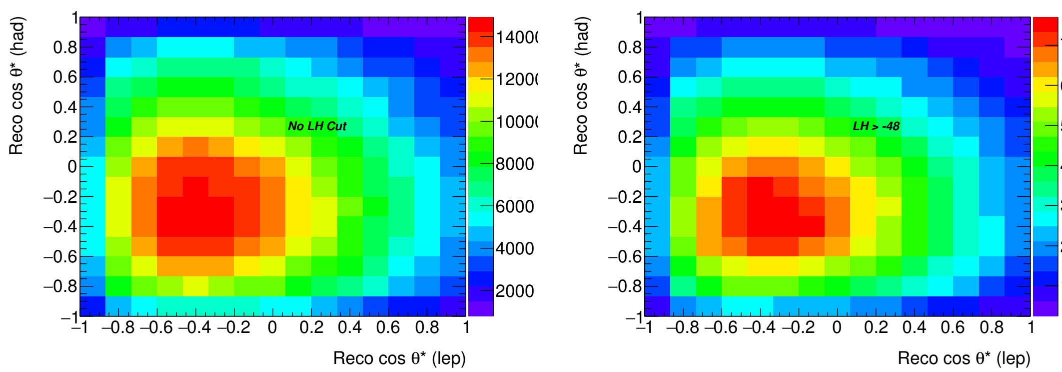

Figure 5.16: Two-dimensional distributions of the reconstructed leptonic and hadronic cos θ^* in all events with two or more b tags passing the nominal selection (left) and passing the nominal selection plus the cut LH > -48 to optimize the sensitivity of the hadronic analyzer.

The correlation factor is calculated to be -0.0038 for the nominal selection and -0.0029 when imposing the LH cut. The correlation is considered to be negligible in both cases, and the measurements are considered to be independent for the remainder of this analysis.

5.5.5 Evaluation of Systematic and Expected Statistical Uncertainties

Ensemble tests are performed for the estimation of systematic and expected statistical uncertainties. Pseudo-data distributions are produced using MC simulation and scaled to the actual data statistics. Ensembles (pseudo-experiments) are obtained by fluctuating each bin of the pseudo-data distribution according to Poisson statistics. For the template fit, 5,000 pseudo-experiments are generated. The mean values of N_0 , N_L and N_R are used to calculate the specific W-helicity fractions for each pseudo-data distribution. The differences between the fractions obtained from the nominal distribution and the fractions obtained from each systematic variation are considered. For systematics with up and down variations, the calculated systematic shifts are added in quadrature. For one-sided sources of systematic uncertainty (e.g. jet energy resolution, signal modeling systematics), the single variation is symmetrized and taken as both the up and down variations. All contributions summed in quadrature.

The expected statistical uncertainties are obtained from fits to the pseudo-data distributions, where MINUIT provides the fitted number of events and the corresponding statistical uncertainties. Since the helicity fractions are obtained from the fitted number of events, the error propagation is considered accordingly. Table 5.9 summarizes the statistical uncertainty expectation obtained in each channel from ensemble test fits. The normalization of the background contributions were kept fixed during these tests in order to estimate the absolute statistical uncertainty. In each W boson decay (leptonic and hadronic), the e+jets and μ+jets channels are combined. The combined sensitivities are high as expected from the increase in statistics. The eight-channel combination including both leptonic and hadronic sides, provides the lowest expected statistical uncertainty.

As seen in table 5.9, the expected statistical sensitivities are worse for the helicity fractions fit from the hadronic side than those fits from the leptonic one. This is a reflection of the imperfect identification of the up and down type jets from the decay of the hadronic W boson which results in a lower discrimination between the pure, re-weighted templates. The sensitivity of the hadronic extraction is improved by requiring the log likelihood of the leading permutation be greater than -48. This optimization is discussed in Section 5.4.5.

Five thousand pseudo-experiments are performed to evaluate the sensitivity of the leptonic channel both with and without the likelihood cut derived from the hadronic optimization. The sensitivity of the eight-channel combination measurement is also evaluated when the likelihood cut was applied to both channels and when it was applied to the hadronic channel alone. The results are summarized in same table and show negligible difference. To simplify the combination and of the leptonic and hadronic measurements, the same likelihood cut is imposed for both the leptonic and hadronic measurements. Using identical phase spaces has the additional benefit of allowing the background templates to be treated as correlated quantities in the leptonic+hadronic combination fit.

Table 5.10 compares the measured helicity fractions obtained from fit to data when the background normalizations are fixed to their Monte Carlo predictions and when they are allowed to float within their theoretical uncertainties according their associated Gaussian priors. Since the floating background normalization treatment takes the background normalization uncertainties into account, the systematic uncertainties due to background normalization uncertainties are evaluated individually in the fixed background configuration. The up (down) variation of each background is obtained by increasing (decreasing) the

Selection eff.	e+jets (lep)	μ+jets (lep)	e+jets (had)	μ+jets (had)
1 Exclusive b tag				
ϵ_0	0.014	0.017	0.014	0.016
ϵ_L	0.010	0.013	0.012	0.014
ϵ_R	0.015	0.017	0.012	0.014
2 Inclusive b tags				
ϵ_0	0.014	0.017	0.013	0.016
ϵ_L	0.010	0.012	0.012	0.014
ϵ_R	0.016	0.018	0.012	0.014

Table 5.8: Selection efficiencies in the 1 exclusive and 2 inclusive b tag regions for both the leptonic and hadronic templates in the e+jets and μ+jets channel.

Cut		2incl. b tag	1excl+2incl b tag
Leptonic side			
no LH cut	σ_{F_0}	0.010 ± 1.0%	0.009 ± 1.0%
	σ_{F_L}	0.006 ± 1.0%	0.005 ± 1.0%
	σ_{F_R}	0.005 ± 1.0%	0.004 ± 1.0%
LH >-48	σ_{F_0}	0.012 ± 1.3%	0.010 ± 1.1%
	σ_{F_L}	0.008 ± 1.3%	0.006 ± 1.0%
	σ_{F_R}	0.006 ± 1.3%	0.004 ± 1.1%
Hadronic side			
LH >-48	σ_{F_0}	0.012 ± 1.0%	0.010 ± 1.0%
	σ_{F_L}	0.022 ± 1.1%	0.021 ± 1.0%
	σ_{F_R}	0.022 ± 1.0%	0.021 ± 1.1%
Leptonic + hadronic combination			
LH >-48 in hadronic side	σ_{F_0}	0.008 ± 1.0%	0.007 ± 1.1%
	σ_{F_L}	0.005 ± 1.0%	0.004 ± 1.1%
	σ_{F_R}	0.004 ± 1.0%	0.003 ± 1.0%
LH >-48 in both sides	σ_{F_0}	0.008 ± 1.0%	0.007 ± 1.0%
	σ_{F_L}	0.006 ± 1.0%	0.005 ± 1.0%
	σ_{F_R}	0.004 ± 1.0%	0.004 ± 1.0%

Table 5.9: Absolute statistical uncertainty expectations of the helicity fractions fitted using the leptonic side, hadronic side and combined in 2 inclusive b tag and the combined 1excl. + 2incl. b tag. The requirement of the leading log likelihood to be > -48 is applied to the hadronic analyzer and also studied for the leptonic analyzer. The combined leptonic + hadronic sides is also presented for both cut options. The background normalization uncertainties kept fixed in the fit. The relative errors presenting the error in obtaining the Gaussian width of each helicity fraction distribution.

Background norm. unc.		2incl. b tag	1excl+2incl b tag
		Leptonic side	
Fixed X ± Y(stat.)± Z(bkg. norm.)	F_0	0.707 ± 0.012 ± 0.004	0.696 ± 0.010 ± 0.009
	F_L	0.300 ± 0.008 ± 0.001	0.305 ± 0.006 ± 0.005
	F_R	-0.007 ± 0.006 ± 0.003	-0.001 ± 0.005 ± 0.005
Floating X ± Y(stat.+bkg. norm.)	F_0	0.709 ± 0.012	0.686 ± 0.010
	F_L	0.299 ± 0.008	0.308 ± 0.006
	F_R	-0.008 ± 0.006	0.006 ± 0.005
		Hadronic side	
Fixed	F_0	0.670 ± 0.012 ± 0.006	0.681 ± 0.010 ± 0.014
	F_L	0.297 ± 0.022 ± 0.006	0.301 ± 0.021 ± 0.013
	F_R	0.032 ± 0.022 ± 0.012	0.018 ± 0.020 ± 0.027
Floating	F_0	0.673 ± 0.013	0.659 ± 0.010
	F_L	0.299 ± 0.023	0.281 ± 0.021
	F_R	0.028 ± 0.024	0.061 ± 0.022
		Leptonic + hadronic combination	
Fixed	F_0	0.689 ± 0.008 ± 0.005	0.688 ± 0.007 ± 0.012
	F_L	0.310 ± 0.006 ± 0.002	0.309 ± 0.005 ± 0.006
	F_R	0.001 ± 0.004 ± 0.003	0.003 ± 0.004 ± 0.006
Floating	F_0	0.694 ± 0.008	0.674 ± 0.007
	F_L	0.308 ± 0.006	0.315 ± 0.005
	F_R	-0.002 ± 0.004	0.011 ± 0.004

Table 5.10: Measured helicity fractions obtained from fit to data using the leptonic side, hadronic side and combined in 2 inclusive b tag and the combined 1excl. + 2incl. b tag. The requirement of the leading log likelihood to be > -48 is applied to both leptonic and hadronic analyzers. The fit results are compared when the background normalizations are fixed to their Monte Carlo predictions and when they are allowed to float within their theoretical uncertainties according to Gaussian prior.

corresponding normalization by the upper (lower) normalization uncertainty while keeping fixing the other backgrounds normalizations to their nominal values. The total background normalization uncertainty is the quadrature sum of all components after symmetrization. The helicity fractions obtained using the fixed background configuration are consistent with the results obtained by using the floating background normalization configuration.

5.5.6 Method Validation

The template fit method is validated by producing pseudo-data using input helicity fractions varied over reasonable value ranges and testing whether the extracted fractions measure the input fractions. The longitudinal W-helicity fraction is varied between 0.4 and 1.0 by steps of 0.1, while the left-handed and right-handed fractions are both iterated in steps of 0.05

while enforcing the condition that the sum of the three fractions equal unity. The templates are fitted to the ensembles generated for each calibration point. Calibration curves are created using 5000 ensembles per calibration point. The linearity test results for the fully combined region (1 exclusive + 2 inclusive b tag, electron + muon, leptonic + hadronic measurements) are shown in Figure 5.17. The measured slopes of one and offsets of zero are indicative of an unbiased extraction.

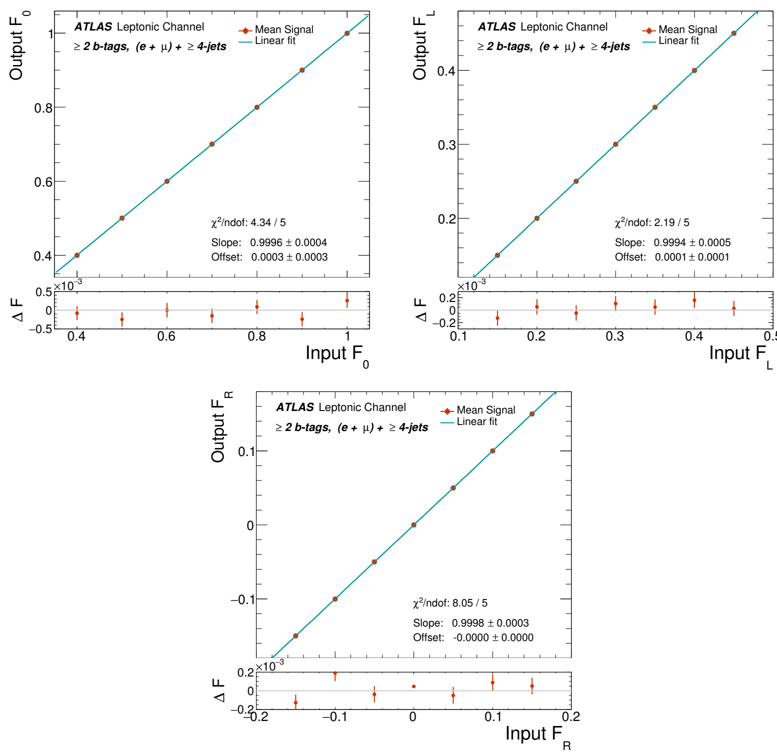

Figure 5.17: Linearity checks for F_0, F_L, and F_R in the electron+muon in two inclusive b tag region for the leptonic analyzer. 5000 sets of pseudo-data were fit to perform the test. Good closure is seen for all helicity fractions, and no bias is observed.

5.6 Systematic Uncertainties

Several sources of systematic uncertainties are considered that could affect the signal and background normalizations and/or the shapes of their $\cos\theta^*$ distributions. Individual sources of systematic uncertainty are considered uncorrelated. Correlations of a single systematic uncertainty are maintained across processes and channels. Table 5.11 presents a summary of the systematic uncertainties considered in this analysis and indicates whether each affects either only normalizations or both shapes and normalizations. When the difference between the nominal $\cos\theta^*$ distribution and a given systematic variation is smaller than the statistical uncertainty on the Monte Carlo yield of the nominal sample, that systematic variation is removed from consideration when calculating the total systematic error. A variation is kept if a) the difference between the total yield of the varied $\cos\theta^*$ distribution and the total nominal yield is larger than the total nominal Monte Carlo statistical uncertainty and/or b) if the difference in yield between the nominal sample and a variation is larger than the nominal MC uncertainty in two or more individual bins. The following sections describe each of the systematic uncertainties considered in the analysis. Results are shown in Tables 5.12, 5.13, and 5.14.

5.6.1 Luminosity

The measured luminosity delivered to the ATLAS experiment during pp collisions at $\sqrt{s} = 8$ TeV has an estimated uncertainty of 1.9% [111]. The overall luminosity uncertainty affects the normalizations of all backgrounds and the $t\bar{t}$ signal. Any impact of the luminosity uncertainty is fully correlated between the three pure helicity fraction normalizations and therefore cancels identically. The effect on all three helicity fractions due to the luminosity uncertainty is found to be $< 10^{-6}$.

5.6.2 Physics Objects

Lepton Reconstruction, Identification and Trigger

The reconstruction and identification efficiency of electrons and muons, as well as the efficiency of the triggers used to record the events, differ between data and simulation. Scale factors are derived using tag-and-probe techniques on $Z \to \ell^+\ell^-$ ($\ell = e, \mu$) data and simulated samples to correct the simulation for these discrepancies.

Lepton Momentum Scale and Resolution

The accuracy of lepton momentum scale and resolution in simulation is checked using reconstructed distributions of the $Z \to \ell^+\ell^-$ and $J/\psi \to \ell^+\ell^-$ masses. In the case of electrons, E/p studies using $W \to e\nu$ events are also used. Small discrepancies are observed between data and simulation, and corrections for the lepton energy scale and resolution in the latter are implemented using the tools provided by the combined performance groups. In the case of muons, momentum scale and resolution corrections are only applied to the simulation. Uncertainties on both the momentum scale and resolutions in the muon spectrometer and the tracking systems are considered and varied separately.

Systematic uncertainty	Type	Components
Luminosity	N	1
Physics Objects		
Electron	SN	5
Muon	SN	6
Jet energy scale	SN	26
Jet vertex fraction	SN	1
Jet energy resolution	SN	11
Jet reconstruction efficiency	SN	1
b tagging efficiency	SN	6
c tagging efficiency	SN	4
Light jet tagging efficiency	SN	12
Background Model		
W+light/c/bb/cc calibration	N	3
W+jets shape	S	1
Multi-jet normalization	N	1
Z+jets normalization	N	1
Single top cross section	N	1
Diboson+jets normalization	N	1
Signal Model		
$t\bar{t}$ Radiation	SN	2
$t\bar{t}$ MC Generator	SN	1
$t\bar{t}$ Showering & Hadronization	SN	1
$t\bar{t}$ PDF	SN	3
Top mass	SN	1
Template Statistics	SN	1

Table 5.11: List of systematic uncertainties considered. "N" represents uncertainties only affecting the normalization for all processes and channels, whereas "S" denotes systematic uncertainties that are considered as shape-only in all processes and channels. "SN" means that the uncertainty is affecting both shape and normalization. Some of the systematic uncertainties are split into several different components for a more accurate treatment (number indicated under the column labeled as "Components").

Jet Reconstruction Efficiency

The jet reconstruction efficiency is overestimated in MC simulations. This effect is taken into account by the evaluation of an additional systematic uncertainty. Reconstructed jets are dropped randomly to match the efficiency in data. Online jets with $p_{\mathrm{T}} < 30$ GeV are affected, of which 0.2 % are dropped. The analysis is then repeated with the reduced set of jets, and the difference to the nominal selection is quoted as the uncertainty.

Jet Vertex Fraction Efficiency

The per-jet efficiency to satisfy the jet vertex fraction requirement is measured in $Z(\to \ell^+\ell^-)$+1-jet events in data and simulation, separately selecting events enriched in hard-scatter jets and events enriched in jets from other proton interactions in the same bunch crossing (pileup). The corresponding uncertainty is evaluated in the analysis by changing the nominal JVF cut value by 0.1 up and down and repeating the analysis using the modified cut value.

Jet Energy Scale

The jet energy scale (JES) and its uncertainty are derived by combining information from test-beam data, LHC collision data, and simulation [50, 112–114]. The jet energy scale uncertainty is split into 26 uncorrelated sources which can have different jet p_{T} and η dependencies and are treated independently in this analysis. The `JetUncertainties` tool [115] allows computation of uncertainties corresponding to each of the eigenvectors.

Jet Energy Resolution

The jet energy resolution has been measured separately for data and simulation using two *in-situ* techniques [116]. The expected fractional p_{T} resolution for a given jet was measured using the `JERUncertaintyProvider` tool [117] as a function of its p_{T} and rapidity. For the majority of the jet p_{T} spectrum, the width of the balance between jets and well measured photons or leptonically reconstructed Z bosons is used to measure the detector resolution. Additionally, the balance between dijet events is used to extend these measurements to higher p_{T} and $\mid \eta \mid$. For very low p_{T} jets, there is a significant contribution to the jet energy resolution from pile-up particles and electronic noise.

The effect of the total jet energy resolution is parameterized as the sum of of terms relating electronic and pile-up noise, a term arising from the stochastic effect of the sampling nature of the calorimeters, and a constant p_{T} independent term. A correlation matrix as a function of p_{T} and $\mid \eta \mid$ is built to account for correlations between the measurements at different $\mid \eta \mid$. An eigenvector reduction is performed which results in a maximum of twelve additional nuisance parameters which describe all correlations between the p_{T} and $\mid \eta \mid$ regions covered by the $in-situ$ studies. In total, eleven orthogonal nuisance parameters are used to estimate the total systematic effect of the jet energy resolution.

Heavy- and Light-Flavor Tagging

Uncertainties due to the efficiencies of the heavy flavor identification of jets by the b tagging algorithm are also evaluated evaluated. These efficiencies are measured from data and depend on the jet flavor. Efficiencies for b and c quarks in the simulation are corrected by

p_{T}-dependent factors. The scale factors and their uncertainties are applied to each jet in the simulation depending on its flavor and p_{T}. In the case of light-flavor jets, the corrections also depend on jet η.

A total of 6 independent sources of uncertainty affecting the b tagging efficiency and 4 affecting the c tagging efficiency are considered. Each of these uncertainties correspond to a resulting eigenvector after diagonalizing the matrix containing the information of total uncertainty per p_{T} bin and the bin-to-bin correlations. Twelve uncertainties are considered for the efficiency of light jet tagging which depend on jet p_{T} and η regions. All b tagging systematic uncertainties are taken as uncorrelated between b jets, c jets, and light flavor jets. A per-jet weighting procedure [118] is applied to simulated events to propagate the calibration of b tagging and the related uncertainties.

5.6.3 Uncertainties on the Background Estimates

W+jets Modeling

As discussed in Sect. 5.3, the W+jets contribution is obtained from Monte Carlo and normalized using data-driven calibration factors which take into account the charge of the lepton and heavy flavor components of the associated jets. By independently varying each sub-component of the W+jets contribution (W+light, $W+c$, $W+bb/cc$) by its appropriate uncertainty (the corresponding calibration factor uncertainty) while the other two components are held fixed to their respective normalizations, the overall shape of the W+jets background is varied. The total shape uncertainty is then estimated from the envelope of the sub-component variations.

Z+jets Modeling

An overall normalization uncertainty of 48% is applied to Z+jets contribution. The overall uncertainty takes into account 5% uncertainty on the theoretical NLO cross section and 24% uncertainty on the extrapolation to higher jet multiplicities [119].

Multi-jet Modeling

Systematic uncertainties on the multi-jets background estimated via the matrix method in the single lepton channel are due to limited data statistics, particularly at high jet and b tag multiplicities, as well as from uncertainties on the fake rates, estimated in different control regions. A combined conservative uncertainty of 30% due to all these effects is assigned, which is taken as correlated across jet and b tag multiplicity bins, but uncorrelated between electron and muon channels.

A shape uncertainty is assigned to the fake multi-jets by varying the fake efficiencies up and down, and taking the new templates as the shape variations.

Electroweak backgrounds Modeling

Uncertainties of +5%/-4% and ±6.8% are assumed for the theoretical cross sections of the single top production [88, 89]. The former corresponds to the cross-section weighted average of the theoretical uncertainties on s-, t- and Wt-channel single top production (see Figure [**?**] for the relevant leading order Feynman diagrams), while the latter corresponds to the theoretical uncertainty on Wt-channel production. Uncertainty on the single top background shape is assessed by comparing Wt-channel MC samples generated using different schemes (diagram removal vs diagram subtraction) to take into account the interference between Wt and $t\bar{t}$ diagrams. The change in the fitted helicity fractions due to the change of single top sample was found to be negligible ($\mathcal{O}(10^{-5})$ for all fractions and is subsequently dropped from the total systematic uncertainty. Additionally, a PROTOS t-channel single top sample with anomalous Wtb couplings was used in place of the nominal t-channel single top sample to assess the impact on the extracted helicity fractions. The observed effect was also observed to be negligible ($\mathcal{O}(10^{-4})$ and dropped from consideration.

Uncertainty on the diboson backgrounds rate includes the uncertainty on the inclusive diboson NNLO cross section of ±5% [76] added in quadrature to the uncertainty of 24% due to the extrapolation to the high jet multiplicity region.

5.6.4 Signal Modeling

Initial and Final State Radiation

The uncertainties due to QCD initial- and final-state radiation (ISR/FSR) modeling are estimated with samples generated with POWHEG-BOX interfaced to Pythia and use varied values for the factorization scale (μ is varied from 0.5 to 2), the h_{damp} parameter responsible for high p_{T} radiation damping in the POWHEG-BOX generator ($h_{damp} = m_t$ for $\mu = 2$ and $h_{damp} = 2m_t$ for $\mu = 0.5$), and the transverse momentum scale of space-like parton-shower evolution in Pythia. These variations span the ranges compatible with the results of measurements of $t\bar{t}$ production in association with jets. The variation with the largest effect on the measured helicity fractions is taken as the total radiation uncertainty and symmetrized.

PDF

The PDF uncertainty on the $t\bar{t}$ signal is evaluated using a aMC@NLO $t\bar{t}$ sample following the recommendation of the PDF4LHC [17]. It takes into account the differences between three PDF sets - CT10 NLO [86], MSTW2008 68% CL NLO [12, 13] and NNPDF 2.3 NLO [16]. The final PDF uncertainty is an envelope of a) intra-PDF uncertainty, which evaluates the changes due to the variation of different PDF parameters within a single PDF error set (used for the CT10 and MSTW PDF sets) and b) inter-PDF uncertainty, which evaluates differences between different PDF sets (used for the NNPDF set). For each PDF set variation, the nominal sample is reweighted using inputs from the variation sets, and the difference between the re-weighted sample and the nominal is considered in the uncertainty envelope. The half width of the envelope of the three estimates is taken as the total PDF systematic uncertainty.

Parton Shower and Hadronization

An uncertainty due to the choice of the parton shower and hadronization model is calculated by comparing events produced by POWHEG interfaced with PYTHIA and HERWIG (h_{damp} factor set to infinity). Effects on the shapes are compared, symmetrized and applied to the shapes predicted by the default model.

Matrix Element Generator Uncertainty

An uncertainty due to the MC generator choice for the hard process is evaluated by comparing events produced by POWHEG-BOX andMC@NLO, both interfaced to HERWIG for showering and hadronization.

Top mass

The signal templates are generated with a top quark mass of $m_{top} = 172.5$ GeV. The uncertainty due to the usage of this fixed mass is evaluated pseudo-data with different input top masses for the signal processes. The obtained fractions are plotted dependent as a function of top quark mass and a slope is fitted to that curve. The uncertainty is obtained from the slope according to a change of $\pm$ 0.70 GeV taken from the $\sqrt{s} = 8$ TeV ATLAS measurement of top quark mass of 172.84 ± 0.70 GeV [120]).

5.6.5 Template statistics

To account for possible fluctuations in the templates, ensemble tests are performed. In these ensemble tests, the pseudo data distribution is not changed, but the template distributions are fluctuated within their sample statistics. The width of the distributions for the W boson helicity fractions are taken as a measure of the uncertainty that arises due to this limited template statistics. The result is comparable to the statistical uncertainty and comes mainly from the uncertainties on the signal templates due to the re-weighting method.

F_0				
Systematic uncertainty	N_{syst}	Lep 2incl	Had 1excl+2incl	Lep+Had 1excl+2incl
Reconstructed Objects				
Muon	6(3)	+0.0024 -0.0029	+0.0026 -0.0037	+0.0026 -0.0026
Electron	5(3)	+0.0028 -0.003	+0.0025 -0.0021	+0.0026 -0.003
JES	26(6)	+0.0063 -0.0033	+0.0069 -0.007	+0.0077 -0.009
JER	11(11)	+0.0062 -0.0059	+0.0274 -0.031	+0.0068 -0.0068
JVF	1(1)	+0.0036 -0.0017	+0.0129 -0.0092	+0.0025 -0.0015
b tagging	3(3)	+0.0017 -0.0021	+0.0289 -0.0307	+0.0213 -0.0211
Sum of Reco Objects	-	+0.0104 -0.0084	+0.0426 -0.0454	+0.0241 -0.0243
Modeling				
Radiation	radLo radHi	0.0033 -0.0025	0.0178 -0.0108	-0.0079 0.0025
Parton Shower	1(1)	+0.0019 -0.0019	+0.015 -0.015	+0.0072 -0.0072
ME Generator	1(1)	+0.0025 -0.0025	+0.0159 -0.0159	+0.0019 -0.0019
PDF	3(3)	+0.003 -0.003	+0.001 -0.001	+0.002 -0.002
Top Mass	3(3)	+0.002 -0.002	+0.003 -0.003	+0.001 -0.001
Sum of Modeling	-	+0.0058 -0.0058	+0.0284 -0.0284	+0.0111 -0.0111
Method Uncertainty				
Template Statistics	3(3)	+0.009 -0.009	+0.008 -0.008	+0.005 -0.005
Total Syst.	-	+0.0149 -0.0136	+0.0518 -0.0541	+0.027 -0.0271
Stat. + Bkg.	-	0.012	0.010	0.007

Table 5.12: Summary of systematic and statistical errors in the 1 exclusive + 2 inclusive b tag leptonic, hadronic, and combined leptonic and hadronic measurements of F_0. The numbers in parentheses in the N_{syst} column refer to the number of variations with corresponding templates deviating by more than two bins w.r.t. the nominal template. Errors from variations failing this condition are neglected. Systematics are grouped by their plus/minus behavior. Single-sided sources of systematic error are symmetrized. For the radiation uncertainty, the larger of the two variations is taken as the total uncertainty and symmetrized. When the difference between the up and down total systematic uncertainty is less than 0.015, the magnitude of the larger uncertainty is taken as the total symmetrized uncertainty.

F_{L}				
Systematic uncertainty	N_{syst}	Lep 2incl	Had 1excl+2incl	Lep+Had 1excl+2incl
Reconstructed Objects				
Muon	6(3)	+0.0013 -0.0015	+0.0046 -0.0035	+0.0011 -0.0008
Electron	5(3)	+0.0018 -0.002	+0.0028 -0.0038	+0.0011 -0.0014
JES	26(6)	+0.0028 -0.0025	+0.0119 -0.0078	+0.0022 -0.0032
JER	11(11)	+0.0048 -0.0018	+0.0329 -0.0407	+0.0043 -0.0019
JVF	1(1)	+0.0019 -0.0013	+0.0012 -0.0046	+0.0021 -0.0017
b tagging	3(3)	+0.0012 -0.0013	+0.0132 -0.0143	+0.0082 -0.0078
Sum of Reco Objects	-	+0.0064 -0.0044	+0.0378 -0.0444	+0.0099 -0.009
Modeling				
Radiation	radLo radHi	-0.0032 0.0058	0.0393 -0.0115	-0.006 0.0076
Parton Shower	1(1)	+0.0019 -0.0019	+0.001 -0.001	+0.0086 -0.0086
ME Generator	1(1)	+0.0032 -0.0032	+0.0242 -0.0242	+0.0016 -0.0016
PDF	3(3)	+0.003 -0.003	+0.001 -0.001	+0.002 -0.002
Top Mass	3(3)	+0.002 -0.002	+0.003 -0.003	+0.001 -0.001
Sum of Modeling	-	+0.0078 -0.0078	+0.0463 -0.0463	+0.0118 -0.0118
Method Uncertainty				
Template Statistics	3(3)	+0.006 -0.006	+0.016 -0.016	+0.004 -0.004
Total Syst.	-	+0.0135 -0.0127	+0.0603 -0.0646	+0.0162 -0.0157
Stat. + Bkg.	-	0.008	0.021	0.005

Table 5.13: Summary of systematic and statistical errors in the 1 exclusive + 2 inclusive b tag leptonic, hadronic, and combined leptonic and hadronic measurements of F_{L}. The numbers in parentheses in the N_{syst} column refer to the number of variations with corresponding templates deviating by more than two bins w.r.t. the nominal template. Errors from variations failing this condition are neglected. Systematics are grouped by their plus/minus behavior. Single-sided sources of systematic error are symmetrized. For the radiation uncertainty, the larger of the two variations is taken as the total uncertainty and symmetrized. When the difference between the up and down total systematic uncertainty is less than 0.015, the magnitude of the larger uncertainty is taken as the total symmetrized uncertainty.

			F_{R}	
Systematic uncertainty	N_{syst}	Lep 2incl	Had 1excl+2incl	Lep+Had 1excl+2incl
Reconstructed Objects				
Muon	6(3)	+0.001 -0.0015	+0.0072 -0.0072	+0.0015 -0.0017
Electron	5(3)	+0.0011 -0.0011	+0.0051 -0.0058	+0.0015 -0.0017
JES	26(6)	+0.0037 -0.0014	+0.0139 -0.0054	+0.0073 -0.0061
JER	11(11)	+0.0072 -0.0067	+0.0573 -0.0707	+0.0076 -0.0065
JVF	1(1)	+0.0017 -0.0006	+0.0114 -0.0045	+0.0003 -0.0002
b tagging	3(3)	+0.0011 -0.0012	+0.0336 -0.0349	+0.0132 -0.0132
Sum of Reco Objects	-	+0.0085 -0.0072	+0.0694 -0.0797	+0.017 -0.0161
Modeling				
Radiation	radLo radHi	-0.0001 -0.0034	-0.0573 0.022	0.014 -0.0101
Parton Shower	1(1)	+0.0037 -0.0037	+0.0144 -0.0144	+0.0013 -0.0013
ME Generator	1(1)	+0.0057 -0.0057	+0.0401 -0.0401	+0.0033 -0.0033
PDF	3(3)	+0.003 -0.003	+0.001 -0.001	+0.002 -0.002
Top Mass	3(3)	+0.002 -0.002	+0.003 -0.003	+0.001 -0.001
Sum of Modeling	-	+0.0084 -0.0084	+0.0715 -0.0715	+0.0146 -0.0146
Method Uncertainty				
Template Statistics	3(3)	+0.004 -0.004	+0.016 -0.016	+0.003 -0.003
Total Syst.	-	+0.0149 -0.0142	+0.0999 -0.1074	+0.023 -0.0223
Stat. + Bkg.	-	0.006	0.022	0.004

Table 5.14: Summary of systematic and statistical errors in the 1 exclusive + 2 inclusive b tag leptonic, hadronic, and combined leptonic and hadronic measurements of F_{R}. The numbers in parentheses in the N_{syst} column refer to the number of variations with corresponding templates deviating by more than two bins w.r.t. the nominal template. Errors from variations failing this condition are neglected. Systematics are grouped by their plus/minus behavior. Single-sided sources of systematic error are symmetrized. For the radiation uncertainty, the larger of the two variations is taken as the total uncertainty and symmetrized. When the difference between the up and down total systematic uncertainty is less than 0.015, the magnitude of the larger uncertainty is taken as the total symmetrized uncertainty.

5.7 Results

5.7.1 Combination of Helicity Fraction Measurements

The template fitting method described in Section 5.5 was applied to the full 2012 dataset in the eight independent channels (electron/muon, leptonic/hadronic, one exclusive/two inclusive b tags) described previously. The combined measurement was obtained by extending the histograms, i.e. joining the histograms from each region together end-to-end and performing the fit over the full range of bins. The total systematic uncertainty was calculated by symmetrizing all up/down variations and summing the contributions in quadrature for the systematics with up/down variations. For modeling systematics except for radiation, the full difference between the two samples was taken and symmetrized, while for radiation, the maximum difference w.r.t the nominal sample was taken and symmetrized. The summary of systematic and statistical errors are presented in tables 5.12-5.14. Table 5.15 presents the W helicity fractions measured by fitting the templates to the data using different combined regions.

Figure 5.18 shows the final template fits along with the associated statistical + systematic errors for the electron+muon combination measurement for the leptonic analyzer in two inclusive b tag region and for the hadronic analyzer in one exclusive + two inclusive b tag regions.

The measured W boson helicity fractions obtained using the leptonic branch of semileptonic $t\bar{t}$ events with $\geq$2 b-tags are:

Leptonic analyzer ($\geq$2 b-tags)
F_0 = 0.709 $\pm$ 0.012 (stat.+bkg) $^{+0.015}_{-0.014}$ (syst.)
F_L = 0.299 $\pm$ 0.008 (stat.+bkg) $^{+0.013}_{-0.012}$ (syst.)
F_R = -0.008 $\pm$ 0.006 (stat.+bkg) $\pm$0.012 (syst.)

By construction, the individual fractions sum up to one. The F_0 value is anti-correlated with both F_L and F_R (ρ_{F_0,F_L}= -0.55, ρ_{F_0,F_R}= -0.75), and F_L and F_R are positively correlated (ρ_{F_L,F_R}= +0.16). The quoted values correspond to the total correlation coefficient, considering both statistical and systematic uncertainties. These results are the most accurate W boson helicity fractions measured to date and are consistent with the SM predictions given at NNLO accuracy [62].

The most sensitive W boson helicity fractions obtained using the hadronic analyzer are measured using the combination of events with 1 b tag and $\geq$ 2b-tags. The results are given in Table 5.15. In the hadronic analyzer, the lower separation between the three W boson helicity fraction signal templates results in smaller degree of correlations but larger systematic uncertainties. Combining the leptonic and hadronic analyzers is found

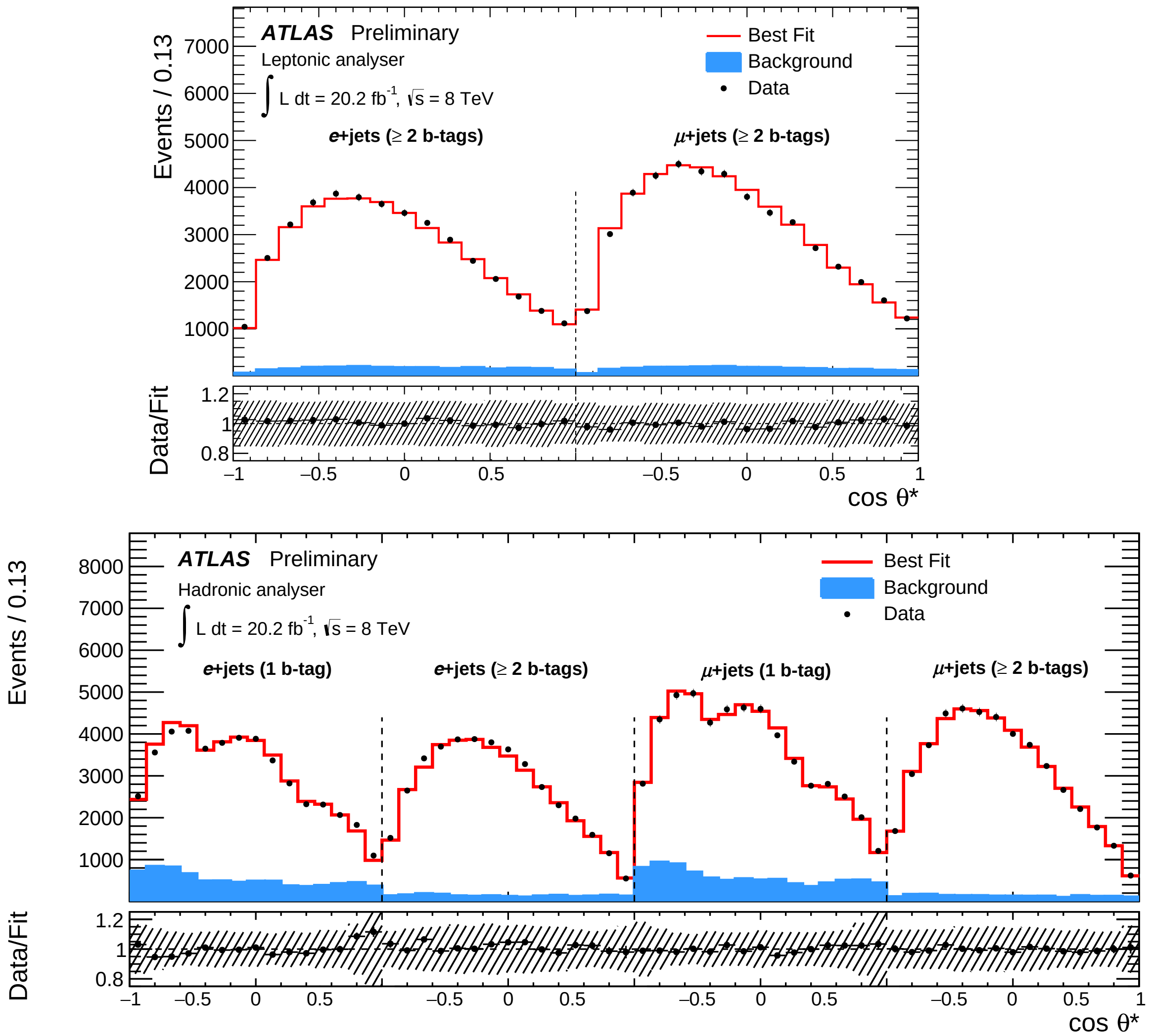

Figure 5.18: Fit results and statistical + systematic errors for the combined electron + muon channel in two inclusive (one exclusive + two inclusive) b tag region for the leptonic (hadronic) analyzer at top (bottom).

to improve the statistical error and several sources of systematic error, but the the total systematic uncertainty is found to be larger than that estimated in the leptonic, two inclusive b tag measurement. The individual leptonic and hadronic measurements do however yield consistent results in agreement with each other.

In the case of the leptonic analyzer, the dominant systematic uncertainty contributions come from jet energy scale and resolution and the limited statistics in the MC templates. The systematic uncertainties in the hadronic measurement are smaller in the one exclusive plus two inclusive b tag region compared to the two inclusive tag region alone. Adding the one exclusive region to the leptonic analyzer is not found to improve sensitivity compared to the two inclusive region measurement. The largest systematic contribution comes from the b tagging uncertainty which affects the event selection, the b tag classification, and the up- vs. down-type quark separation. Other major contributions come from jet energy resolution, the modeling of $t\bar{t}$ events (initial and final state radiation, parton showering and hadronization, and Monte Carlo generator choice for the matrix elements), all of which directly affect the object kinematics.

Leptonic, 2 Incl., $e+\mu$ Combination
F_0 = 0.709 ± 0.012 (stat.+bkg) ± 0.015 (syst.)
$F_{\rm L}$ = 0.299 ± 0.008 (stat.+bkg) ± 0.014 (syst.)
$F_{\rm R}$ = -0.008 ± 0.006 (stat.+bkg) ± 0.012 (syst.)
Lep + Had, 2 Incl., $e+\mu$ Combination
F_0 = 0.694 ± 0.009 (stat.+bkg) ± 0.029 (syst.)
$F_{\rm L}$ = 0.308 ± 0.006 (stat.+bkg) ± 0.019 (syst.)
$F_{\rm R}$ = -0.002 ± 0.005 (stat.+bkg) ± 0.016 (syst.)
Leptonic, 1 Excl. + 2 Incl., $e+\mu$ Combination
F_0 = 0.686 ± 0.010 (stat.+bkg) ± 0.043 (syst.)
$F_{\rm L}$ = 0.308 ± 0.006 (stat.+bkg) ± 0.015 (syst.)
$F_{\rm R}$ = 0.006 ± 0.005 (stat.+bkg) ± 0.035 (syst.)
Hadronic, 1 Excl. + 2 Incl., $e+\mu$ Combination
F_0 = 0.659 ± 0.010 (stat.+bkg) ± 0.054 (syst.)
$F_{\rm L}$ = 0.281 ± 0.021 (stat.+bkg) ± 0.067 (syst.)
$F_{\rm R}$ = 0.061 ± 0.022 (stat.+bkg) ± 0.108 (syst.)
Lep + Had, 1 Excl. + 2 Incl., $e+\mu$ Combination
F_0 = 0.674 ± 0.007 (stat.+bkg) ± 0.027 (syst.)
$F_{\rm L}$ = 0.315 ± 0.005 (stat.+bkg) ± 0.016 (syst.)
$F_{\rm R}$ = 0.011 ± 0.004 (stat.+bkg) ± 0.023 (syst.)

Table 5.15: Obtained W helicity fractions in different sorts of combination w.r.t the b tag, analyzer and lepton channels.

5.7.2 Constraints on Wtb Vertex

The final fitted helicity fractions can be used to constrain anomalous couplings related to the production of $t\bar{t}$. Any deviation of F_0, $F_{\rm L}$, $F_{\rm R}$ from the Standard Model prediction could be caused by new physics contributing to the Wtb vertex, and so the final fitted helicity fractions can be used to constrain any such anomalous couplings/new interactions associated with the top quark may exist at higher energies. The Wtb vertex can be parameterized in terms of an effective Lagrangian [121] above the electroweak symmetry breaking scale of $v = 246$ GeV. After electroweak symmetry breaking, this effective Lagrangian can be written as

$$\mathscr{L}_{Wtb} = -\frac{g}{\sqrt{2}}\bar{b}\gamma^{\mu}(V_L P_L + V_R P_R)tW_{\mu}^{-} - \frac{g}{\sqrt{2}}\bar{b}\frac{i\sigma^{\mu\nu}q_{\nu}}{M_W}(g_L P_L + g_R P_R)tW_{\mu}^{-} + h.c. \quad (5.22)$$

where $P_{\rm L}$ ($P_{\rm R}$) is the left-handed (right-handed) chirality operator and

$$V_L = V_{tb} + C_{\phi q}^{(3,3+3)}\frac{\nu^2}{\Lambda^2}, V_R = \frac{1}{2}C_{\phi\phi^*}^{(33)}\frac{\nu^2}{\Lambda^2}, g_L = \sqrt{2}C_{dW^*}^{(33)}\frac{\nu^2}{\Lambda^2},\ g_R = \sqrt{2}C_{uW}^{(33)}\frac{\nu^2}{\Lambda^2}, \quad (5.23)$$

The parameter Λ is the new physics scale and $C_{\phi q}^{(3,3+3)}$, $C_{\phi\phi^*}^{(33)}$, $C_{dW^*}^{(33)}$, and $C_{uW}^{(33)}$ are the effective operator coefficients. The anomalous couplings $V_{\rm R}$, $g_{\rm L}$, and $g_{\rm R}$, generated by dimension-six operators, are absent in the Standard Model at tree level while the coupling V_{tb} receives a correction from the operator $C_{\phi q}^{(3,3+3)}$. The effect of non-vanishing $V_{\rm R}$, $g_{\rm L}$, and $g_{\rm R}$ on the observables F_i has been calculated in [122,123]. As an example, Figure 5.19 shows the influence on $F_{\rm L}$ [124].

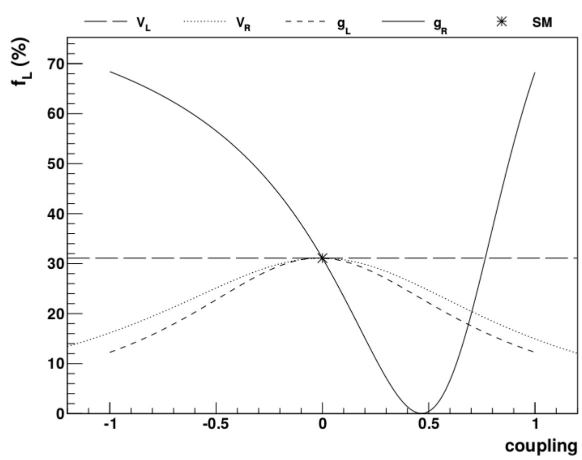

Figure 5.19: Effect of modified anomalous couplings $V_{\rm R}$, $g_{\rm L}$, and $g_{\rm R}$ on the fraction of longitudinally polarized W bosons as implemented in EFTfitter. For each coupling, the value is varied over [-1, 1] (x-axis) while the others are held fixed to their SM values.

Limits on anomalous couplings ($V_{\rm R}$, $g_{\rm L}$, and $g_{\rm R}$) are obtained from the measurement of the W boson helicity fractions in two inclusive b tag region of the leptonic analyzer by utilizing the dependence of the fractions on the couplings. The `EFTfitter` tool [124] is used to extract limits on the anomalous couplings. For simplicity, all couplings are assumed to be real. The limit setting makes use of the measured helicity fractions F_0 and F_L as well as their total uncertainties. The third fraction, F_R, is considered via the constraint of $\sum F_i = 1$. As the correct correlation between the uncertainties is crucial for the limit setting, the total covariance matrix was derived and provided as input for `EFTfitter`.

Results showing the 68% and 95.5% posterior integrals for g_L and g_R (while fixing $V_L = 1$, $V_R = 0$) can be found in Figure 5.20, as well as the 68% and 95.5% posterior integrals for g_R and V_R, while fixing the other parameters to their SM values.

In Figure 5.21, the one-dimensional limits for each anomalous coupling are shown (for all other couplings fixed to their SM expectation). The 95.5% CL intervals for the anomalous couplings are also summarized in Table 5.16.

Coupling	95.5% CL limit
V_R	$[-0.24, 0.31]$
g_L	$[-0.14, 0.11]$
g_R	$[-0.02, 0.06], [0.74, 0.78]$

Table 5.16: Limits for the anomalous couplings V_R, g_L, and g_R at 95.5 % CL. The limits were derived using the measured W helicity fractions (combination of the two channels using the leptonic analyzer in the 2-b-tag incl. channels).

The results are in good agreement with the SM expectations.

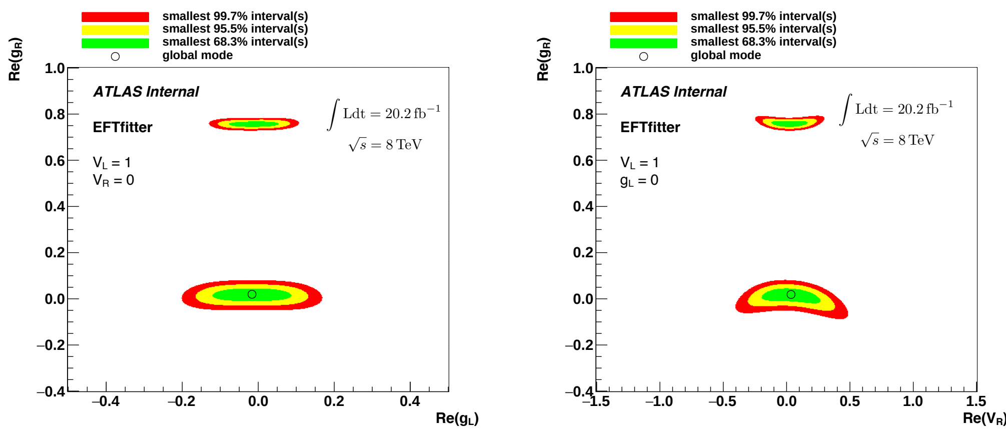

Figure 5.20: Left: Allowed regions at 68%, 95.5% and 99.7 % confidence level (CL) for the Wtb anomalous couplings $g_{\rm L}$ and $g_{\rm R}$. The other couplings are fixed to their SM expectation ($V_L = 1$, $V_R = 0$). Right: Corresponding limits on $V_{\rm R}$ and $g_{\rm R}$ for the other couplings fixed to their SM expectation. The limits were obtained using the 2-channel combination (leptonic analyzer, 2 b-jet incl.).

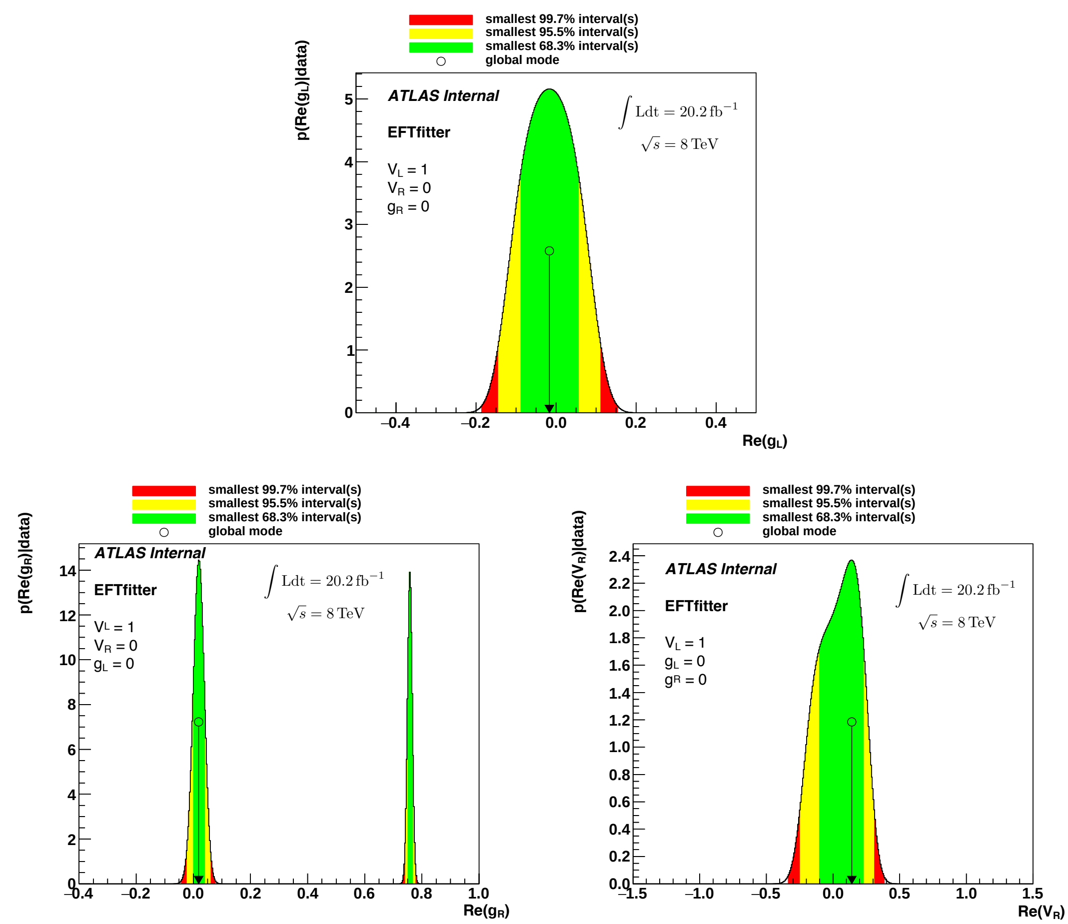

Figure 5.21: Limits on V_R, g_L and g_R while fixing the other anomalous couplings to their SM values. The limits were obtained using the 2-channel combination (leptonic analyzer, 2 b-jet incl). The arrows are drawn to explicitly show the value of the calculated global mode for each coupling.

Chapter 6
Searching for Exotic Dihiggs Production

Searching is half the fun.

- Jimmy Buffet

6.1 Introduction

The Higgs boson is an essential part of the SM and is a product of the mechanism responsible for electroweak symmetry breaking. Along with the interaction of the Higgs with the other particles of the Standard Model, the SM predicts the interaction of the Higgs boson with itself at tree-level (self-interaction). This mechanism contributes to non-resonant Higgs boson pair production together with quark-loop contributions via Yukawa-type interactions. Figure 6.1 shows a schematic diagram of non-resonant Higgs boson pair production. Since the production cross section for Higgs boson pair production is extremely small within the Standard Model,

$$\sigma_{hh}\ (13\ \text{TeV}) = 33\ \text{fb},$$

any significant enhancement would indicate the presence of new physics.

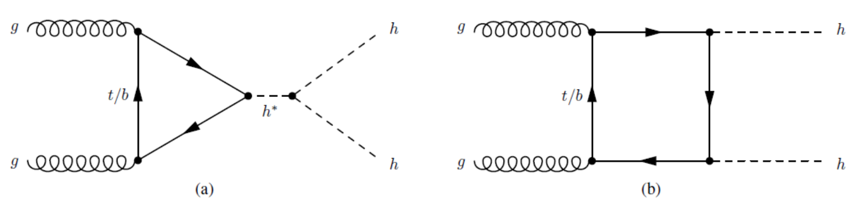

Figure 6.1: Leading order Feynman diagrams for non-resonant production of Higgs boson pairs in the Standard Model through (a) the Higgs boson self-coupling and (b) the Higgs-fermion Yukawa interaction.

Many extensions of the SM predict the existence of additional scalar bosons which may have mass larger than twice the Higgs mass and can decay into a Higgs boson pair. Searching for resonances in the hh mass spectrum can help us discover or limit exotic models which predict the presence of such particles. Figure 6.2 shows a schematic Feynman diagram of the resonant production of Higgs boson pairs with the subsequent decays $h \to WW^*$ and $h \to b\bar{b}$.

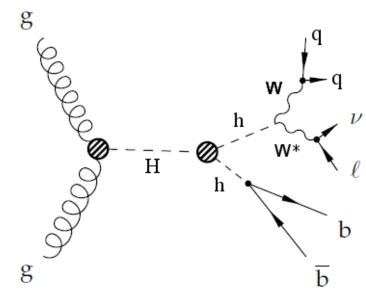

Figure 6.2: Schematic diagram of resonant Higgs boson pair production with the subsequent Higgs and W boson decays.

The following chapter discusses the results of a search for both non-resonant and resonant Higgs boson pair production with one Higgs boson decaying via $h \to b\bar{b}$, and the other via $h \to WW^* \to l\nu q\bar{q}$ (where l is either an electron or a muon). The Higgs boson decay modes chosen for this analysis are a compromise between signal sensitivity and background reduction. The $h \to WW^*$ branching ratio is the second largest after $h \to b\bar{b}$. In the semileptonic $b\bar{b}WW^*$ final state, the dominant background is $t\bar{t}$ production. This search uses the full 2015 and 2016 dataset of pp collisions produced at a center-of-mass energy of 13 TeV (corresponding to an integrated luminosity of 36.1 fb^{-1}) and recorded using the ATLAS detector at the Large Hadron Collider. This is the first search for double Higgs production using the semileptonic $b\bar{b}WW^*$ final state.

6.2 Data and Monte Carlo samples

6.2.1 Data

The analysis presented here uses the full pp collision dataset collected in 2015 and 2016 at the center-of-mass energy of 13 TeV passing data quality checks requiring good conditions of all sub-detectors. The data corresponds to an integrated luminosity of 36.1 fb^{-1} (3.2 fb^{-1}

from 2015 plus 32.8 fb^{-1} from 2016).

6.2.2 MC samples

Monte Carlo simulated events are used to estimate the Standard Model backgrounds and the signal acceptances. Table 6.1 summarizes the MC samples used for background estimation. The $t\bar{t}$ and single top-quark samples are generated with POWHEG-BOX v2 [96] using CT10

Process	Generator	$\sigma \times$ BR [pb]
$t\bar{t} \to WWbb \to l\nu bb + X$	POWHEG+PYTHIA6	451.65
Wt incl.	POWHEG+PYTHIA6	71.7
single t, s-channel, $\to l\nu + X$	POWHEG+PYTHIA6	3.31
single t, t-channel, $\to l\nu + X$	POWHEG+PYTHIA6	69.5
W+jets, $W \to l\nu$	SHERPA	20080
Z+jets, $Z \to ll$	SHERPA	2067
Dibosons incl.	SHERPA	47.3

Table 6.1: SM Monte Carlo samples used for background estimation.

parton distribution functions (PDF) interfaced to PYTHIA 6.428 [72] for parton shower, using the PERUGIA2012 [125] tune with the CTEQ6L1 [126] PDF for the underlying event descriptions. EVTGEN v1.2.0 [127] is used for properties of the bottom and charm hadron decays. The mass of the top quark is set to $m_t = 172.5$ GeV. At least one top quark in the $t\bar{t}$ event is required to decay to a final state with a lepton. The cross section of $t\bar{t}$ is known to NNLO in QCD including re-summation of next-to-next-to-leading logarithmic (NNLL) soft gluon terms, and the reference value used in ATLAS is calculated using TOP++ 2.0 [24]. The parameter HDAMP, used to regulate the high-p_{T} radiation in POWHEG, is set to m_t for good data/MC agreement in the high p_{T} region [128]. Each process of single top-quark (t-channel, s-channel and Wt-channel) is generated separately. The cross section of single-top is calculated with the prescriptions in Ref. [99, 100].

SHERPA v2.2.1 [129] with the NNPDF 3.0 [14] PDF set is used as the baseline generator for the $(W \to \ell\nu)/(Z \to \ell\ell)$+jets background. The diboson processes (WW, WZ and ZZ) are generated with SHERPA with the CT10 PDF set.

Signal samples are generated with MADGRAPH5_AMC@NLO interfaced to HERWIG++. The procedure defined in [130] is applied. It consists of generating events with an effective Lagrangian in the infinite top-quark mass approximation, and re-weighting the generated events, vertex by vertex, with form factors (FF) that take into account the finite mass of the top quark. This procedure partially accounts for the finite top-quark mass effects avoiding the need to calculate two-loop amplitudes that are still not fully available [131].

Table 6.2 shows the list of hh signals. Two sets of samples are used. The non-resonant signal sample use Standard Model production to model the kinematics while the resonant samples use a heavy Higgs scalar model as the signal hypothesis. The masses of the heavy Higgs range from 260 GeV to 3000 GeV while the Higgs width is set to 10 MeV, making the model valid in the narrow width approximation (NWA). The signals are normalized to the cross section upper limits from the Run1 ATLAS combined result [132]. Additional pp

Process	Generator
hh SM	Madgraph5_aMC@NLO + Herwig++ including FF
$H \to hh$ ($m_H = 260 - 3000$) GeV	Madgraph5_aMC@NLO + Herwig++ including FF

Table 6.2: Di-Higgs signal samples used in the analysis.

collisions generated with PYTHIA 8.186 are overlaid to model the effects of the pileup for all simulated events. All simulated events are processed with the same reconstruction algorithm used for data. Samples are processed through the full ATLAS detector simulation [93] based on GEANT4 [94].

6.3 Event selection

This analysis is based on the final state $hh \to b\bar{b}WW^* \to l\nu q\bar{q}b\bar{b}$. The semileptonic final state was chosen as a compromise between an acceptable branching fraction and the reduction of multi-jet background since the fully hadronic channel suffers from large multi-jet backgrounds while the fully leptonic channel suffers from the low branching fraction $WW^* \to l\nu l\nu$. The final state is therefore characterized by the presence of one lepton, two light jets, two b-jets, and $E_{\mathrm{T}}^{\mathrm{miss}}$ from the escaping neutrino.

Correctly identifying the pair of light jets produced by the hadronic W decay is important in the event reconstruction both for a correct reconstruction of the W and also for the higgs boson decaying to WW^* since the hadronic W information is also used to solve for the z component of the neutrino momentum. There is an additional complication due to the fact that one of the W bosons is off-shell, so there is no W mass constraint for one of the W bosons. This section details the stages of the event reconstruction and the final selection which defines the signal region. Control regions used to the background modeling are defined in Section 6.5. The signal regions are blinded (no data is shown in the signal region) since the final analysis has not yet been approved by the ATLAS collaboration. The evaluation of the background modeling and the expected sensitivity of the analysis are presented.

6.3.1 Trigger requirement

Events are selected using the un-prescaled single lepton triggers. The list of triggers used in this analysis is shown in Table 6.3. Events are selected with a logical OR between the triggers listed in Table 6.3.

6.3.2 Event pre-selection

The following selection criteria are applied before any cuts are applied on the physics objects in an event

- In order to assure good data quality, events with bad detector conditions, namely where large part of the detectors were missing from data acquisition due to problems during a run, or when the performance of the detectors were affected by large noise, have been rejected from the data analysis. Incomplete events or events with bad detector information are rejected.

- The presence of at least one primary vertex with at least two tracks is required. Among all primary vertices, the vertex with the highest $\sum p^2_{\mathrm{T,trk}}$, where $p_{\mathrm{T,trk}}$ is the transverse momentum of tracks associated with the vertex, is retained as the primary interaction vertex.

- The presence of at least one signal electron (e) or signal muon (μ) is required. The definitions for signal electrons and muons are given in Sec. 4.1.2 and Sec. 4.2.2 respectively. The signal lepton must be trigger matched to the corresponding HLT object which fires the trigger.

- There must be at least four jets surviving object selection of which two and only two are b-tagged.

6.3.3 Event Reconstruction

Events are reconstructed by first requiring exactly two b-tag jets and either two or three light jets. In events with three light jets, the pair with the lowest ΔR between them are selected as W jet candidates. This procedure yields the correct jet assignment in 70% of the cases where the hadronic daughters of the W boson can be correctly matched to reconstructed jets.

The event kinematics of the $h \to WW^* \to l\nu qq$ topology can be fully reconstructed since the only unknown component of the final state objects is the neutrino momentum

Dataset	Trigger items
2015	mu20_iloose_L1MU15 mu50 e24_lhmedium_L1EM18VH (MC) e24_lhmedium_L1EM20VH (data) e60_lhmedium e120_lhloose
2016 - Period A	mu24_iloose_L1MU15 (MC) mu24_iloose (data) mu40 e26_lhtight_nod0_ivarloose e60_lhmedium_nod0 e60_medium e140_lhloose_nod0 e300_etcut
2016 - Period B-D3	mu24_ivarmedium mu50 e26_lhtight_nod0_ivarloose e60_lhmedium_nod0 e60_lhmedium e140_lhloose_nod0 e300_etcut
2016 - Period D4-E3	mu26_ivarmedium mu50 e26_lhtight_nod0_ivarloose e60_lhmedium_nod0 e60_lhmedium e140_lhloose_nod0 e300_etcut
2016 - Period $\geq$ F	mu26_ivarmedium mu50 e26_lhtight_nod0_ivarloose e60_lhmedium_nod0 e60_lhmedium e140_lhloose_nod0 e300_etcut

Table 6.3: Summary of trigger items used for 2015 and 2016 data. For 2016 data, different triggers were used for different data run periods. All triggers are un-prescaled.

along the beam axis, p_z. Imposing the relation

$$m_h^2 = (p^l + p^\nu + p^{j1} + p^{j2})^2 \tag{6.1}$$

where p^i is the four-momenta of particle i, the neutrino p_z can be reconstructed using

$$p_E^\nu = E^\nu = \sqrt{p_{\mathrm{T}}^2 + p_z^2}, \quad p_x^\nu = p_{\mathrm{T}} \cos(\phi), \quad p_y^\nu = p_{\mathrm{T}} \sin(\phi)$$

where ϕ is the azimuthal angle of the $E_{\mathrm{T}}^{\mathrm{miss}}$, E^ν the neutrino energy, and p_x and p_y are the two transverse spatial components of the neutrino momentum. Eq. 6.1 is a quadratic expression in p_z, so it can have either two real, one real, or two complex solutions. In the last case, only the real part of the complex solution is taken into account leaving a single value of p_z. In the first case, the solution with the neutrino direction closest to the charged lepton is retained. Following this algorithm results in choosing the correct solution in approximately 60% of the selected events.

6.3.4 $b\bar{b}\tau^+\tau^-$ analysis overlap removal

In order to remove overlap with an ATLAS search for dihiggs production in the $b\bar{b}\tau^+\tau^-$ final state, events are rejected which contain at least one hadronic τ candidate. This orthogonality between analyses is useful for future efforts to combine the results of multiple dihiggs searches in order place more stringent limits than can be produced by a search in any single final state. Events containing hadronic tau candidates that fulfill the following requirements

- have $p_T > 20$ GeV and $|\eta| < 2.5$
- are reconstructed with one or three prongs
- possess unit charge
- pass a medium τ identification working point

are rejected. This rejection causes a signal efficiency loss of about 3%.

6.3.5 Kinematic selection

Since one of the largest backgrounds of this search comes from semileptonic $t\bar{t}$ decays, kinematic cuts placed on selected events designed to suppress the $t\bar{t}$ background while keeping a large signal efficiency. A schematic view of $hh \to b\bar{b}WW^*$ and the $t\bar{t} \to WbWb$ event topologies is shown in Figure 6.3. While semileptonic $t\bar{t}$ and $hh \to bbWW$ decays are both characterized by the presence two b-jets and two W bosons, the ΔR separation between the two b-jets and the two W bosons is much larger for $t\bar{t}$ events than for dihiggs

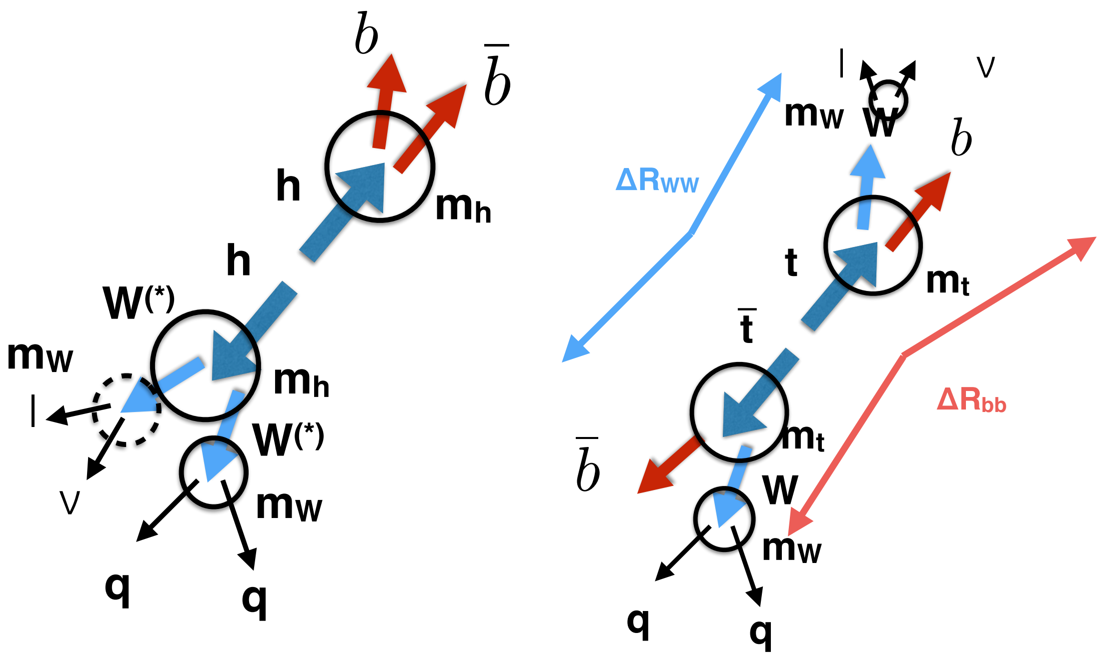

Figure 6.3: Schematic view of a $hh \to WWbb$ event compared to a $t\bar{t} \to WWbb$ event.

events. The mass spectrum of the $b\bar{b}$ pair can also be used as a discriminant since $m_{b\bar{b}}$ should be close to m_h in dihiggs events while there is no resonant value for $t\bar{t}$. The full set of variables used in the event selection variables are given by

- the p_T of the $b\bar{b}$ pair ($p_{\mathrm{T}}^{b\bar{b}}$)
- the ΔR of the $b\bar{b}$ pair ($\Delta \mathrm{R}_{b\bar{b}}$)
- the p_T of the WW pair (p_T^{WW})
- the ΔR of the WW pair (ΔR^{WW})
- the mass of the WW system computed using the calculated neutrino longitudinal momentum (m_h). This value is exactly equal to m_h if a real solution is found, it is larger if no real solution is found
- the invariant mass of the dihiggs boson system (m_{hh})
- the invariant mass of the 2 b-jets boson system ($m_{b\bar{b}}$)

6.3.6 Signal region definitions

The cuts of the selection were optimized by maximizing the Poisson significance at the end of the selection. A two step procedure has been implemented in order to final the optimal

Variable	non-resonant	low-mass	high-mass
$E_{\mathrm{T}}^{\mathrm{miss}}$ (GeV)	> 25	> 25	> 25
m_{WW} (GeV)	< 130	< 130	no-cut
p_{T}^{bb} (GeV)	> 230	> 150	> 350
$\Delta \mathrm{R}_{b\bar{b}}$	< 1.2	< 1.1	no-cut
p_{T}^{WW} (GeV)	no-cut	no-cut	> 360
ΔR_{WW}	< 1.1	< 0.9	< 2.0
m_{hh} (GeV)	no-cut	see Table 6.5	see Table 6.5
$m_{b\bar{b}}$ (GeV)	105-135	105-135	105-135

Table 6.4: Event selections for the non-resonant, low, and high mass selections. m_{hh} is not applied for non-resonant signal, and for resonant signals m_{hh} depends on the mass.

set of selection cuts. In the first step each cut is individually optimized. In the second step, all cuts are set to their optimal value and cuts are varied one by one to test the stability of the optimal point since correlations among the variables could alter the results obtained in the first step. The $t\bar{t}$ background was normalized to data in the region $m_{b\bar{b}} < 100$ GeV and $m_{b\bar{b}} > 140$ GeV (orthogonal to the final signal region) during the optimization.

Three different optimizations were produced using i) a non-resonant dihiggs signal, ii) a heavy Higgs with $m_H = 700$ GeV (low-mass), and iii) a resonant heavy Higgs with $m_H = 2000$ GeV (high mass). The resonant signals is normalized to the Run-1 upper limit scaled by the 13/8 TeV cross section ratio expected from the PDF luminosity scale of a narrow resonance of that mass. The non-resonant signal is normalized to the Standard Model expectation. The results of the optimizations for the three reference signal hypotheses are summarized in Table 6.4. In the low and high mass selections, a m_{hh} dependent cut is applied. The window edges are obtained by maximizing the expected signal significance. The m_{hh} interval used for each mass point is shown in Table 6.5.

6.4 Background estimation

The largest backgrounds in this dihiggs search at the end of selection are expected to come from $t\bar{t}$ and multi-jet production. The $t\bar{t}$ background is normalized using data while the multi-jet background is derived using a data-driven ABCD method as described in Sec. 6.4.2. For all other backgrounds (diboson, V+jets, etc), Monte Carlo samples are used after normalizing their event yields to their expected cross sections and the appropriate integrated luminosity.

Signal Mass	low-mass	high-mass
500	$[450, 550]$	$[NA]$
600	$[520, 680]$	$[NA]$
700	$[630, 770]$	$[480, 920]$
750	$[680, 820]$	$[660, 840]$
800	$[720, 880]$	$[730, 870]$
900	$[800, 1000]$	$[750, 1050]$
1000	$[940, 1060]$	$[870, 1130]$
1100	$[960, 1240]$	$[880, 1320]$
1200	$[1090, 1310]$	$[1030, 1370]$
1300	$[1180, 1420]$	$[1160, 1440]$
1400	$[1200, 1600]$	$[1210, 1590]$
1500	$[1260, 1740]$	$[1320, 1680]$
1600	$[1370, 1830]$	$[1380, 1820]$
1800	$[1560, 2040]$	$[1620, 1980]$
2000	$[1770, 2230]$	$[1770, 2230]$
2250	$[2040, 2490]$	$[2040, 2460]$
2500	$[2260, 2740]$	$[2260, 2740]$
2750	$[2520, 2980]$	$[2550, 2950]$
3000	$[2770, 3230]$	$[2790, 3210]$

Table 6.5: m_{hh} selection for the low mass and high mass searches corresponding to best discovery significance.

Variable	CR1	CR2
m_{bb}	$m_{bb} < 100$ or $m_{bb} > 140$	$m_{bb} < 100$ or $m_{bb} > 140$
m_{WW} (GeV)	< 130	no-cut
p_{T}^{bb} (GeV)	> 150	> 350

Table 6.6: Definition of the kinematic regions used to normalise the Top background. $m_{bb} < 100$ or $m_{bb} > 140$ defines the sidebands in which the control regions are defined. Expected SM backgrounds compared to the measured data after each subsequent selection cut.

CR: $m_{b\bar{b}}$ Sideband non-resonant selection					
Sample	$m_{WW} < 130$	$p_{\mathrm{T}}^{bb} > 150$	$p_{\mathrm{T}}^{bb} > 230$	$\Delta R_{bb} < 1.2$	$\Delta R_{WW} < 1.1$
$t\bar{t}$	23776.6 ± 87.2	2370.9 ± 27.5	363.8 ± 10.8	114.3 ± 5.9	91.7 ± 5.3
QCD	12587.3 ± 491.3	1028.5 ± 147.5	198.0 ± 73.3	66.9 ± 34.6	54.5 ± 29.2
W+jets	3948.2 ± 31.2	326.7 ± 6.2	91.4 ± 2.9	30.3 ± 1.7	26.0 ± 1.6
SingleTop	1605.4 ± 18.0	232.8 ± 6.6	55.1 ± 3.3	8.0 ± 1.3	5.6 ± 1.1
Dibosons	109.9 ± 2.7	17.6 ± 1.2	6.5 ± 0.8	3.9 ± 0.6	2.7 ± 0.5
Z+jets	1107.6 ± 8.4	66.9 ± 1.3	18.7 ± 0.7	5.1 ± 0.4	4.2 ± 0.4
Background Sum	43135.1± 500.3	4043.4± 150.3	733.5± 74.2	228.5± 35.2	184.6± 29.7
XhhSM	44.6 ± 2.2	18.9 ± 1.2	7.3 ± 0.6	4.6 ± 0.5	3.8 ± 0.4
Data	43199.0	3947.0	722.0	220.0	183.0

Table 6.7: The number of observed events and expected background events in the m_{bb} sidebands for the non-resonant selection. The top CR is defined at the bbpt150 selection. No NF has been applied to the background yields. Only statistical uncertainties are shown.

6.4.1 Top normalisation and control region

The $t\bar{t}$ background normalization is calculated and validated using two dedicated control regions (CR). The first control region, CR1, is defined for the non-resonant and low-mass selections while the second, CR2, is defined for the high-mass selection. The definitions for CR1 and CR2 are given in Table 6.6. Tables 6.7, 6.8, and 6.9 show the number of observed and expected background events in the $m_{b\bar{b}}$ control region for the non-resonant, low-mass, and high-mass selections before the application of $t\bar{t}$ normalization factors. The $m_{b\bar{b}}$ control region is orthogonal to the signal region due to the inversion of the $m_{b\bar{b}}$ cut.

The top normalization factors are determined by a simultaneous fit of signal and control regions, which include both top and QCD control regions 6.4.2. The factors differ between the low-mass and high-mass selections due to the different definitions of CR1 and CR2. The non-resonant selection shares CR1 and the $t\bar{t}$ normalization with the low-mass selection. The normalization factors of the two top control regions are shown in Table 6.10. Figures 6.4 and 6.5 show distributions in CR1 and CR2 for the variables used in event selection.

CR: $m_{b\bar{b}}$ Sideband low-mass selection					
Sample	$m_{WW} < 130$	$p_{\mathrm{T}}^{bb} > 150$	$\Delta R_{bb} < 1.1$	$\Delta R_{WW} < 0.9$	$630 < m_{hh} < 770$
$t\bar{t}$	23776.6 ± 87.2	2370.9 ± 27.5	763.1 ± 15.8	335.1 ± 10.6	21.5 ± 2.6
QCD	12587.3 ± 491.3	1028.5 ± 147.5	336.8 ± 82.2	146.8 ± 42.0	21.9 ± 10.2
W+jets	3948.2 ± 31.2	326.7 ± 6.2	125.2 ± 3.7	62.4 ± 2.6	9.0 ± 0.9
SingleTop	1605.4 ± 18.0	232.8 ± 6.6	45.7 ± 3.1	21.1 ± 2.1	2.1 ± 0.7
Dibosons	109.9 ± 2.7	17.6 ± 1.2	8.4 ± 0.8	4.3 ± 0.6	0.6 ± 0.2
Z+jets	1107.6 ± 8.4	66.9 ± 1.3	11.7 ± 0.5	8.5 ± 0.6	2.1 ± 0.3
Background Sum	43135.1± 500.3	4043.4± 150.3	1290.9± 83.8	578.3± 43.5	57.3± 10.6
Xhh700	4.2 ± 0.2	3.2 ± 0.2	1.8 ± 0.1	1.5 ± 0.1	0.7 ± 0.1
Data	43199.0	3947.0	1265.0	543.0	67.0

Table 6.8: The number of observed events and expected background events in the m_{bb} sidebands for the low-mass selection. The top CR is defined at the bbpt150 selection. To show how well the prediction matches data, no NF has been applied to any background. Only statistical uncertainties are shown.

CR: $m_{b\bar{b}}$ Sideband high-mass selection				
Sample	$p_{\mathrm{T}}^{bb} > 350$	$p_{\mathrm{T}}^{WW} > 360$	$\Delta R_{WW} < 2.0$	$1770 < m_{hh} < 2230$
$t\bar{t}$	8568.7 ± 52.1	5148.6 ± 40.4	2099.1 ± 26.2	327.6 ± 10.4
QCD	1298.7 ± 221.0	679.5 ± 149.5	444.0 ± 134.3	74.4 ± 27.0
W+jets	2259.5 ± 7.9	1556.2 ± 6.4	804.1 ± 4.7	142.3 ± 1.7
SingleTop	1778.1 ± 19.4	1246.1 ± 16.2	523.9 ± 10.6	81.3 ± 4.1
Dibosons	170.6 ± 3.9	115.0 ± 3.3	57.4 ± 2.3	8.8 ± 0.9
Z+jets	403.6 ± 2.1	214.8 ± 1.4	99.5 ± 1.0	18.7 ± 0.4
Background Sum	14479.1± 228.1	8960.0± 155.9	4028.0± 137.4	653.3± 29.3
Xhh2000	25.7 ± 0.4	21.7 ± 0.4	12.1 ± 0.3	5.1 ± 0.2
Data	14613.0	8945.0	4100.0	698.0

Table 6.9: The number of observed events and expected background events in the m_{bb} sidebands for the high-mass selection. The top CR is defined at the bbpt350 selection. No NF has been applied to the background yields. Only statistical uncertainties are shown.

Region	NF	$\sigma_{stat.}$
non-res and low-mass	0.94	0.03
high-mass	1.03	0.02

Table 6.10: Normalisation factors for the two CRs, the statistical error includes only data statistics, the systematic error is shown to check the compatibility of the NF with one, but it is not directly used in the fit procedure.

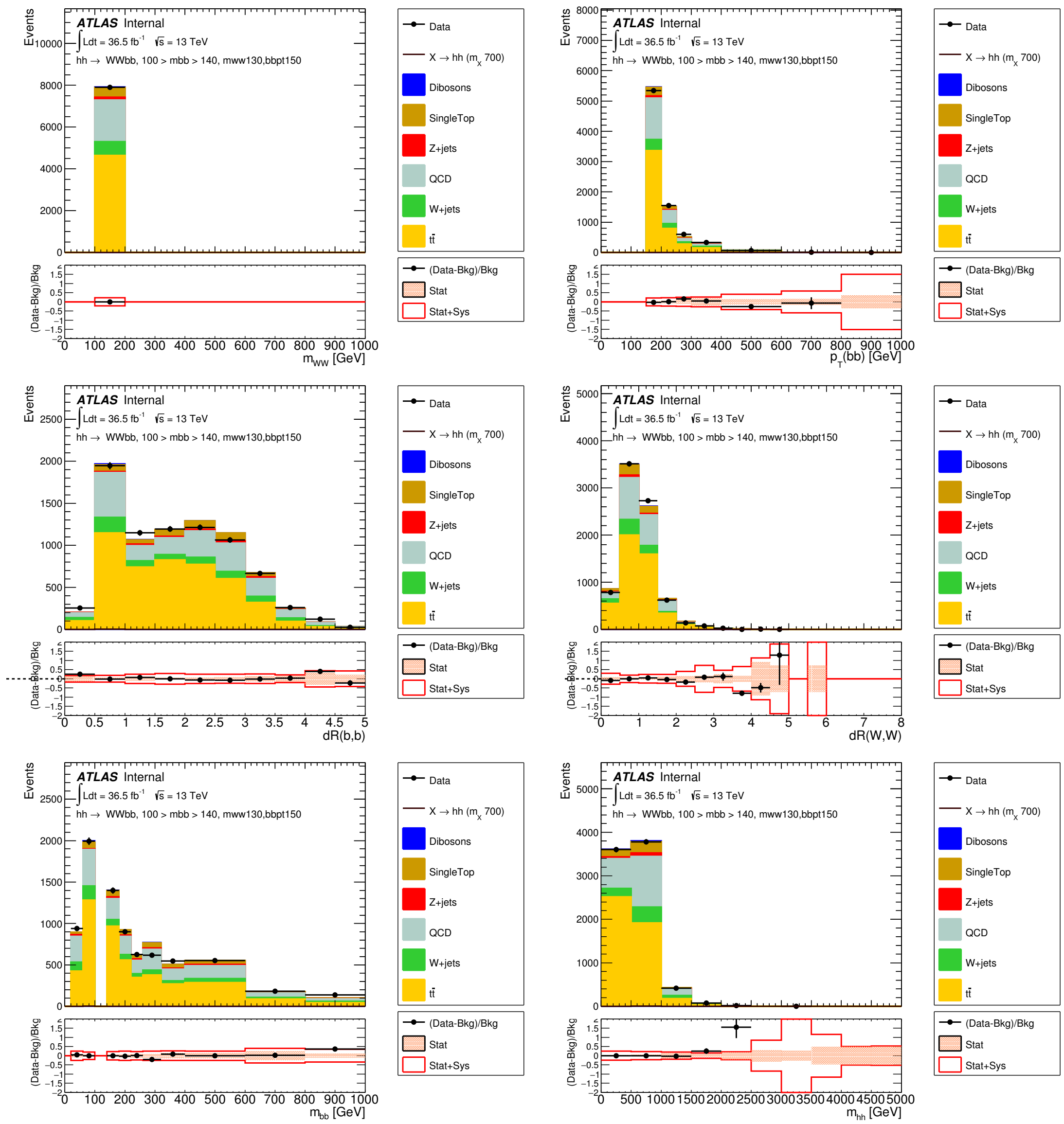

Figure 6.4: Event selection variables in CR1 for the non-resonant and low-mass selections. $t\bar{t}$ NFs as described in 6.4.1 have been applied The uncertainties shown include the statistical and systematic uncertainties described in 6.6.

6.4.2 Multi-jet background

Multi-jet backgrounds can enter in the event selection if a jet is mis-identified as an electron or a muon and used as a lepton in the analysis. Such phenomena are not accurately reproduced by MC simulation due to the large uncertainties in the jet shower shape simulation and uncertainties in jet fragmentation functions and kinematics. In order to estimate the

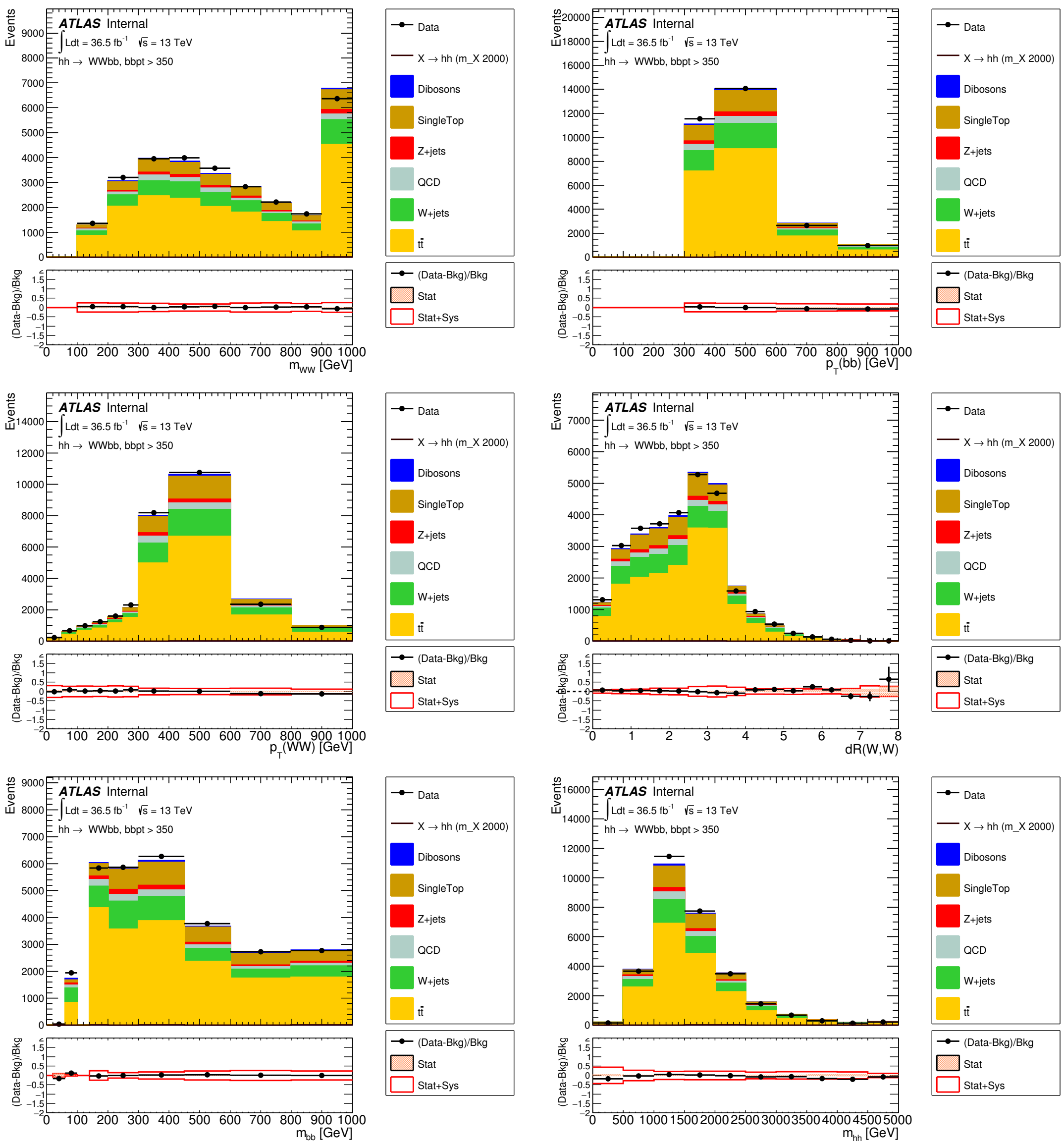

Figure 6.5: Event selection variables in CR2 for the non-resonant and low-mass selections. $t\bar{t}$ NFs as described in 6.4.1 have been applied The uncertainties shown include the statistical and systematic uncertainties described in 6.6.

contributions of multi-jet processes, a data-driven ABCD method is used to estimate this background in the present analysis.

The ABCD method uses three control regions (the B, C, and D regions) to estimate the contribution of a given background in the signal (A) region. Cuts on two ideally uncorrelated variables are used to create the signal and various control regions, e.g. the A region passes both cuts, the B and C regions each pass one cut and fail the other, while the D region fails both cuts. The absolute value of the significance of the lepton impact parameter, $|d_0/\sigma_{d_0}|$, and the missing transverse energy (MET) are used as the two variables used to define the regions in the ABCD method for this analysis. The correlation between MET and $|d_0/\sigma_{d_0}|$ was tested using $t\bar{t}$ MC, and the two variables were found to be negligibly correlated (correlation factor $\sim \mathcal{O}(10^{-2})$ at all stages of event selection. The regions are thus defined

- A region: MET > 25 GeV, $|d_0/\sigma_{d_0}| < 2.0$
- B region: MET < 25 GeV, $|d_0/\sigma_{d_0}| < 2.0$
- C region: MET > 25 GeV, $|d_0/\sigma_{d_0}| > 2.0$
- D region: MET < 25 GeV, $|d_0/\sigma_{d_0}| > 2.0$

Figure 6.6 shows a pictoral representation of the four regions.

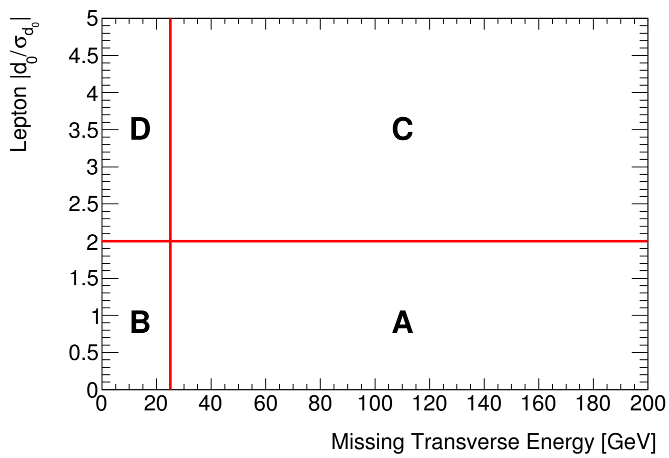

Figure 6.6: A pictoral representation of the four regions used in the ABCD calculation.

Assuming that the two variables chosen to define the ABCD regions are completely uncorrelated, the yield of the process being modeled (QCD multi-jets in this case) in the A region is given by

$$N_A = N_C \frac{N_B}{N_D} \tag{6.2}$$

where the yields N_i are yields calculated from data - all Monte Carlo backgrounds ($t\bar{t}$, W/Z+jets, single top, diboson processes) in region i ($N_i = N_i^{\text{data}} - N_i^{\text{MC Bkgs}}$). The assumption underlying Equation 6.2 is that the relationship between the yields in the B and

D regions is the same as the relationship between the A and C regions, i.e.

$$\frac{N_A}{N_C} = \frac{N_B}{N_D} \tag{6.3}$$

Using equation 6.3, the quantity $R = \frac{N_C N_B}{N_A N_D}$ can be defined. In the case of two completely uncorrelated variables, $R = 1$ and the ABCD estimation reduces to Equation 6.2. If the two variables are not completely uncorrelated, the R factor enters as a correction to Equation 6.2 for the multi-jet estimation in the A region, and the expression can be rewritten as

$$N_A = R\frac{N_C N_B}{N_D} \tag{6.4}$$

The R factor is calculated for each selection (non-resonant, low mass, and high mass) individually, and the results at each cut in each selection is provided in Table 6.11.

QCD R Values, Non-resonant Selection				
mww	bbpt150	bbpt230	drbb12	drww11
0.74 ± 0.03	0.67 ± 0.10	0.67 ± 0.24	0.57 ± 0.33	0.20 ± 0.19
QCD R Values, Low Mass Selection				
mww	bbpt150	drbb11	drww09	hh700
0.74 ± 0.03	0.67 ± 0.10	0.67 ± 0.18	0.28 ± 0.15	0.19 ± 0.72

QCD R Values, High Mass Selection			
bbpt350	wwpt360	drww20	hh2000above
0.47 ± 0.09	0.43 ± 0.11	0.46 ± 0.15	1.05 ± 0.89

Table 6.11: Values calculated for R at each stage in the non-resonant, low mass, and high mass selections. The estimate of multi-jet contribution in the A region uses the R value calculated after the first cut of each selection.

In order to minimize the dependence of R from the event selection cuts, the R value calculated after the first cut of each selection (0.74 and 0.47) is used in Equation 6.4 to estimate the multi-jet background after each subsequent cut. Once the normalization of the multi-jet background in the A region is calculated using Equation 6.4, the shape of the multi-jet template is taken from the data - Monte Carlo distribution in the C region since the two are kinematically identical except for the cut on $|d_0/\sigma_{d_0}|$.

The uncertainty due to the limited statistics in the B and D regions is the main source of the multi-jet estimation method systematics. In order to minimize this error, the yields from the B and D regions used in the ABCD calculation are frozen at a level of the cutflow to minimize statistical fluctuations. The B and D region yields are frozen after the $p_{\mathrm{T}}^{b\bar{b}} >$

230 GeV cut for the non-resonant selection, after the $\Delta R_{b\bar{b}} < 1.1$ cut for the low mass selection, and after the $\Delta R_{WW} < 2.0$ cut for the high mass selection.

Since $t\bar{t}$ and multi-jet events contaminate the control regions used for their estimation, additional studies were performed via an iterative procedure to ensure that the $t\bar{t}$ and QCD yields converge to stable values and that the estimation technique is able to disentangle between the two backgrounds. The iterative procedure begins with the QCD estimate set to zero and continues as follows:

1. Calulate $t\bar{t}$ NF at appropriate cut **before** QCD is calculated
2. Start at beginning of cutflow, apply $t\bar{t}$ NF, and calculate QCD
3. Move through cutflow to $t\bar{t}$ NF cut
4. Calculate new $t\bar{t}$ NF
5. Repeat steps 2 - 4

If the procedure converges, the estimate is said to be stable. Tables 6.12, 6.13, and 6.4.2 show the iterations for the non-resonant, low mass, and high mass selections. Iteration 0 starts with zero QCD in the background estimate. Yields are provided for QCD and $t\bar{t}$ after the first selection cut (noted as sample_first) and in the final $m_{b\bar{b}}$ signal region (noted as sample_SR). The QCD yield at the $t\bar{t}$ normalization cut is also provided. The final column shows the calculated normalization factor for $t\bar{t}$. For all selections, convergence (change in $t\bar{t}$ normalization <5%) is observed after just a few iterations for all selections.

Iteration	nQCD_first	n_QCD_nf	nQCD_SR	ttbar_first	ttbar_SR	ttbarNF
0	0.00	0.00	0.00	24637.64	65.92	1.43 ± 0.02
1	4226.57	273.95	3.30	35249.05	94.31	0.92 ± 0.02
2	15765.74	1381.06	19.04	22708.20	60.75	0.94 ± 0.03
3	15311.64	1335.16	18.33	23145.35	61.92	0.94 ± 0.03

Table 6.12: Iteration of $t\bar{t}$ normalization and QCD estimate for the non-resonant selection. The '_first' region is defined after the $m_{WW} < 130$ GeV cut and the '_nf' region is defined after requiring $p_T^{b\bar{b}} > 150$ GeV. Convergence is observed after two iterations.

Since the m_T^W distribution should contain a large multi-jet contribution at low m_T^W, the agreement between data and prediction in the m_T^W distribution for each selection acts as a

Iteration	nQCD_first	n_QCD_nf	nQCD_SR	ttbar_first	ttbar_SR	ttbarNF
0	0.00	0.00	0.00	24637.64	11.28	1.43 ± 0.02
1	4226.57	273.95	1.13	35249.05	16.14	0.92 ± 0.02
2	15765.74	1381.06	8.14	22708.20	10.40	0.94 ± 0.03
3	15311.64	1335.16	7.81	23145.35	10.60	0.94 ± 0.03

Table 6.13: Iteration of $t\bar{t}$ normalization and QCD estimate for the low mass selection. The '_first' region is defined after the $m_{WW} < 130$ GeV cut and the '_nf' region is defined after requiring $p_{\mathrm{T}}^{b\bar{b}} > 150$ GeV. Convergence is observed after two iterations.

Iteration	nQCD_first	n_QCD_nf	nQCD_SR	ttbar_first	ttbar_SR	ttbarNF
0	0.00	0.00	0.00	8810.24	6.70	1.26 ± 0.02
1	92.73	40.56	0.11	11133.25	8.47	0.99 ± 0.02
2	1595.54	541.28	1.40	8679.56	6.60	1.03 ± 0.03
3	1238.18	432.83	1.12	9063.72	6.90	1.03 ± 0.02

Table 6.14: Iteration of $t\bar{t}$ normalization and QCD estimate for the low mass selection. The '_first' region is defined after the $p_{\mathrm{T}}^{b\bar{b}} > 350$ GeV cut and the '_nf' region is defined after requiring $p_{\mathrm{T}}^{WW} > 360$ GeV. Convergence is observed after two iterations.

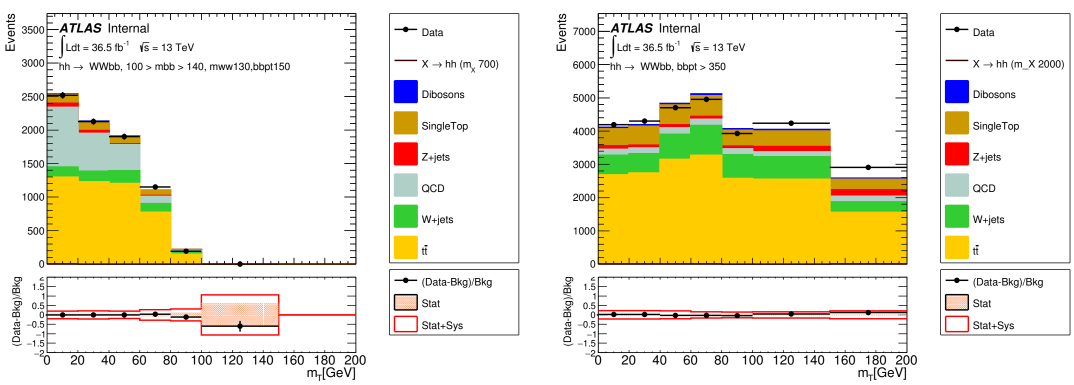

Figure 6.7: Transverse leptonic W mass plots in CR1 and CR2. $t\bar{t}$ NFs as described in 6.4.1 have been applied The percent uncertainties shown in the bottom of each plot include the statistical and systematic uncertainties described in 6.6.

closure test on the estimation of the multi-jet background by the ABCD method. Figure 6.7 shows the m_{T}^{W} distributions in CR1 and CR2. Good agreement is observed.

To evaluate the systematic error of the estimation, a Sherpa multi-b-jet sample is used to compare the ABCD prediction to the Monte Carlo expectation using events with exactly one lepton and four jets. No b-tagging requirements or other event selection cuts are applied. Pseudo-data is produced using the multi-jet Monte Carlo and events from the nominal $t\bar{t}$ Monte Carlo. The R factor is calculated using the inclusive b-tag (0, 1, or 2 b-tags) and used to estimate the QCD contribution in the two b-tag exclusive region. The percent difference between the number of events from the ABCD estimation and the number of multi-jet events from Monte Carlo used to produce the pseudo-data is taken as the systematic uncertainty. This uncertainty is calculated to be 36%.

6.5 Signal region plots and cutflow

This section presents the blinded results of the search for dihiggs production. As described previously, the blinding of the final signal region is achieved by inverting the $m_{b\bar{b}}$ cut, i.e. requiring $m_{b\bar{b}} < 100$ GeV or $m_{b\bar{b}} > 140$ GeV. Figure 6.8 shows the $m_{b\bar{b}}$ distributions with all cuts applied and the cut on $m_{b\bar{b}}$ inverted for the three selections. The low-mass and high-mass selections are shown with the hh window cuts for $m_H = 700$ GeV and $m_H = 2000$ GeV respectively. Tables 6.15, 6.16, and 6.17 show the cutflows for signals and backgrounds for full selection in the correct $m_{b\bar{b}}$ window. The signals are normalized as explained in Section 6.2.

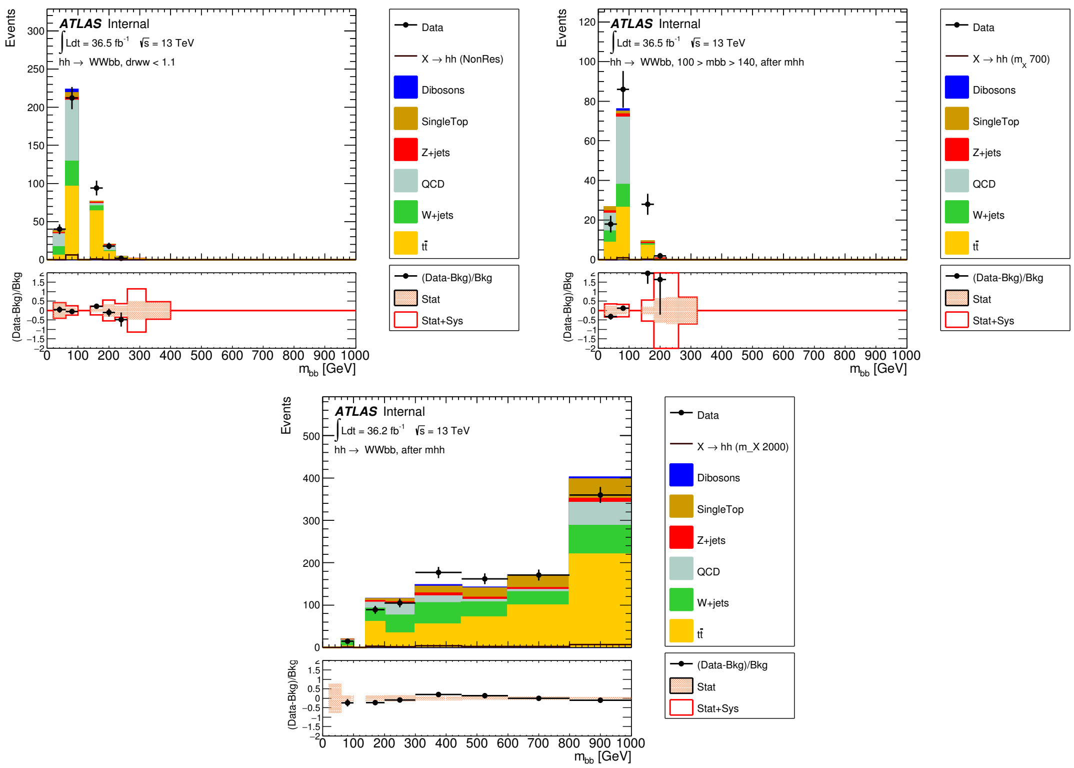

Figure 6.8: $m_{b\bar{b}}$ distributions in the final $m_{b\bar{b}}$ control region for the non-resonant, low-mass, and high-mass selections. Data is blinded in the final $m_{b\bar{b}}$ window. The low-mass and high-mass selections are shown with the hh window cuts for $m_H = 700$ GeV and $m_H = 2000$ GeV respectively. The percent uncertainties shown in the bottom of each plot include the statistical and systematic uncertainties described in 6.6.

6.6 Systematic uncertainties

This section describes the sources of systematic uncertainties considered in the analysis. These uncertainties are divided into three categories: experimental uncertainties, uncertainties on the modeling of background processes estimated from simulation, and theoretical uncertainties on the signal processes. Each systematic uncertainty is treated as a nuisance parameter in the statistical fit. These systematic variations are estimated on the final expected yield in the signal regions.

6.6.1 Experimental uncertainties

Each reconstructed object has several sources of uncertainties, each of which are evaluated separately. The leading instrumental uncertainties are the uncertainty on the b-tagging efficiency and the jet energy scale (JES). The summary of experimental uncertainties is

SR: $100 < m_{b\bar{b}} < 140$ GeV						
Sample	$m_{WW} < 130$	$p_T^{bb} > 150$	$p_T^{bb} > 230$	$\Delta R_{b\bar{b}} < 1.2$	$\Delta R_{WW} < 1.1$	$105 < m_{b\bar{b}} < 135$ GeV
tt	7461.0 ± 48.6	728.9 ± 15.1	107.7 ± 6.0	96.1 ± 5.7	79.7 ± 5.1	64.5 ± 4.7
QCD	2579.8 ± 203.9	191.0 ± 58.2	29.9 ± 24.5	22.3 ± 19.6	15.3 ± 15.2	10.8 ± 12.3
W+jets	655.5 ± 13.0	55.5 ± 2.8	14.0 ± 1.2	9.1 ± 0.9	7.6 ± 0.8	5.5 ± 0.7
Single top	452.2 ± 9.6	43.6 ± 2.8	9.4 ± 1.4	5.8 ± 1.0	4.8 ± 1.0	2.9 ± 0.7
Z+Dibosons	21.6 ± 1.3	2.8 ± 0.5	0.5 ± 0.2	0.3 ± 0.1	0.3 ± 0.1	0.4 ± 0.2
Z+jets	262.8 ± 4.4	12.0 ± 0.7	2.2 ± 0.2	1.3 ± 0.2	0.8 ± 0.1	0.5 ± 0.1
Background Sum	11433.0± 210.3	1033.9± 60.3	163.7± 25.2	134.9± 20.5	108.5± 16.1	84.6± 13.2
XhhSM	68.3 ± 2.4	44.8 ± 1.7	14.6 ± 0.6	11.7 ± 0.5	11.0 ± 0.5	9.7 ± 0.5
Data	—	—	—	—	—	—

Table 6.15: The number of expected background and signal events in the $m_{b\bar{b}}$ SR for the non-resonant selection. Data are still blinded.

SR: $100 < m_{b\bar{b}} < 140$ GeV						
Sample	$m_{WW} < 130$	$ptbb > 150$	$\Delta R_{b\bar{b}} < 1.1$	$\Delta R_{WW} < 0.9$	$630 < m_{hh} < 770$	$105 < m_{b\bar{b}} <$
tt	7461.0 ± 48.6	728.9 ± 15.1	159.0 ± 7.2	92.4 ± 5.5	20.5 ± 2.6	14.0 ± 2.1
QCD	2579.8 ± 203.9	191.0 ± 58.2	32.5 ± 28.8	29.2 ± 25.4	6.1 ± 7.3	3.7 ± 4.7
W+jets	655.5 ± 13.0	55.5 ± 2.8	10.5 ± 1.0	7.6 ± 0.8	2.8 ± 0.6	2.3 ± 0.5
Single top	452.2 ± 9.6	43.6 ± 2.8	9.4 ± 1.3	5.3 ± 1.0	0.3 ± 0.2	0.3 ± 0.2
Z+Dibosons	21.6 ± 1.3	2.8 ± 0.5	0.5 ± 0.2	0.3 ± 0.1	0.0 ± 0.0	0.0 ± 0.0
Z+jets	262.8 ± 4.4	12.0 ± 0.7	1.4 ± 0.2	0.6 ± 0.1	0.1 ± 0.0	0.0 ± 0.0
Background Sum	11433.0± 210.3	1033.9± 60.3	213.4± 29.7	135.5± 26.0	29.7± 7.8	20.3± 5.2
Xhh700	9.2 ± 0.3	8.8 ± 0.3	6.5 ± 0.2	6.1 ± 0.2	4.6 ± 0.2	4.1 ± 0.2
Data	—	—	—	—	—	—

Table 6.16: The number of expected background and signal events in the $m_{b\bar{b}}$ SR for the low-mass selection. Data are still blinded.

SR: $100 < m_{b\bar{b}} < 140$ GeV					
Sample	$p_T^{bb} > 350$	$p_T^{WW} > 360$	$\Delta R_{WW} < 2.0$	$1770 < m_{hh} < 2230$	$105 < m_{b\bar{b}} <$
$t\bar{t}$	1307.8 ± 20.2	659.7 ± 14.1	275.2 ± 9.1	9.4 ± 1.7	7.2 ± 1.5
QCD	171.4 ± 86.7	96.7 ± 54.0	67.0 ± 44.7	6.5 ± 5.7	0.5 ± 0.6
W+jets	341.3 ± 3.4	229.4 ± 2.7	127.4 ± 2.2	13.2 ± 0.5	9.7 ± 0.5
Single top	144.1 ± 5.6	97.8 ± 4.7	39.4 ± 3.0	2.1 ± 0.6	1.8 ± 0.6
Z+Dibosons	25.9 ± 1.5	18.1 ± 1.3	8.5 ± 0.8	0.2 ± 0.1	0.2 ± 0.1
Z+jets	53.8 ± 0.8	28.3 ± 0.6	13.5 ± 0.4	1.6 ± 0.1	1.4 ± 0.1
Background Sum	2044.3± 89.2	1129.8± 56.1	531.0± 45.8	32.9± 6.1	20.7± 1.8
Xhh2000	21.0 ± 0.4	16.7 ± 0.3	9.7 ± 0.3	5.8 ± 0.2	5.0 ± 0.2
Data	—	—	—	—	—

Table 6.17: The number of expected background and signal events in the $m_{b\bar{b}}$ SR for the high-mass selection. Data are still blinded.

presented in Table 6.18.

Source	Description	Analysis Name
Muons	p_{T} resolution MS	MUON_MS
Muons	p_{T} resolution ID	MUON_ID
Muons	p_{T} scale	MUON_SCALE
Muons	Isolation efficiency SF	MUON_ISO_SYS
Muons	Isolation efficiency SF	MUON_ISO_STAT
Muons	Reconstruction efficiency SF	MUON_EFF_SYS
Muons	Reconstruction efficiency SF	MUON_EFF_STAT
Muons	Trigger efficiency SF	MUON_EFF_TrigStatUncertainty
Muons	Trigger efficiency SF	MUON_EFF_TrigSystUncertainty
Electrons	p_{T} resolution	EG_RESOLUTION_ALL
Electrons	p_{T} scale	EG_SCALE_ALL
Electrons	Isolation efficiency SF	EL_EFF_Iso_TOTAL_1NPCOR_PLUS_UNCOR
Electrons	Reconstruction efficiency SF	EL_EFF_Reco_TOTAL_1NPCOR_PLUS_UNCOR
Electrons	Trigger efficiency SF	EL_EFF_Trigger_TOTAL_1NPCOR_PLUS_UNCOR
Electrons	Identification efficiency SF	EL_EFF_ID_TOTAL_1NPCOR_PLUS_UNCOR
MET	Soft term	MET_SoftTrk_ResoPerp
MET	Soft term	MET_SoftTrk_ResoPara
MET	Soft term	MET_SoftTrk_Scale
Small-R Jets	JES strongly reduced	JET_SR1_JET_GroupedNP_1
Small-R Jets	JES strongly reduced	JET_SR1_JET_GroupedNP_2
Small-R Jets	JES strongly reduced	JET_SR1_JET_GroupedNP_3
Small-R Jets	JES strongly reduced	JET_SR1_JET_EtaIntercalibration_NonClosure
Small-R Jets	Energy resolution	JET_JER_SINGLE_NP
Small-R Jets	JVT efficiency SF	JET_JvtEfficiency
b-tagging	Flavor tagging scale factors	FT_EFF_Eigen_Light_0
b-tagging	Flavor tagging scale factors	FT_EFF_Eigen_Light_1
b-tagging	Flavor tagging scale factors	FT_EFF_Eigen_Light_2
b-tagging	Flavor tagging scale factors	FT_EFF_Eigen_Light_3
b-tagging	Flavor tagging scale factors	FT_EFF_Eigen_Light_4
b-tagging	Flavor tagging scale factors	FT_EFF_Eigen_Light_5
b-tagging	Flavor tagging scale factors	FT_EFF_Eigen_Light_6
b-tagging	Flavor tagging scale factors	FT_EFF_Eigen_Light_7
b-tagging	Flavor tagging scale factors	FT_EFF_Eigen_Light_8
b-tagging	Flavor tagging scale factors	FT_EFF_Eigen_Light_9
b-tagging	Flavor tagging scale factors	FT_EFF_Eigen_Light_10
b-tagging	Flavor tagging scale factors	FT_EFF_Eigen_Light_11
b-tagging	Flavor tagging scale factors	FT_EFF_Eigen_Light_12
b-tagging	Flavor tagging scale factors	FT_EFF_Eigen_Light_13
b-tagging	Flavor tagging scale factors	FT_EFF_Eigen_B_0
b-tagging	Flavor tagging scale factors	FT_EFF_Eigen_B_1
b-tagging	Flavor tagging scale factors	FT_EFF_Eigen_B_2
b-tagging	Flavor tagging scale factors	FT_EFF_Eigen_B_3
b-tagging	Flavor tagging scale factors	FT_EFF_Eigen_B_4
b-tagging	Flavor tagging scale factors	FT_EFF_Eigen_C_0
b-tagging	Flavor tagging scale factors	FT_EFF_Eigen_C_1
b-tagging	Flavor tagging scale factors	FT_EFF_Eigen_C_2
b-tagging	Flavor tagging scale factors	FT_EFF_Eigen_C_3
b-tagging	Flavor tagging scale factors	FT_EFF_Eigen_C_4
b-tagging	Flavor tagging scale factors	FT_EFF_Eigen_extrapolation
b-tagging	Flavor tagging scale factors	FT_EFF_Eigen_extrapolation_from_charm

Table 6.18: Qualitative summary of the object systematic uncertainties included in this analysis.

Luminosity

The uncertainty in the combined 2015+2016 integrated luminosity is calculated to be 3.2%. It is derived from a preliminary calibration of the luminosity scale using x-y beam-separation scans performed in August 2015 and May 2016 [133]. The luminosity uncertainty is applied to those backgrounds estimated from simulation and the signal samples.

Trigger

Systematic uncertainties on the efficiency of electron and muon triggers are evaluated as recommended by the corresponding ATLAS combined performance groups.

Muons

The following systematic uncertainties are applied to muons in estimations based on the simulation:

- Identification efficiency: The efficiencies are measured with the tag and probe method using the Z mass peak.
- Energy and Momentum scales: These are also measured with Z mass line shape, and provided by the CP groups.

Electrons

The following systematic uncertainties are applied to electron in estimations based on the simulation:

- Identification efficiency: The efficiencies are measured with the tag and probe method using the Z mass peak.
- Energy and Momentum scales: These are also measured with Z mass line shape, and provided by the CP groups.

Jet uncertainties

The jet energy uncertainties are derived based on in situ measurements performed during Run1 and from MC simulation extrapolations from Run1 to Run2 conditions [134]. The jet energy resolution uncertainty is evaluated by smearing jet energies according to the systematic uncertainties of the resolution measurement [135]. The uncertainty in the b-tagging efficiency is evaluated by propagating the systematic uncertainty in the measured tagging efficiency for b-jets [52].

Missing transverse energy

The systematic uncertainties related to the missing transverse energy are obtained by the propagation of the systematic uncertainty on the objects that build the MET, in particular the muon, electron and jets energy resolution and scale. The resolution and scale of the MET soft-term is broken down into its components: METScale, METResoPara, METResoPerp, and full uncertainties from each component is taken into account in the final fit.

6.6.2 Background modeling uncertainties

Several systematics have been evaluated to take into account the uncertainties on the modeling of backgrounds.

Uncertainties from the modeling of $t\bar{t}$

The dominant background $t\bar{t}$ is normalized in CR1 for the low mass selection and in CR2 for the high mass selection. MC is used to extrapolate the shapes from the control regions to the signal region, so theoretical uncertainties are related to such extrapolation. PDF and scale uncertainties are evaluated by applying event selection at truth level. The resulting uncertainties are approximately 4% and included in the final fit.

Additional uncertainties in $t\bar{t}$ modeling stems from the difference in the matrix element (ME) implementation across generators, hadronization and fragmentation modeling (called parton shower, PS), and the amount of initial and final state radiation (ISR/FSR). The ME uncertainty is computed by comparing the events generated by aMC@NLO with the events generated by Powheg-Box v2, both interfaced to Herwig++ for parton shower. The difference computed close to the signal region with enough statistics is used. The PS uncertainty is computed by comparing the the nominal Powheg+Pythia6 sample with the PS variation Powheg+Herwig++ sample in a region close to the SR but with enough statistics. For ISR/FSR, the dedicated radHi and radLo samples with modified hDamp parameter are compared. The sample with the higher impact on the fit is kept as the uncertainty due to ISR/FSR. Table 6.19 shows the numbers provided to the fit for the various $t\bar{t}$ modeling systematics for the low and high mass selections. Since the uncertainties are computed based on extrapolation from the CRs, these uncertainties are input to the statistical fit as rate uncertainties in the SR only.

Single top uncertainty

Theoretical cross section uncertainties of 5.3% is assigned to the associated Wt production, 3.9% to the s-channel and 4.2% to t-channel single top production. The dominant production for this analysis is the Wt channel. The single top modeling systematic uncertainties have been calculated employing the difference between the nominal (DR scheme) and the

Source	Non-resonant	Low-Mass	High-Mass
Parton Shower	8.4	1.6	4.7
Matrix Element	1.5	0.9	11.1
ISR/FSR	8.1	13.4	5.6

Table 6.19: Extrapolation uncertainties in percentage from the CR to the SR for all selections, provided to the fit for the $t\bar{t}$ modeling systematics.

(available) systematic variation sample (DS scheme) in SR for the Wt channel. The uncertainties are computed to be 12%, 9%, and 85% for non-resonant, low-mass and high-mass analyses respectively.

W/Z+jets modeling uncertainty

Inclusive theoretical uncertainty of 6% is added in quadrature with 24% uncertainty for each additional jet. Therefore, in the final SR with 4 or 5 jets, a total uncertainty of 48% is applied. This procedure has been used in published Top Group analyses [136].

Diboson uncertainty

The same procedure as for W/Z+jets is followed.

QCD uncertainty

An overall 36% uncertainty is assigned to the QCD multi-jet background. The systematic uncertainty was calculated following the steps described in Section 6.4.2.

6.6.3 Model uncertainties on the signal

The systematic uncertainties on the modeling of the high mass $H \to hh$ signal sample have been evaluated checking the acceptance change when spanning the CT10 PDF error set, they amount to 0.4% while the uncertainties due to missing higher order has been computed varying normalization and factorization scales by a factor two and they amount to 0.6%.

6.7 Results

The data yields in all signal regions are currently blinded. In order to quantify the sensitivity of the expected background and signal, cross section σ_H limits on $pp \to hh$ production are set as a function of m_{hh} in the range 500 GeV to 3000 GeV and for the non-resonant signal. A simultaneous maximum-likelihood fit is performed for the number of events in the signal region and three control regions. Two of these correspond to the m_{bb} sideband region as defined in Section 6.4.1, with one A region and one C region as described in Section 6.4.2. The third control region corresponds to the signal region using the C region selection criteria.

The fit includes six contributions: signal, W+jets, Z+jets, $t\bar{t}$, single-top, diboson and multi-jet. The $t\bar{t}$ and multi-jet normalizations factors are free to float in the global fit while the diboson, W+jets and Z+jets backgrounds are constrained to their expected Standard Model cross-section within uncertainties. The $t\bar{t}$ modeling systematic uncertainties are applied to the yields in the signal region only as they have been extrapolated from the top control region, as described in Section 6.6.2.

The event numbers in the different regions are then modeled as:

$$
\begin{aligned}
N_{\mathrm{SR,A}} &= \sigma_{\mathrm{sig}}\mu N_{\mathrm{sig}}^{\mathrm{SR,A}} + \sigma_{t\bar{t}}\mu_{t\bar{t}}N_{t\bar{t}}^{\mathrm{SR,A}} + \sigma_{\mathrm{QCD}}\mu_{\mathrm{QCD}}N_{\mathrm{QCD}}^{\mathrm{SR,A}} + \sigma_{\mathrm{BG}}N_{\mathrm{BG}}^{\mathrm{SR,A}} \\
N_{\mathrm{SR,C}} &= \sigma_{\mathrm{sig}}\mu N_{\mathrm{sig}}^{\mathrm{SR,C}} + \mu_{t\bar{t}}N_{t\bar{t}}^{\mathrm{SR,C}} + \frac{1}{R}\left(\frac{N_{\mathrm{D}}}{N_{\mathrm{B}}}\right)\sigma_{\mathrm{QCD}}\mu_{\mathrm{QCD}}N_{\mathrm{QCD}}^{\mathrm{SR,A}} + \sigma_{\mathrm{BG}}N_{\mathrm{BG}}^{\mathrm{SR,C}} \\
N_{\mathrm{m}_{bb},\mathrm{A}} &= \sigma_{\mathrm{sig}}\mu N_{\mathrm{sig}}^{\mathrm{m}_{bb},\mathrm{A}} + \mu_{t\bar{t}}N_{t\bar{t}}^{\mathrm{m}_{bb},\mathrm{A}} + \sigma_{\mathrm{QCD}}\mu_{\mathrm{QCD}}N_{\mathrm{QCD}}^{\mathrm{m}_{bb},\mathrm{A}} + \sigma_{\mathrm{BG}}N_{\mathrm{BG}}^{\mathrm{m}_{bb},\mathrm{A}} \\
N_{\mathrm{m}_{bb},\mathrm{C}} &= \sigma_{\mathrm{sig}}\mu N_{\mathrm{sig}}^{\mathrm{m}_{bb},\mathrm{C}} + \mu_{t\bar{t}}N_{t\bar{t}}^{\mathrm{m}_{bb},\mathrm{C}} + \frac{1}{R}\left(\frac{N_{\mathrm{D}}}{N_{\mathrm{B}}}\right)\sigma_{\mathrm{QCD}}\mu_{\mathrm{QCD}}N_{\mathrm{QCD}}^{\mathrm{m}_{bb},\mathrm{A}} + \sigma_{\mathrm{BG}}N_{\mathrm{BG}}^{\mathrm{m}_{bb},\mathrm{C}}
\end{aligned}
$$

where μ is the signal strength of the $hh \to bbWW$ production and $(RN_{\mathrm{B}}/N_{\mathrm{D}})^{-1}$ is the fraction of multi-jet events in the signal region that appear in region C. The σ_i represent the systematic uncertainties associated to each contribution.

The factor $(RN_{\mathrm{B}}/N_{\mathrm{D}})^{-1}$ is obtained as described in Section 6.4.2. The initial values of the $t\bar{t}$ normalization factor and number of multi-jet events in the signal region are extracted from the third iteration of the stability test.

The fit is performed combining electron and muon channels into a single data yield. Systematic uncertainties are taken into account as nuisance parameters with Gaussian sampling distributions. For each source of systematic uncertainty, the correlations across bins and between different kinematic regions as well as those between signal and background are taken into account. The statistical analysis of the final results are based on the statistical framework used in previous Run 1 higgs [137] and dihiggs [138] analyses. Fitting and input models are handled by the RooStats [139] and RooFit [140] packages. Complete information about the statistical treatment and asymptotic formulae used to calculate the limits can be found elsewhere [141]. Profile-likelihood-ratio test statistics are used to test the hypothesis of Higgs boson pair production with its cross section as the parameter of interest. The likelihood is the product of terms of the Poisson probability constructed from the final discriminant and of nuisance parameter constraints with either Gaussian, log-normal, or Poisson distributions. Upper limits on the Higgs boson pair production cross section are derived using the $\mathrm{CL_s}$ method [142].

The expected upper limit at 95% CL on the cross-section for non-resonant Higgs boson pair production times branching fraction $\sigma(pp \to hh) \cdot \mathrm{Br}(\mathrm{hh} \to \mathrm{b\bar{b}WW^*})$ is 1.58 $\left(^{+0.62}_{-0.44}\right)$ pb which is equivalent to 191 times the SM prediction of 0.03341 pb.

The expected and observed upper limits at 95% CL on the cross-section of resonant production as a function of mass is shown in Figure 6.11. The low-mass selection is used for resonances of mass up to 1600 GeV. The high-mass selection is used for resonances of mass 1800 GeV and above. The most stringent observed (expected) limit is found for a resonant mass of 2500 GeV at 0.23 (0.45) pb. The largest deviation between the observed and expected limits is found at a resonance mass of 1800 GeV and has a local significance of 1.87 σ. The distribution of the standard deviation of observed limits with respect to the expected limits ((observed limit - expected limit) / one sigma expected deviation) is shown in Figure 6.12. The red line shows a Gaussian fit with a mean of zero and a sigma of one and has a χ^2/ndf of 2.86/3. This is consistent with an overall observation of zero signal.

Figures 6.9 and 6.10 show pull and ranking plots for all systematics included as nuisance parameters in the fit. Plots for m_X = 700, 900, 2250, and 3000 GeV for are shown using Asimov datasets[4] profiled with the signal strength parameter set to zero. The 700 and 900 GeV mass points are evaluated using the low-mass selection while the 2250 and 3000 GeV points are evaluated using the high-mass selection.

The analysis presented in this chapter represents the first ever attempt to measure di-higgs production in the semileptonic $b\bar{b}WW^*$ final state. Several updates and changes have been made between the version of the analysis presented in this dissertation and the final version published by the ATLAS collaboration. The published version uses a cutflow that was re-optimized by taking into account the systematic as well as statistical uncertainties, and the error on the QCD estimation was significantly reduced. These and other improvements lead to overall more sensitive upper limits in the public result, however both the public analysis and the version presented in this dissertation were unblinded together, and the version presented here is internally self-consistent.

[4] An Asimov dataset is an artificial, generated dataset where all simulation inputs are set to their expected values [141].

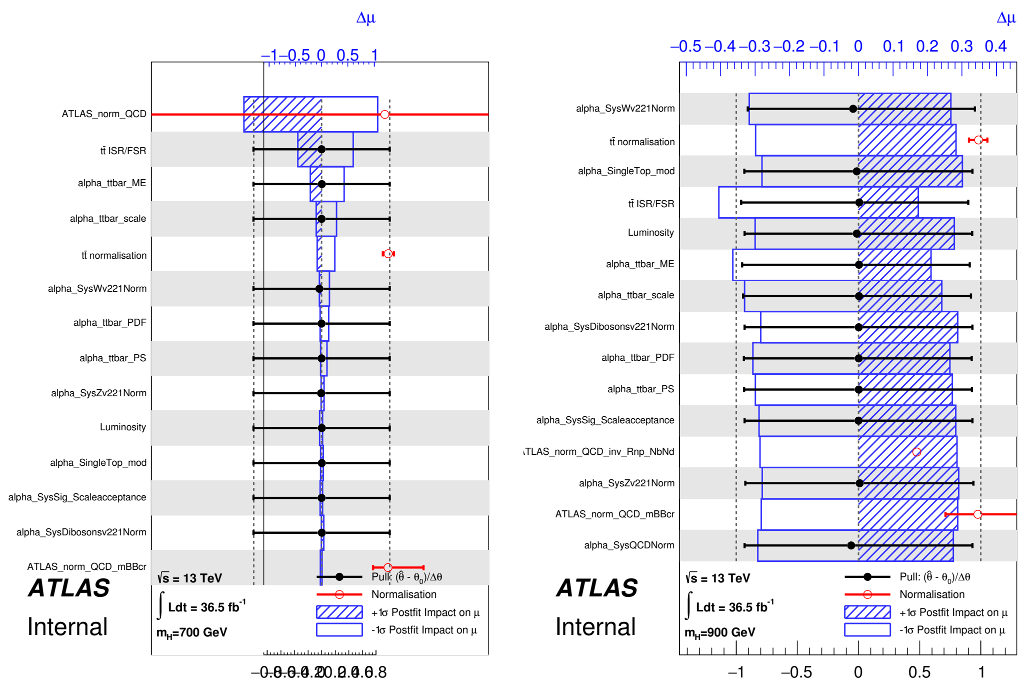

Figure 6.9: Pull plots produced when fitting to an Asimov dataset created and profiled at $\mu = 0$ for $\mathrm{m}_X = 700$ and 900 GeV for the low-mass selection. The signal strength, μ, is allowed to float as a free parameter during the fit.

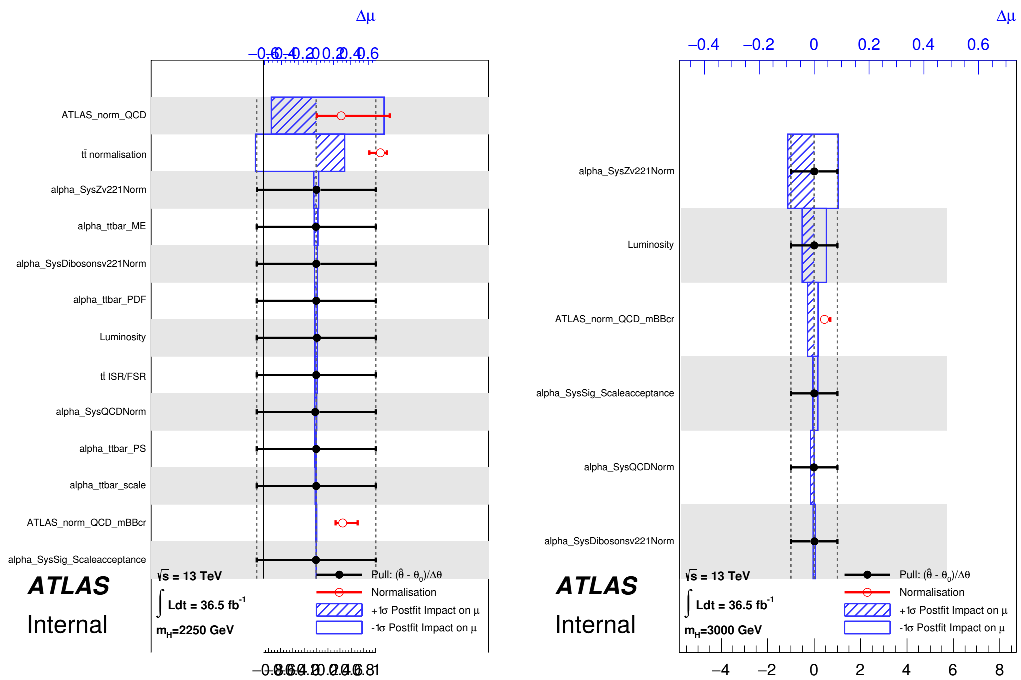

Figure 6.10: Pull plots produced when fitting to an Asimov dataset created and profiled at $\mu = 0$ for $\mathrm{m}_X = 2250$ and 3000 GeV for the high-mass selection. The signal strength, μ, is allowed to float as a free parameter during the fit.

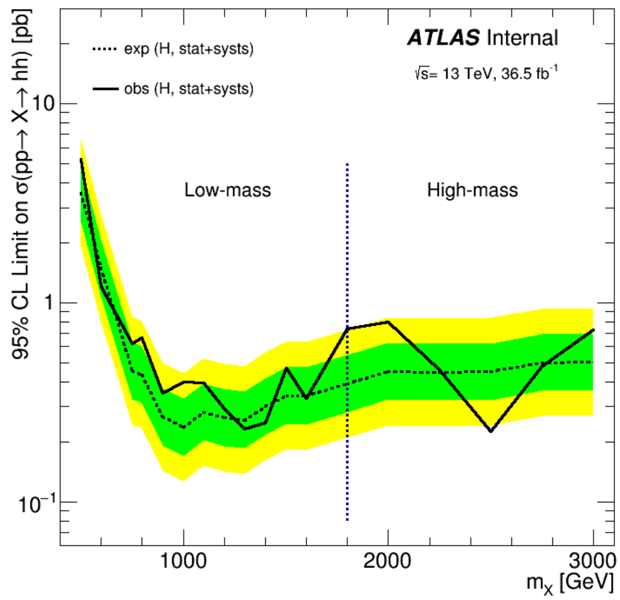

Figure 6.11: Expected and observed upper limits at 95% CL on the cross-section of resonant Higgs boson pair production as a function of resonant mass.

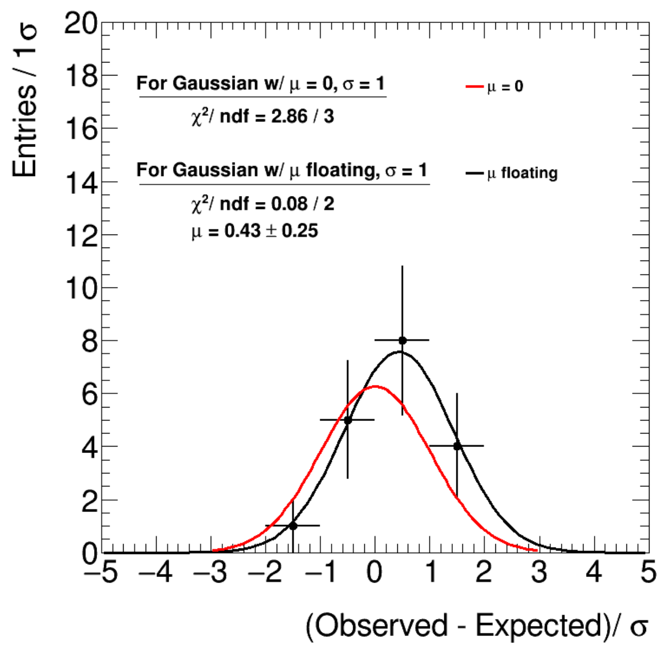

Figure 6.12: The distribution of the observed limits compared to the expected limits. The results are consistent with a unit Gaussian expectation of zero signal (red fit). A Gaussian fit with the mean allowed to float is shown for comparison.

Chapter 7
Conclusion

This thesis presented two analyses, each of which tests the predictions of the Standard Model and constrain the range of possible new theories of physics. The helicities of W bosons produced in semileptonic $t\bar{t}$ decays were measured with the highest precision to date using the decays from the leptonic W, and the world's first direct measurement was produced using the hadronically decaying W. Limits on the upper limit of resonant and non-resonant production of Higgs boson pairs was set for the first time using the semileptonic $b\bar{b}WW^*$ final state where one of the W's decays hadronically. At the end of the day, the predictions of the Standard Model were confirmed, and no evidence for the presence of new physics was observed. But that doesn't mean the search is over. There are still places to search and measurements to make.

Smashing particles together to understand their inner workings has been likened to smashing two watches together and picking through the resulting mess of glass and gears in order to understand how they kept time. While the comparison may be apt, particle colliders are one of the best tools we have for exploring the fundamental nature of our Universe. The LHC will be colliding protons and ions for years to come and at higher intensities and energies than ever before. More energetic collisions open new phase spaces for exploration; new analysis methods can improve and further the sensitivity and reach of our experiments. The application of techniques to understand and unpack the substructure of highly boosted hadronic objects and the introduction of machine learning algorithms in particle identification and event classification have already had significant impacts in many analyses. These tools and others will continue to mature in the coming years, pushing the frontier of high energy physics forward. In short, the future is bright and full of potential.

Bibliography

[1] S. L. Glashow, "Partial Symmetries of Weak Interactions," *Nucl. Phys.*, vol. 22, pp. 579–588, 1961.

[2] S. Weinberg, "A Model of Leptons," *Phys. Rev. Lett.*, vol. 19, pp. 1264–1266, 1967.

[3] A. Salam, "Weak and Electromagnetic Interactions," *Conf. Proc.*, vol. C680519, pp. 367–377, 1968.

[4] P. Langacker, *The standard model and beyond*. Series in High Energy Physics, Cosmology and Gravitation, Boca Raton, FL: Taylor and Francis, 2010.

[5] W. B. Rolnick, *The Fundamental Particles and Their Interactions*. Boston, MA: Addison-Wesley Publishing Company, Inc., 1994.

[6] D. Green, *High Pt Physics at Hadron Colliders*. Cambridge monographs on particle physics, nuclear physics, and cosmology, Cambridge: Cambridge Univ. Press, 2005.

[7] J. F. Gunion, S. Dawson, H. E. Haber, and G. L. Kane, *The Higgs hunter's guide*, vol. 80. Upton, NY: Brookhaven Nat. Lab., 1989.

[8] P. W. Higgs, "Broken symmetries and the masses of gauge bosons," *Phys. Rev. Lett.*, vol. 13, pp. 508–509, Oct 1964.

[9] F. Englert and R. Brout, "Broken symmetry and the mass of gauge vector mesons," *Phys. Rev. Lett.*, vol. 13, pp. 321–323, Aug 1964.

[10] G. S. Guralnik, C. R. Hagen, and T. W. B. Kibble, "Global conservation laws and massless particles," *Phys. Rev. Lett.*, vol. 13, pp. 585–587, Nov 1964.

[11] M. S. Carena and H. E. Haber, "Higgs Boson Theory and Phenomenology," *Prog. Part. Nucl. Phys.*, vol. 50, pp. 63–152. 87 p, Aug 2002.

[12] A. D. Martin *et al.*, "Parton distributions for the LHC," vol. 63, p. 189, 2009.

[13] A. D. Martin *et al.*, "Uncertainties on $alpha_S$ in global PDF analyses and implications for predicted hadronic cross sections," vol. 64, p. 653, 2009.

[14] H.-L. Lai, M. Guzzi, J. Huston, Z. Li, P. M. Nadolsky, *et al.*, "New parton distributions for collider physics," *Phys.Rev.*, vol. D82, p. 074024, 2010.

[15] J. Gao, M. Guzzi, J. Huston, H.-L. Lai, Z. Li, P. Nadolsky, J. Pumplin, D. Stump, and C. P. Yuan, "CT10 next-to-next-to-leading order global analysis of QCD," *Phys. Rev.*, vol. D89, no. 3, p. 033009, 2014.

[16] R. D. Ball *et al.*, "Parton distributions with LHC data," *Nucl. Phys.*, vol. B867, pp. 244–289, 2013.

[17] M. Botje *et al.*, "The PDF4LHC Working Group Interim Recommendations," 2011.

[18] J. R. Andersen *et al.*, "Handbook of LHC Higgs Cross Sections: 3. Higgs Properties," 2013.

[19] LHC Higgs Cross Section Working Group, S. Dittmaier, C. Mariotti, G. Passarino, and R. Tanaka (Eds.), "Handbook of LHC Higgs Cross Sections: 1. Inclusive Observables," *CERN-2011-002*, CERN, Geneva, 2011.

[20] G. Aad *et al.*, "Combined Measurement of the Higgs Boson Mass in pp Collisions at $\sqrt{s} = 7$ and 8 TeV with the ATLAS and CMS Experiments," *Phys. Rev. Lett.*, vol. 114, p. 191803, 2015.

[21] M. J. Dolan, C. Englert, and M. Spannowsky, "New Physics in LHC Higgs boson pair production," *Phys. Rev.*, vol. D87, no. 5, p. 055002, 2013.

[22] F. Abe *et al.*, "Observation of top quark production in $\bar{p}p$ collisions," *Phys. Rev. Lett.*, vol. 74, p. 2626, 1995.

[23] S. Abachi *et al.*, "Observation of top quark," *Phys. Rev. Lett.*, vol. 74, p. 2632, 1995.

[24] M. Czakon and A. Mitov, "Top++: A Program for the Calculation of the Top-Pair Cross-Section at Hadron Colliders," *Comput. Phys. Commun.*, vol. 185, p. 2930, 2014.

[25] P. Kant, O. M. Kind, T. Kintscher, T. Lohse, T. Martini, S. Mlbitz, P. Rieck, and P. Uwer, "HatHor for single top-quark production: Updated predictions and uncertainty estimates for single top-quark production in hadronic collisions," *Comput. Phys. Commun.*, vol. 191, pp. 74–89, 2015.

[26] M. Owen, A. Lister, and F. Deliot, "Top summary plots for ICHEP 2016," Tech. Rep. ATL-COM-PHYS-2016-1049, CERN, Geneva, Jul 2016.

[27] L. Evans and P. Bryant, "LHC Machine," *JINST*, vol. 3, p. S08001, 2008.

[28] G. Aad *et al.*, "The ATLAS Experiment at the CERN Large Hadron Collider," *JINST*, vol. 3, p. S08003, 2008.

[29] M. Aleksa *et al.*, "Results of the ATLAS solenoid magnetic field map," *J. Phys. Conf. Ser.*, vol. 110, p. 092018, 2008.

[30] "ATLAS inner detector: Technical design report. Vol. 1," 1997.

[31] "ATLAS inner detector: Technical design report. Vol. 2," 1997.

[32] M. Capeans, G. Darbo, K. Einsweiller, M. Elsing, T. Flick, M. Garcia-Sciveres, C. Gemme, H. Pernegger, O. Rohne, and R. Vuillermet, “ATLAS Insertable B-Layer Technical Design Report,” Tech. Rep. CERN-LHCC-2010-013. ATLAS-TDR-19, Sep 2010.

[33] “Particle Identification Performance of the ATLAS Transition Radiation Tracker,” Tech. Rep. ATLAS-CONF-2011-128, CERN, Geneva, Sep 2011.

[34] *ATLAS muon spectrometer: Technical Design Report.* Technical Design Report ATLAS, Geneva: CERN, 1997.

[35] “Muon Reconstruction Performance,” Tech. Rep. ATLAS-CONF-2010-064, CERN, Geneva, Jul 2010.

[36] “Performance of Missing Transverse Momentum Reconstruction in ATLAS studied in Proton-Proton Collisions recorded in 2012 at 8 TeV,” Tech. Rep. ATLAS-CONF-2013-082, CERN, Geneva, Aug 2013.

[37] “Electron performance measurements with the atlas detector using the 2010 lhc proton-proton collision data,” vol. 72, p. 1909, 2012.

[38] M. Aaboud *et al.*, “Electron efficiency measurements with the ATLAS detector using 2012 LHC proton-proton collision data,” *Eur. Phys. J.*, vol. C77, no. 3, p. 195, 2017.

[39] ATLAS Collaboration, “Electron efficiency measurements with the ATLAS detector using the 2015 LHC proton-proton collision data.” ATLAS-CONF-2016-024, Jun 2016.

[40] ATLAS Collaboration, “Electron and photon energy calibration with the ATLAS detector using LHC Run 1 data,” *Eur. Phys. J.*, vol. C74, no. 10, p. 3071, 2014.

[41] ATLAS Collaboration, “Electron and photon energy calibration with the ATLAS detector using data collected in 2015 at $\sqrt{s} = 13$ TeV,” Aug 2016.

[42] G. Aad *et al.*, “Measurement of the muon reconstruction performance of the ATLAS detector using 2011 and 2012 LHC protonproton collision data,” *Eur. Phys. J.*, vol. C74, no. 11, p. 3130, 2014.

[43] G. Aad *et al.*, “Muon reconstruction performance of the ATLAS detector in proton-proton collision data at $\sqrt{s}$ =13 TeV,” *Eur. Phys. J.*, vol. C76, no. 5, p. 292, 2016.

[44] M. Cacciari, G. P. Salam, and G. Soyez, “The anti-k_t jet clustering algorithm,” vol. 04, p. 063, 2008.

[45] M. Cacciari and G. P. Salam, “Dispelling the n^3 myth for the k_t jet-finder,” vol. B641, p. 57, 2006.

[46] M. Cacciari, G. P. Salam, and G. Soyez, “Fastjet user manual,” *Eur. Phys. J.*, vol. C72, p. 1896, 2012.

[47] ATLAS Collaboration, “The ATLAS Experiment at the CERN Large Hadron Collider,” *JINST*, vol. 3, p. S08003, 2008.

[48] C. Cojocaru *et al.*, "Hadronic calibration of the ATLAS liquid argon end-cap calorimeter in the pseudorapidity region $1.6 < |\eta| < 1.8$ in beam tests," vol. 531, p. 481, 2004.

[49] T. Barillari *et al.*, "Local hadronic calibration," *ATL-LARG-PUB-2009-001*, 2009.

[50] ATLAS Collaboration, "Jet energy measurement with the atlas detector in proton-proton collisions at $\sqrt{s} = 7$ tev," *submitted to Eur. Phys. J. C*, 2011.

[51] G. Aad *et al.*, "Performance of *b*-Jet Identification in the ATLAS Experiment," 2015.

[52] "Calibration of *b*-tagging using dileptonic top pair events in a combinatorial likelihood approach with the ATLAS experiment," Tech. Rep. ATLAS-CONF-2014-004, CERN, Geneva, Feb 2014.

[53] "Data-driven determination of the energy scale and resolution of jets reconstructed in the ATLAS calorimeters using dijet and multijet events at $\sqrt{s} = 8\ TeV$," Tech. Rep. ATLAS-CONF-2015-017, CERN, Geneva, Apr 2015.

[54] ATLAS Collaboration, "Topological cell clustering in the ATLAS calorimeters and its performance in LHC Run 1," 2016.

[55] ATLAS Collaboration, " Jet energy scale measurements and their systematic uncertainties in proton-proton collisions at sqrt(s) = 13 TeV with the ATLAS detector ," 2017.

[56] ATLAS Collaboration, "Performance of pile-up mitigation techniques for jets in pp collisions at $\sqrt{s} = 8$ TeV using the ATLAS detector," *Eur. Phys. J.*, vol. C76, no. 11, p. 581, 2016.

[57] ATLAS Collaboration, "Optimisation of the ATLAS *b*-tagging performance for the 2016 LHC Run." ATL-PHYS-PUB-2016-012, Jun 2016.

[58] "Reconstruction and calibration of missing transverse energy and performance in z and w events in atlas proton-proton collisions at 7 tev," *ATLAS-CONF-2011-080*, 2011.

[59] ATLAS Collaboration, " Performance of missing transverse momentum reconstruction for the ATLAS detector in the first proton-proton collisions at $\sqrt{s}$= 13 TeV ." ATL-PHYS-PUB-2015-027, Jul 2015.

[60] "First combination of Tevatron and LHC measurements of the top-quark mass," Tech. Rep. arXiv:1403.4427. ATLAS-CONF-2014-008. CDF-NOTE-11071. CMS-PAS-TOP-13-014. D0-NOTE-6416, CERN, Geneva, Mar 2014. Comments: 34 pages, 7 figures.

[61] M. Beneke *et al.*, "Top quark physics," in *1999 CERN Workshop on standard model physics (and more) at the LHC, CERN, Geneva, Switzerland, 25-26 May: Proceedings*, pp. 419–529, 2000.

[62] A. Czarnecki *et al.*, "Helicity fractions of W bosons from top quark decays at NNLO in QCD," *Phys. Rev*, vol. D81, p. 111503, 2010.

[63] M. Fischer, S. Groote, J. G. Korner, M. C. Mauser, and B. Lampe, "Polarized top decay into polarized W: t(polarized) —¿ W(polarized) + b at O(alpha-s)," *Phys. Lett.*, vol. B451, pp. 406–413, 1999.

[64] G. Aad *et al.*, "Measurement of the W boson polarization in top quark decays with the ATLAS detector," *JHEP*, vol. 06, p. 088, 2012.

[65] S. Chatrchyan *et al.*, "Measurement of the W-boson helicity in top-quark decays from $t\bar{t}$ production in lepton+jets events in pp collisions at $\sqrt{s} = 7$ TeV," *JHEP*, vol. 10, p. 167, 2013.

[66] V. Khachatryan *et al.*, "Measurement of the W boson helicity fractions in the decays of top quark pairs to lepton + jets final states produced in pp collisions at $\sqrt{s} =$ 8TeV," *Phys. Lett.*, vol. B762, pp. 512–534, 2016.

[67] V. M. Abazov *et al.*, "Model-independent measurement of the W boson helicity in top quark decays at D0," *Phys. Rev. Lett.*, vol. 100, p. 062004, 2008.

[68] "Selection of jets produced in proton-proton collisions with the atlas detector using 2011 data," *ATLAS-CONF-2012-020*, 2012.

[69] ATLAS Collaboration, "Measurement of the top quark-pair production cross section with ATLAS in pp collisions at $\sqrt{s} = 7$ TeV," vol. 71, p. 1577, 2011.

[70] M. L. Mangano *et al.*, "ALPGEN, a generator for hard multiparton processes in hadronic collisions," vol. 07, p. 001, 2003.

[71] P. M. Nadolsky *et al.*, "Implications of CTEQ global analysis for collider observables," vol. 78, p. 013004, 2008.

[72] T. Sjostrand, S. Mrenna, and P. Z. Skands, "PYTHIA 6.4 Physics and Manual," *JHEP*, vol. 05, p. 026, 2006.

[73] M. L. Mangano *et al.*, "Multijet matrix elements and shower evolution in hadronic collisions: $Wb\bar{b} + n$ jets as a case study," vol. B 632, p. 343, 2002.

[74] A. Juste, R. Hawking, H. Helsens, M. Huhtinen, D. Marley, A. McCarn, F. Rubbo, T. Schwarz, and J. A. Aguilar Saavedra, "Measurement of the charge asymmetry in top quark pair production in pp collision data at $\sqrt{s} = 8\ TeV$ using the ATLAS detector.," Tech. Rep. ATL-COM-PHYS-2014-087, CERN, Geneva, Feb 2014.

[75] K. Melnikov and F. Petriello, "Electroweak gauge boson production at hadron colliders through $\mathcal{O}(\alpha_s^2)$," vol. 74, p. 114017, 2006.

[76] J. Campbell and R. Ellis, "An update on vector boson pair production at hadron colliders," vol. 60, p. 113006, 1999.

[77] P. Nason, "A new method for combining NLO QCD with shower Monte Carlo algorithms," vol. 11, p. 040, 2004.

[78] S. Frixione, P. Nason, and C. Oleari vol. 11, p. 070, 2007.

[79] S. Alioli, P. Nason, C. Oleari, and E. Re vol. 06, p. 040, 2010.

[80] M. C. et al., "Top-top-pair production at hadron colliders with next-to-next-to-leading logarithmic soft-gluon resummation," vol. B710, p. 612, 2012.

[81] P. B. et al., "Percent level precision physics at the tevatron: First genuine nnlo qcd corrections to $q\bar{q} \to t\bar{t}$," vol. 109, p. 132001, 2012.

[82] M. Czakon and A. Mitov, "NNLO corrections to top-pair production at hadron colliders: the all-fermionic scattering channels," *JHEP*, vol. 12, p. 054, 2012.

[83] M. Czakon and A. Mitov, "NNLO corrections to top pair production at hadron colliders: the quark-gluon reaction," *JHEP*, vol. 01, p. 080, 2013.

[84] P. F. M. Czakon and A. Mitov, "The total top quark pair production cross-section at hadron colliders through $\mathcal{O}(\alpha_s^4)$," vol. 110, p. 252004, 2013.

[85] G. Aad *et al.*, "Search for the Standard Model Higgs boson produced in association with top quarks and decaying into $b\bar{b}$ in pp collisions at $\sqrt{s} = 8$ TeV with the ATLAS detector," *Eur. Phys. J.*, vol. C75, no. 7, p. 349, 2015.

[86] H.-L. Lai *et al.*, "New parton distributions for collider physics," vol. 82, p. 074024, 2010.

[87] S. Frixione, E. Laenen, P. Motylinski, and B. R. Webber, "Single-top production in MC@NLO," vol. 03, p. 092, 2006.

[88] N. Kidonakis, "Next-to-next-to-leading-order collinear and soft gluon corrections for t-channel single top quark production," vol. 83, p. 091503, 2011.

[89] N. Kidonakis, "Next-to-next-to-leading logarithm resummation for s-channel single top quark production," vol. 81, p. 054028, 2010.

[90] J. Butterworth, J. Forshaw, and M. Seymour, "Multiparton interactions in photoproduction at HERA," vol. 72, p. 637, 1996.

[91] P. Golonka and Z. Wąs, "Photos monte carlo: a precision tool for qed corrections in z and w decays," vol. 45, p. 97, 2006.

[92] S. Jadach, J. H. Kühn, and Z. Waąs, "Tauola - a library of monte carlo programs to simulate decays of polarized τ leptons," vol. 64, p. 275, 1991.

[93] G. Aad *et al.*, "The ATLAS Simulation Infrastructure," *Eur.Phys.J.*, vol. C70, pp. 823–874, 2010.

[94] S. Agostinelli *et al.*, "GEANT4: A Simulation toolkit," *Nucl.Instrum.Meth.*, vol. A506, pp. 250–303, 2003.

[95] P. Nason, "A New method for combining NLO QCD with shower Monte Carlo algorithms.," *JHEP*, vol. 11, p. 040, 2004.

[96] S. Frixione, P. Nason, and C. Oleari, "Matching NLO QCD computations with Parton Shower simulations: the POWHEG method," *JHEP*, vol. 11, p. 070, 2007.

[97] S. Alioli, P. Nason, C. Oleari, and E. Re, "A general framework for implementing NLO calculations in shower Monte Carlo programs: the POWHEG BOX," *JHEP*, vol. 06, p. 043, 2010.

[98] K. Melnikov and F. Petriello, "Electroweak gauge boson production at hadron colliders through $O(\alpha_s^2)$," *Phys. Rev. D.*, vol. 74, p. 114017., 2006.

[99] N. Kidonakis, "Next-to-next-to-leading-order collinear and soft gluon corrections for t-channel single top quark production," *Phys. Rev.*, vol. D83, p. 091503, 2011.

[100] N. Kidonakis, "Two-loop soft anomalous dimensions for single top quark associated production with a W- or H-," *Phys. Rev.*, vol. D82, p. 054018, 2010.

[101] N. Kidonakis, "NNLL resummation for s-channel single top quark production," *Phys. Rev. D.*, vol. 81, p. 054028, 2010.

[102] J. Campbell and R. Ellis, "An update on vector boson pair production at hadron colliders," *Phys. Rev. D.*, vol. 60, pp. 113006,, 1999.

[103] J. Erdmann, S. Guindon, K. Kroeninger, B. Lemmer, O. Nackenhorst, A. Quadt, and P. Stolte, "A likelihood-based reconstruction algorithm for top-quark pairs and the KLFitter framework," *Nucl. Instrum. Meth.*, vol. A748, pp. 18–25, 2014.

[104] A. Caldwell, D. Kollar, and K. Kroninger, "BAT: The Bayesian Analysis Toolkit," *Comput. Phys. Commun.*, vol. 180, pp. 2197–2209, 2009.

[105] M. Jezabek and J. H. Kuhn, "V-A tests through leptons from polarized top quarks," *Phys. Lett.*, vol. B329, pp. 317–324, 1994.

[106] A. Brandenburg, Z. G. Si, and P. Uwer, "QCD corrected spin analyzing power of jets in decays of polarized top quarks," *Phys. Lett.*, vol. B539, pp. 235–241, 2002.

[107] "Measurements of spin correlation in top-antitop quark events from proton-proton collisions at $\sqrt{s} = 7$ TeV using the ATLAS detector," *Phys.Rev.*, vol. D90, no. 11, p. 112016, 2014.

[108] F. James and M. Roos, "MINUIT: a system for function minimization and analysis of the parameter errors and corrections," *Comput. Phys. Commun.*, vol. 10, pp. 343–367. 38 p, Jul 1975.

[109] R. Brun and F. Rademakers, "ROOT: An object oriented data analysis framework," *Nucl. Instrum. Meth.*, vol. A389, pp. 81–86, 1997.

[110] G. Aad *et al.*, "Measurement of the top quark-pair production cross section with ATLAS in pp collisions at $\sqrt{s} = 7$ TeV," *Eur. Phys. J.*, vol. C71, p. 1577, 2011.

[111] A. Collaboration, "Luminosity Determination in pp Collisions at $\sqrt{s} = 8$ TeV using the ATLAS Detector at the LHC," Tech. Rep. ATL-COM-DAPR-2015-014, CERN, Geneva, Aug 2015. Journal draft for EdBoard review.

[112] "In-situ jet energy scale and jet shape corrections for multiple interactions in the first ATLAS data at the LHC." ATLAS-CONF-2011-030, 2011.

[113] "In-situ pseudorapidity intercalibration for evaluation of jet energy scale uncertainty using dijet events in proton-proton collisions at $\sqrt{s} = 7$ TeV." ATLAS-CONF-2011-014, 2011.

[114] "Jet energy resolution and selection efficiency relative to track jets from in-situ techniques with the ATLAS Detector Using Proton-Proton Collisions at a Center of Mass Energy $\sqrt{s} = 7$ TeV." ATLAS-CONF-2010-054, 2010.

[115] "JetUncertainties twiki:," We are using tag JetUncertainties-00-05-07.

[116] B. Malaescu, D. I. Gillberg, M. Begel, R. Camacho Toro, J. Taenzer, J. Lacey, S. Lammers, D. Lopez Mateos, C. Issever, Z. Marshall, A. Pilkington, F. Ruehr, C. Sawyer, P. Starovoitov, M. Vetterli, and C. J. Young, "Determination of jet calibration and energy resolution in proton-proton collisions at $\sqrt{s} = 8$ TeV using the ATLAS detector," Tech. Rep. ATL-COM-PHYS-2015-1086, CERN, Geneva, Sep 2015.

[117] "JetEnergyResolutionProvider twiki:," We are using tag JetResolution-01-00-00.

[118] M. Bosman *et al.*, "Weighting method to propagate heavy-flavor tagging calibrations and related uncertainties," *ATL-COM-PHYS-2010-331*, 2010.

[119] "Estimation of the W+Jets Background for Top Quark Re-Discovery in the Single Lepton+Jets Channel," *ATL-COM-PHYS-2010-834*, 2010.

[120] ATLAS Collaboration, "Measurement of the top pair production cross section in 8 TeV proton–proton collisions using kinematic information in the lepton+jets final state with ATLAS," *Phys. Rev. D*, vol. 91, p. 112013, 2015.

[121] J. A. Aguilar-Saavedra, J. Carvalho, N. F. Castro, F. Veloso, and A. Onofre, "Probing anomalous Wtb couplings in top pair decays," *Eur.Phys*, vol. J, p. 519, 2007.

[122] J. A. Aguilar-Saavedra, J. Carvalho, N. F. Castro, F. Veloso, and A. Onofre, "Probing anomalous Wtb couplings in top pair decays," *Eur. Phys. J.*, vol. C50, pp. 519–533, 2007.

[123] F. Bach and T. Ohl, "Anomalous Top Couplings at Hadron Colliders Revisited," *Phys. Rev.*, vol. D86, p. 114026, 2012.

[124] N. Castro, J. Erdmann, C. Grunwald, K. Kröninger, and N.-A. Rosien, "EFTfitter—A tool for interpreting measurements in the context of effective field theories," 2016.

[125] P. Z. Skands, "Tuning Monte Carlo Generators: The Perugia Tunes," *Phys.Rev.*, vol. D82, p. 074018, 2010.

[126] J. Pumplin, D. Stump, J. Huston, H. Lai, P. M. Nadolsky, *et al.*, "New generation of parton distributions with uncertainties from global QCD analysis," *JHEP*, vol. 0207, p. 012, 2002.

[127] D. J. Lange, "The EvtGen particle decay simulation package," *Nucl. Instrum. Meth.*, vol. A462, pp. 152–155, 2001.

[128] "Comparison of Monte Carlo generator predictions for gap fraction and jet multiplicity observables in top-antitop events," Tech. Rep. ATL-PHYS-PUB-2014-005, CERN, Geneva, May 2014.

[129] T. Gleisberg, S. Hoeche, F. Krauss, M. Schonherr, S. Schumann, *et al.*, "Event generation with SHERPA 1.1," *JHEP*, vol. 0902, p. 007, 2009.

[130] R. Frederix, S. Frixione, V. Hirschi, F. Maltoni, O. Mattelaer, P. Torrielli, E. Vryonidou, and M. Zaro, "Higgs pair production at the LHC with NLO and parton-shower effects," *Phys. Lett.*, vol. B732, pp. 142–149, 2014.

[131] G. Degrassi, P. P. Giardino, and R. Grber, "On the two-loop virtual QCD corrections to Higgs boson pair production in the Standard Model," *Eur. Phys. J.*, vol. C76, no. 7, p. 411, 2016.

[132] G. Aad *et al.*, "Searches for Higgs boson pair production in the $hh \to bb\tau\tau, \gamma\gamma WW^*, \gamma\gamma bb, bbbb$ channels with the ATLAS detector," *Phys. Rev.*, vol. D92, p. 092004, 2015.

[133] M. Aaboud *et al.*, "Luminosity determination in pp collisions at $\sqrt{s} = 8$ TeV using the ATLAS detector at the LHC," *Eur. Phys. J.*, vol. C76, no. 12, p. 653, 2016.

[134] "Jet Calibration and Systematic Uncertainties for Jets Reconstructed in the ATLAS Detector at $\sqrt{s} = 13$ TeV," Tech. Rep. ATL-PHYS-PUB-2015-015, CERN, Geneva, Jul 2015.

[135] G. Aad *et al.*, "Jet energy measurement and its systematic uncertainty in proton-proton collisions at $\sqrt{s} = 7$ TeV with the ATLAS detector," *Eur. Phys. J.*, vol. C75, p. 17, 2015.

[136] J. Alwall *et al.*, "Comparative study of various algorithms for the merging of parton showers and matrix elements in hadronic collisions," *Eur. Phys. J.*, vol. C53, pp. 473–500, 2008.

[137] G. Aad *et al.*, "Combined search for the Standard Model Higgs boson in pp collisions at $\sqrt{s} = 7$ TeV with the ATLAS detector," *Phys. Rev.*, vol. D86, p. 032003, 2012.

[138] ATLAS Collaboration, "Searches for Higgs boson pair production in the $hh \to bb\tau\tau, \gamma\gamma WW*, \gamma\gamma bb, bbbb$ channels with the ATLAS detector," *Phys. Rev. D*, vol. 92, p. 092004. 25 p, Sep 2015. Comments: 25 pages plus author list + cover pages (42 pages total), 7 figures, 6 tables, submitted to Phys. Rev. D. All figures including auxiliary figures are available at https://atlas.web.cern.ch/Atlas/GROUPS/PHYSICS/PAPERS/HIGG-2013-33/.

[139] L. Moneta, K. Cranmer, G. Schott, and W. Verkerke, "The RooStats project," in *Proceedings of the 13th International Workshop on Advanced Computing and Analysis Techniques in Physics Research. February 22-27, 2010, Jaipur, India. http://acat2010.cern.ch/. Published online at ¡A href="http://pos.sissa.it/cgi-bin/reader/conf.cgi?confid=93"¿http://pos.sissa.it/cgi-bin/reader/conf.cgi?confid=93¡/A¿, p.57*, p. 57, 2010.

[140] W. Verkerke and D. Kirkby, "The RooFit toolkit for data modeling," *ArXiv Physics e-prints*, June 2003.

[141] G. Cowan, K. Cranmer, E. Gross, and O. Vitells, "Asymptotic formulae for likelihood-based tests of new physics," *Eur. Phys. J.*, vol. C71, p. 1554, 2011. [Erratum: Eur. Phys. J.C73,2501(2013)].

[142] A. L. Read, "Presentation of search results: The CL_s technique," *J. Phys.*, vol. G28, pp. 2693–2704, 2002. [,11(2002)].